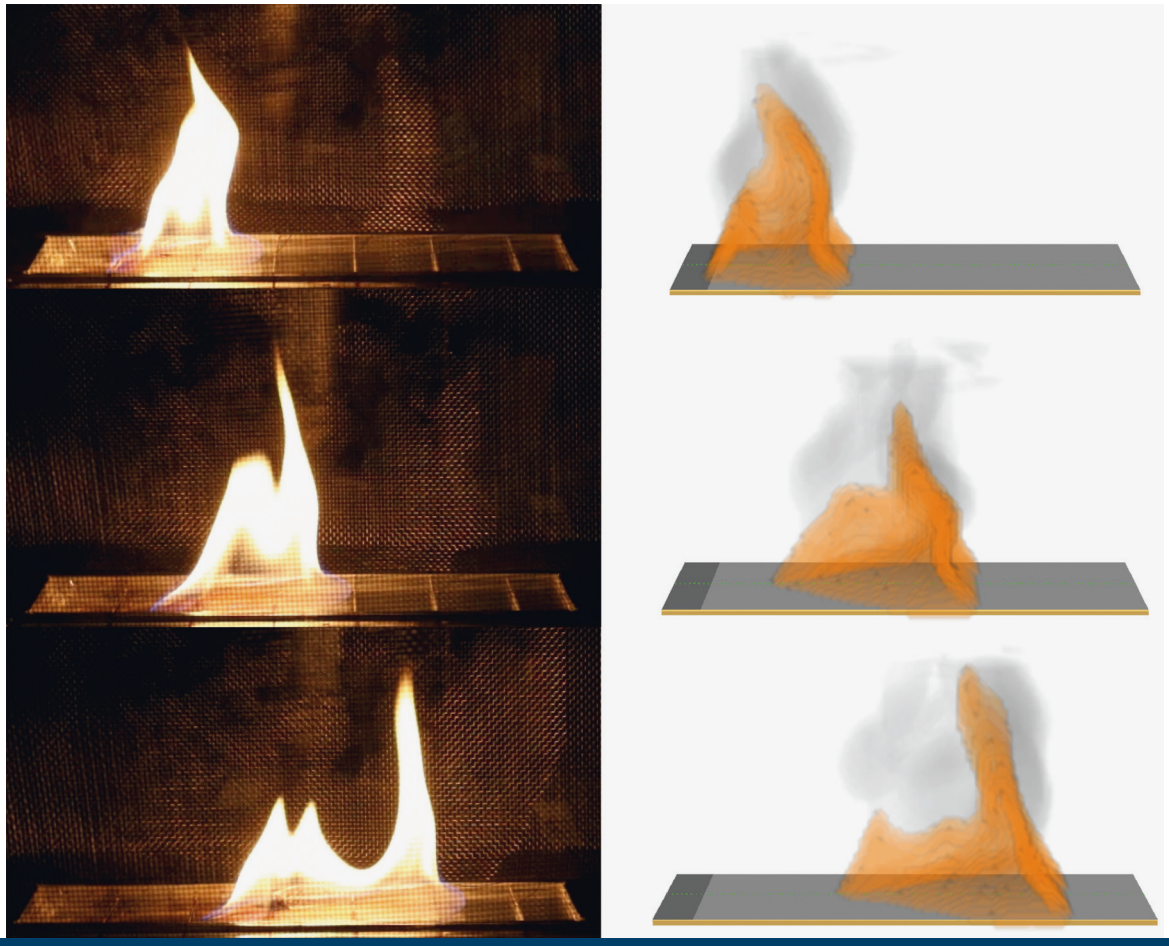

Sensitivity Analysis on Flame Spread Simulation

Tássia Lins da Silva Quaresma

IAS Series
Band / Volume 76
ISBN 978-3-95806-894-0

Mitglied der Helmholtz-Gemeinschaft

JÜLICH
Forschungszentrum

Schriften des Forschungszentrums Jülich
IAS Series Band / Volume 76

Forschungszentrum Jülich GmbH
Institute for Advanced Simulation (IAS)
Zivile Sicherheitsforschung (IAS-7)

Sensitivity Analysis on Flame Spread Simulation

Tássia Lins da Silva Quaresma

Schriften des Forschungszentrums Jülich
IAS Series

Band / Volume 76

ISSN 1868-8489

ISBN 978-3-95806-894-0

Bibliografische Information der Deutschen Nationalbibliothek.
Die Deutsche Nationalbibliothek verzeichnet diese Publikation in der
Deutschen Nationalbibliografie; detaillierte Bibliografische Daten
sind im Internet über http://dnb.d-nb.de abrufbar.

Herausgeber und Vertrieb:	Forschungszentrum Jülich GmbH Zentralbibliothek, Verlag 52425 Jülich Tel.: +49 2461 61-5368 Fax: +49 2461 61-6103 zb-publikation@fz-juelich.de www.fz-juelich.de/zb
Umschlaggestaltung:	Grafische Medien, Forschungszentrum Jülich GmbH
Druck:	Grafische Medien, Forschungszentrum Jülich GmbH
Copyright:	Forschungszentrum Jülich 2026

Schriften des Forschungszentrums Jülich
IAS Series, Band / Volume 76

D 468 (Diss. Wuppertal, Univ., 2025)

ISSN 1868-8489
ISBN 978-3-95806-894-0

Vollständig frei verfügbar über das Publikationsportal des Forschungszentrums Jülich (JuSER)
unter www.fz-juelich.de/zb/openaccess.

This is an Open Access publication distributed under the terms of the Creative Commons Attribution License 4.0,
which permits unrestricted use, distribution, and reproduction in any medium, provided the original work is properly cited.

To the women in my family, and to my father.

Acknowledgements

I would like to express my deepest gratitude to Prof. Dr. Lukas Arnold for his supervision and support over the past four years. Thank you for the enriching discussions and words of encouragement that helped me overcome the personal and professional challenges I faced along the way.

Thank you also to Dr. Tristan Hehnen for his co-supervision, patience, and dedication during our long discussions. I learned a great deal from his knowledge and experience.

Thank you to Prof. Dr. Armin Seyfried and the colleagues of the IAS-7 for welcoming me with open arms. I would especially like to thank Dr. Carole Babelot, for caring, for speaking up, for being so supportive and for contributing so much to creating such a healthy work environment.

I am also grateful to the new friends I made on this journey: Joel, Tania, Rudina, Karen, Ignacio, Inga, Kristian, Jette and Philipp. The fun moments we shared made my days much happier.

Last but not least, I would like to thank my husband and life partner, Rodrigo. Thank you for accepting my invitation to join me on this journey and, more importantly, for enduring it.

Abstract

Predicting how quickly a fire can grow over surrounding combustible materials is a critical aspect in assessing fire scenarios. A promising approach to this challenge lies in numerical flame spread simulations that are able to predict the heat release rate (HRR) and rate of spread (ROS), based on pyrolysis modelling. However, a major constraint in developing pyrolysis models is the difficulty in obtaining all the required material parameters. These parameters are commonly derived using inverse modelling and optimisation techniques, taking bench-scale experimental data as targets. This thesis investigates two fundamental aspects of such techniques that may affect the reliability of estimated material properties for modelling pyrolysis and predicting flame spread: (1) the assumption that material parameters estimated from bench-scale experiments (e.g., cone calorimeter) are transferable to flame spread scenarios, and (2) the level of accuracy required in fitting experimental data to ensure that uncertainties in the estimated parameters are sufficiently low. Using horizontal flame spread over poly(methyl methacrylate) (PMMA) as a case study, sensitivity analyses are applied to quantify how uncertainties in material parameters influence ROS and HRR predictions. Results show that parameter sensitivities differ considerably between a simplified cone calorimeter and flame spread simulations conducted using the Fire Dynamics Simulator (FDS), challenging the assumption of direct parameter transferability. Moreover, even small mass loss rate peaks observed in differential thermogravimetric analysis data can measurably affect ROS predictions, highlighting the importance of accurately characterising pyrolysis rates. Further, a validation study using data from a small-scale horizontal flame spread experiment revealed difficulties in simultaneously achieving accurate predictions of ROS and temperature profiles within the solid. This discrepancy suggests that further research is needed to assess current limitations related to heat flux calculations and the 1D heat conduction model in FDS, so that the overall predictive capabilities of flame spread simulations are improved.

Kurzfassung

Die Vorhersage, wie schnell sich ein Feuer über umliegende brennbare Materialien ausbreiten kann, ist ein entscheidender Aspekt bei der Bewertung von Brandszenarien. Ein vielversprechender Ansatz zur Lösung dieser Herausforderung sind numerische Simulationen der Flammenausbreitung, die dynamisch die Wärmefreisetzungsrate (HRR) und die Ausbreitungsrate (ROS) basierend auf Pyrolyse-Modellen vorhersagen. Eine wichtige Einschränkung bei der Entwicklung von Pyrolyse-Modellen ist jedoch die Schwierigkeit, alle erforderlichen Materialparameter zu ermitteln. Diese Parameter werden häufig durch Inversmodellierung und Optimierungstechniken unter Verwendung von experimentellen Daten im kleinen Maßstab abgeleitet. Diese Arbeit untersucht zwei grundlegende Aspekte solcher Techniken, die die Zuverlässigkeit der geschätzten Materialeigenschaften für die Modellierung der Pyrolyse und die Vorhersage der Flammenausbreitung beeinflussen können: (1) die Annahme, dass Materialparameter, die aus Experimenten im kleinen Maßstab (z. B. Kegelkalorimeter) geschätzt wurden, auf Flammenausbreitungsszenarien übertragbar sind, und (2) der erforderliche Genauigkeitsgrad bei der Anpassung experimenteller Daten, um sicherzustellen, dass die Unsicherheiten der geschätzten Parameter ausreichend gering sind. Am Beispiel der horizontalen Flammenausbreitung über Poly(methylmethacrylat) (PMMA) wurde eine Sensitivitätsanalyse durchgeführt, um zu quantifizieren, wie Unsicherheiten in den Materialparametern die Vorhersagen von ROS und HRR beeinflussen. Die Ergebnisse zeigen, dass die Sensitivitäten der Parameter zwischen einem vereinfachten Kegelkalorimeter und Flammenausbreitungssimulationen im Fire Dynamics Simulator (FDS) erheblich variieren, was die Annahme der direkten Übertragbarkeit infrage stellt. Eine Validierungsstudie zeigte, dass die gleichzeitige genaue Vorhersage von ROS und Temperaturprofilen schwierig ist, was weitere Untersuchungen der Wärmeflussberechnungen und des 1D-Wärmeleitungsmodells in FDS erfordert.

Contents

List of Figures

List of Tables

Abbreviations

A	Pre-exponential factor
CAPA	Controlled Atmosphere Pyrolysis Apparatus
Cone_04	Simplified cone calorimeter simulation
DSC	Differential scanning calorimeter
DTG	Differential thermogravimetric analysis
E	Activation energy
FDS	Fire Dynamics Simulator
HRR	Heat release rate
HRRPUV	Heat release rate per unit volume
MCC	Microscale combustion calorimeter
MLR	Mass loss rate
n	Order of reaction
PCE	Polynomial Chaos Expansion
PMMA	Poly(methyl methacrylate)
$\text{PMMA}_{\text{melt}}$	Material component of PMMA sample
PMMA_{int}	Intermediate component from $\text{PMMA}_{\text{melt}}$ pyrolysis
PMMA_{imp}	Material component of PMMA sample
PMMA_{gas}	Combustible gas from PMMA pyrolysis
RMSE	Root mean square error
ROS	Rate of spread
R1	Pyrolysis reaction associated to $\text{PMMA}_{\text{melt}}$
R2	Pyrolysis reaction associated to PMMA_{int}
R3	Pyrolysis reaction associated to PMMA_{imp}
SCE	Shuffled complex evolution optimisation
S1	First-order Sobol sensitivity index
S2	Second-order Sobol sensitivity index
S3	Third-order Sobol sensitivity index
ST	Total-order Sobol sensitivity index
STA	Simultaneous Thermal Analysis
TGA	Thermogravimetric analysis
T_p	Peak temperature
ΔT	Pyrolysis range
ΔH_R	Heat of reaction

Chapter 1

Introduction

1.1 Motivation

In fire protection engineering, predicting how quickly a fire can grow over surrounding combustible materials is a critical aspect in assessing fire scenarios. This information is essential for designing effective evacuation and response strategies to minimise damage to structures, the environment, and human life. In building compartments, this prediction helps determine the time to flashover, while in open vegetation areas, it aids in understanding how quickly the fire can spread across the landscape. In order to accurately predict the fire growth rate, it is necessary to understand and model the flame spread process, which is the fundamental mechanism driving fire spread.

Among the various modelling approaches available to represent fire spread, the present work is in the context of numerical models that aim to predict flame spread behaviour. These models, also known as predictive flame spread simulations, allow the heat release rate (HRR) from the fire to be calculated by the simulation itself, rather than being prescribed. This is achieved by taking into account the modelling of material pyrolysis, where both the heat transfer within the solid and the rates of pyrolysis are calculated. As a result, the simulated flame can dynamically respond to changes in environmental conditions, such as reduced oxygen concentrations.

These features make predictive flame spread simulations significantly more advantageous than traditional modelling approaches based on prescriptive design fires. However, a major challenge in their development is the difficulty in obtaining all the material properties required to model pyrolysis. These include thermophysical and optical properties, as well as kinetic parameters, all of which must be provided as simulation inputs. Together, these properties define the identity of materials and determine how they behave during heat transfer processes and thermal decomposition.

In response to this challenge, considerable effort within the fire research community has been dedicated to determining material properties needed for pyrolysis modelling. One prominent example is the ongoing work of the Measurement and Computation of Fire Phenomena (MaCFP) working group, which focuses on the estimation of material properties from micro- and bench-scale experimental data to support the validation and development of predictive fire models [Leventon et al., 2022, 2023]. In this context, inverse modelling and optimisation are a widely employed for material property estimation, using data from such experiments as targets.

This thesis contributes to these ongoing efforts by addressing two fundamental issues associated with inverse modelling for pyrolysis in flame spread simulations. The first concerns the common assumption of parameter transferability across fundamentally different experimental setups. Typically, the experiments used for parameter estimation are conducted under conditions where flame spread is negligible or entirely absent, raising questions about the validity of applying these parameters to full-scale flame spread scenarios. The second issue relates to the level of agreement required between the model and experimental data during the inverse modelling process. Specifically, it is still unclear how closely the simulation must match the target data to ensure that uncertainties in the estimated parameters are acceptably low.

This work is motivated by these challenges, which are central to improving the reliability and applicability of inverse modelling approaches for estimating pyrolysis properties that can be used to predict flame spread with sufficient accuracy.

1.2 State of the Art

1.2.1 Inverse modelling for estimating material properties

The standard procedure for determining the thermal properties of solid materials is through measurement techniques based on fundamental physical laws. For example, the thermal conductivity of insulation materials is commonly derived using the guarded hot-plate technique [Hammerschmidt et al., 2015]. In this method, a steady-state heat flux is applied to the sample and the resulting temperature gradient is measured. The thermal conductivity is then calculated using the Fourier's law of heat conduction. Another example is the laser flash analysis, a transient measurement technique widely used for more conductive materials. This method determines thermal diffusivity, from which thermal conductivity can be derived [Yang et al., 2019; DiDomizio et al., 2024].

However, in nearly all techniques used to experimentally determine the thermal properties of solid materials, measurements are conducted at temperatures below those at which pyrolysis occurs. As a result, the derived properties represent the material's behaviour only under the specific experimental conditions and may not accurately capture its response during pyrolysis. Even though some efforts have been made to determine certain thermophysical properties at higher temperatures [Hasburgh and Boardman, 2023; DiDomizio et al., 2024], obtaining a complete set of required properties under these conditions is still very challenging. That is because phenomena such as swelling, cracking, melting, bending, and bubbling, greatly complicate experimental measurements. Moreover, during the burning of the sample, intermediate materials and substances may be formed, which are difficult to isolate and analyse.

In this scenario, researchers in the field of fire science have resorted to inverse modelling and optimisation techniques to estimate the required properties needed to model pyrolysis and flame spread. Some of the most prominent works in this area were carried out by Lautenberger et al. [2006]; Rein et al. [2006]; Matala et al. [2008]; Lautenberger and Fernandez-Pello [2009]. The authors introduced methodologies that consist of using data of simple bench-scale experiments as target in an optimisation procedure. In this, an optimisation algorithm is employed to find the set of input parameters that best fits the model output to the experimental data, with the fitness evaluated by a cost function. This process is illustrated by the flowchart presented in Figure 1.1.

Data commonly used as targets in the inverse modelling come from micro- and bench-scale experiments such as Thermogravimetric Analysis (TGA) [West, 1954], Microscale Combustion Calorimeter (MCC) [Coats and Redfern, 1963], Cone Calorimeter [Babrauskas, 1982], and others [Spink, 2008]. In micro-scale experiments such as TGA and MCC, samples of a few milligrams allow heat transfer effects to be assumed negligible and only kinetic effects to be captured. TGA measurements provide mass loss over time (or temperature), from which the derivative thermogravimetric (DTG) curve can be derived, leading to mass loss rate (MLR) curves. These curves have both been used to determine kinetic parameters, along with the HRR measured from MCC experiments. At bench scale, mass loss over time and HRR, as measured by the cone calorimeter, have been used to derive the material's thermophysical properties. Lautenberger et al. [2006] used a genetic algorithm to generate kinetic parameters and thermophysical properties of charring and polymeric materials from cone calorimeter data. The main goal of that study was to generate material properties needed to

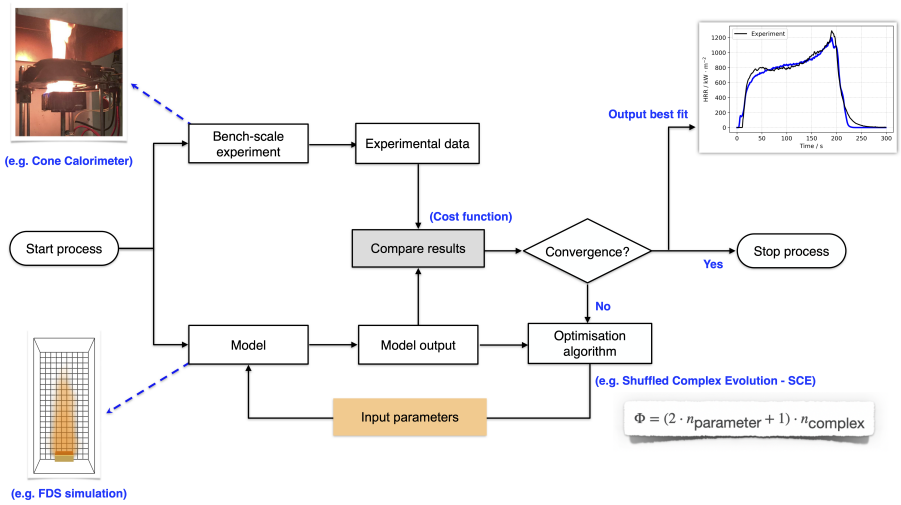

Figure 1.1: Flowchart illustrating an inverse modelling process to estimate input parameters. Adapted from Lauer et al. [2016]; Hehnen et al. [2018].

model pyrolysis in large-scale simulations of fire growth. Later, the works by Rein et al. [2006]; Matala et al. [2008]; Matala and Hostikka [2013] explored deriving kinetic parameters in a separate step based on TGA and MCC data.

The performance of various optimisation algorithms was evaluated in subsequent studies by Chaos et al. [2011] and Lautenberger and Fernandez-Pello [2011] in terms of accuracy and computational efficiency. These studies explored different types of optimisation methods, including genetic, stochastic, and evolutionary approaches. Both studies concluded that the Shuffled Complex Evolution (SCE) algorithm outperformed the others, converging to values closest to reference parameters and was therefore recommended. Meunders et al. [2014] employed a gradient-based optimisation approach to estimate thermophysical properties using cone calorimeter data. They observed that although some estimated parameters became constrained at their sampling bounds, the set of input parameters still resulted in good agreement with the cone calorimeter data. Yet, great deviations were observed once the estimated parameter set was validated in a simulation of flame spread on an armchair. The improved accuracy of SCE was also observed by Kim and Dembsey [2015], although other types of strategies, such as stochastic hill-climbing algorithms, have been explored and used by other researchers to date [Webster Jr, 2009; Fiola et al., 2021].

In addition to analysing the performance of optimisation algorithms, the study

by Kim and Dembsey [2015] highlighted the limitations associated with optimisation strategies for parameter estimation. Their work aimed to provide guidance on the use of these methods by discussing how results can be affected by compensation effects and the way the model is set up. They showed that assumptions and simplifications made in the design of the model are reflected in the estimated values. Further, it was emphasised that, as a result, optimisation strategies may lead to multiple optimal parameter sets, but are worthwhile for estimating effective material properties. Compensation effects in inverse modelling in the context of pyrolysis modelling was also addressed in more detail by Bal and Rein [2015]. They demonstrated that different parameter sets are able to accurately predict the same experimental data considering different levels of model complexity.

Several authors [Matala and Hostikka, 2011; Hehnen et al., 2018, 2020; Viitanen et al., 2022] have applied inverse modelling to derive material properties for the purpose of predicting flame spread on real-scale horizontal cable tray installations. In general, these studies followed an optimisation approach divided into two steps: first, kinetic parameters are determined using TGA and/or MCC data as a target; then, in a second step, thermophysical properties are estimated using cone calorimeter data. Recently, Hehnen and Arnold [2023] explored this methodology considering various model designs, each leading to a different parameter set. The authors proposed a strategy to take into account in the cone calorimeter model the uneven distribution of the incident heat fluxes on the sample surface. The estimated sets of effective properties were subsequently used to define the solid phase in a predictive simulation of upward flame spread (see Leventon et al. [2024], Parallel Panel Test). The performance of each parameter set was then evaluated by comparing the predicted HRRs to the experimental measurements.

Yang et al. [2019] proposed a methodology to establish a prioritisation framework for estimating material properties from limited experimental data with greater efficiency and accuracy. The approach aims to distinguish between parameters that are best obtained by direct measurement and parameters that should be preferably derived through inverse modelling. The decision-making process is guided by a ranking of parameters based on their influence on the pyrolysis model and the difficulty (i.e. cost and effort) of measuring them directly. Their study recommends that parameters with lower influence on the model and higher difficulty of measurement should be estimated via inverse modelling using cone calorimeter data. Specifically, mass loss data from cone calorimeter experiments should be generated at two standard exposure powers as targets. In addition, they recommend that the performance of

the parameter set be validated against cone calorimeter mass loss data obtained at an exposure different from those used in the optimisation.

Other approaches proposed by Kim and Dembsey [2015] and Stoliarov and Li [2016] expanded the parameter estimation process by breaking it down into additional steps. They introduced a strategy that combines inverse modelling with direct measurements, grouping parameters with similar characteristics and determining them separately. Following a hierarchical methodology, Stoliarov and Li [2016] proposed that parameters derived from a set of experiments are used to interpret the results of the subsequent set of experiments, from where more properties are extracted. Their study incorporated more experimental techniques in the process of parameter estimation, such as Simultaneous Thermal Analysis (STA), and Controlled Atmosphere Pyrolysis Apparatus (CAPA). The STA is able to generate TGA and Differential Scanning Calorimeter (DSC) data from the same experiment, whereas CAPA consists of an adaptation of the cone calorimeter to study pyrolysis [Li et al., 2014].

Fiola et al. [2021] used a similar methodology to determine the material properties of two types of poly(methyl methacrylate) (PMMA). Their approach relied on both inverse modelling and direct measurements to derive complete sets of parameters. However, their study only describes the inverse modelling processes using a hill-climbing algorithm. The pyrolysis reaction scheme and associated kinetic parameters were derived from TGA data obtained from STA. Simultaneously obtained DSC data from STA were used to determine specific heat capacities and heats of pyrolysis, following a methodology presented elsewhere [Li and Stoliarov, 2013]. The heats of combustion of the pyrolyzates were determined from the MCC data. Thermal conductivities were estimated by inverse modelling using data from CAPA II experiments as target [Swann et al., 2017]. The methods used to measure the optical properties that make up the parameter set were described in a separate study by Linteris et al. [2012]. This parameter set is currently recommended by the MaCFP group as the set of properties to model PMMA pyrolysis, and has been used to predict flame spread in a room corner configuration [Chaudhari et al., 2021], and in the FDS validation manual [McGrattan et al., 2021].

1.2.2 Sensitivity analysis on solid-phase parameters

In pyrolysis modelling, the number of required material properties can be substantial, depending mainly on: the complexity of the material's behaviour during thermal degradation and; the level of detail within the selected models representing these processes. Simpler models may utilise only a few properties, while more detailed

approaches might require dozens of such properties as input parameters Lautenberger et al. [2006].

This high-dimensional modelling scenario presents several challenges. One of the most critical is the often unknown degree of influence that each parameter exerts on model outputs. Limited understanding of model sensitivities complicates both the assessment of model uncertainties, and the efficient estimation of the required input parameters. To address these issues, numerous studies in fire research have employed sensitivity analysis techniques in the context of pyrolysis and flame spread models. For a comprehensive review on this topic, the reader is encouraged to refer to the work by Nyazika et al. [2019]. In this section, several relevant contributions are highlighted and briefly discussed.

Sensitivity analyses in this context have been motivated by a range of goals, from improving model interpretability and robustness to increasing the efficiency of parameter estimation and guiding experimental design. For instance, studies by Lautenberger et al. [2006]; Chaos et al. [2011]; Chaos [2013] have addressed the importance of running sensitivity analyses with the goal of improving the efficiency of parameter estimation strategies based on inverse modelling and multi-objective optimisation. Given that the computational cost of such optimisation procedures typically increases with the number of parameters to be estimated, sensitivity analyses are often used to simplify the model by identifying parameters with negligible impact on the outputs. These less influential parameters can then be fixed or excluded from the optimisation process, saving computing time.

Chaos [2013] conducted sensitivity analyses on a pyrolysis model implemented in FireFoam. The study evaluated the influence of various parameters, including density, thermal conductivity, specific heat, and Arrhenius parameters, on MLR and surface temperature predictions. Ramroth et al. [2006] conducted sensitivity and uncertainty analyses for finite element thermal models of fiber-reinforced polymer panels exposed to fire. Their work focused on understanding how uncertainties in thermal conductivity, specific heat, and density affected temperature predictions within the material. They used both local and global (Monte Carlo) methods to evaluate sensitivities, illustrating the importance of accounting for input variability in predictive fire performance modelling of composite materials.

In this context, Batiot et al. [2016] conducted sensitivity and uncertainty analyses of Arrhenius parameters to better understand their influence on the thermal degradation kinetics of solids during fire events. The study also employed both global and

local sensitivity analysis methods to assess the impact of parameters like the pre-exponential factor and activation energy on MLRs. The global approach using Sobol indices was particularly useful to address interaction effects between the Arrhenius parameters, which were interpreted as a manifestation of the well-known compensation effect.

Yang et al. [2019] employed first-order sensitivity indices to evaluate a pyrolysis model implemented in the Fire Dynamics Simulator (FDS), aiming to identify the parameters that most strongly influenced the material's thermal response. The resulting parameter ranking was then incorporated into a proposed methodology for estimating material properties, helping to distinguish which parameters should preferably be determined via inverse modelling and which could be reliably obtained through direct measurement.

Wagner et al. [2020] addressed the calibration of temperature-dependent thermal material properties within heat transfer models for fire insulation panels. They employed a probabilistic approach using the Bayesian model calibration framework, which not only provided best-fit parameters but also offered confidence bounds on these estimates. To manage the computational demands of this framework, the authors employed surrogate modelling techniques, specifically combining polynomial chaos expansions with principal component analysis. This surrogate modelling facilitated the acceleration of the calibration process and enabled a sensitivity analysis, also through the computation of Sobol indices.

More recently, a couple of studies have performed sensitivity analyses on full-scale flame spread simulations with the purpose of identifying the most influential parameters such that their estimation can be improved. For instance, Ding et al. [2023] conducted a one-at-a-time sensitivity analysis on large-scale upward flame spread scenarios using FDS, aiming to identify which material input parameters most significantly affect flame spread behaviour. Their objective was to prioritise the most influential parameters, such that their experimental measurements and estimation accuracy can be improved.

Chaudhari and Stoliarov [2022] applied sensitivity analysis to understand how uncertainties in input parameters impact predictions of vertical corner flame spread. Their study aimed to assess the extent to which pyrolysis properties derived via inverse modelling from bench-scale experiments can be applied to large-scale fire scenarios, given the observed deviations from experimental data.

Similarly, Hehnen and Arnold [2023] derived material parameter sets from a series of bench-scale experiments, including TGA, MCC, and cone calorimeter experiments,

to predict large-scale flame spread in a parallel panel configuration. Their conclusions pointed to potential discrepancies in parameter sensitivities between small- and large-scale simulations as a possible cause for deviations between model predictions and experimental data. This raised important questions about the validity of parameter transfer across scales, particularly when parameters that are insensitive in bench-scale models become influential in real-scale scenarios.

Specifically on the influence of pyrolysis reaction schemes on model predictions, Bal and Rein [2011] investigated the effect of using different kinetic schemes on ignition times, considering single- and multiple-step reactions. Their study suggested that a single-step mechanism would be sufficient to represent the material behaviour, due to the secondary importance of kinetics in comparison to the heat transfer in the solid. Fiola et al. [2021] performed in their study a simplified sensitivity analysis to compare pyrolysis properties of extruded and cast PMMA for modelling gasification experiments. Among other differences, the two sets of properties differed by the number of peaks identified in TGA and MCC data. Their study concluded that pyrolysis properties of extruded and cast PMMA can be used interchangeably. However, their study was focused on micro- and bench-scale experiments (STA, MCC, CAPA II), setups where no flame spread takes place.

Despite these efforts, the literature addressing how parameter sensitivities vary across simulation setups, and how this affects the transferability of parameters estimated from bench-scale data to flame spread predictions, is limited. Thus, further research is needed to assess how uncertainties in estimated material parameters can affect the predictions of flame spread simulation models.

1.3 Objectives and Approach

The overall objective of this thesis is to investigate the effect of material parameters, derived via inverse modelling, on predictions of flame spread simulations conducted with FDS. The analyses focus on a case study in which a self-sustained flame spreads over a horizontal poly(methyl methacrylate) (PMMA) slab with bench-scale dimensions. Different sensitivity analysis methods are applied to evaluate the influence of material properties, taken as model inputs, on simulation outputs of interest, such as the HRR and the rate of spread (ROS).

The specific objectives of this work address two fundamental issues associated with the use of standard micro- and bench-scale experiments to estimate material parameters for predicting flame spread through inverse modelling:

- Parameter transferability: A common assumption is that material parameters estimated from bench-scale experiments, such as the cone calorimeter, are directly transferable to simulations involving flame spread. This work examines the validity of this assumption by analysing how the sensitivities to parameters may shift across a cone calorimeter simulation setup and a small-scale horizontal flame spread simulation.

- Required fit accuracy: There is limited guidance on the level of agreement required between model outputs and experimental data during the inverse modelling process to ensure reliable parameter estimation. Often, small deviations from target TGA data are considered negligible and are simply ignored. This study evaluates the extent to which this is reasonable by examining how improving the fit to small MLR peaks observed in DTG data affects flame spread predictions, particularly the ROS.

This thesis concludes with a validation study, in which a bench-scale horizontal flame spread experiment has been conducted for this specific purpose. Measurements of spread rates and solid-phase temperatures taken in the experiment are used to validate predictions of FDS simulations of flame spread on PMMA. The goal is to evaluate whether good agreement between ROS predictions and experimental measurements, is consistent to good agreement in terms of solid-phase temperatures.

1.4 Thesis Outline

This thesis is outlined as follows:

Chapter 2: General methodology

This chapter presents the main methods used in different parts of the thesis. It includes an overview of the numerical modelling approach used for the flame spread simulations within the FDS. The chapter also introduces the input parameters of interest relevant to the pyrolysis modelling, which are investigated through the sensitivity analyses. In addition, the mathematical formulation of the local and global sensitivity analysis methods used in this work is briefly provided.

Chapter 3: Transferability of effective properties estimated from cone calorimeter data

This chapter investigates the common assumption that material properties estimated through inverse modelling from cone calorimeter data can be directly transferred to flame spread simulations. Sensitivity analyses are conducted to compare the influence of input parameters across two simulation setups: a simplified cone calorimeter and a small-scale horizontal flame spread case. The findings highlight important differences in parameter sensitivities, raising questions about the general applicability of bench-scale data for flame spread modelling.

Chapter 4: The influence of small MLR peaks on flame spread predictions

This chapter explores how accounting for small MLR peaks observed in DTG data derived from TGA experiments, affects flame spread predictions, particularly the rate of spread. Through a combination of sensitivity analysis and simulation comparisons, it is shown that even minor peaks in the pyrolysis temperature range can significantly affect the simulated spread rates. The results emphasise the importance of accurately characterising pyrolysis behaviour in inverse modelling processes and suggest that small experimental variations may have non-negligible consequences in simulation predictions of interest.

Chapter 5: Horizontal flame spread: experiment and simulation

This chapter presents a validation study of flame spread simulations against a small-scale horizontal experiment. The goal is to evaluate the accuracy of simulation predictions for spread rates and temperature profiles within the solid using parameter sets and modelling practices common in the fire research community. The study discusses challenges related to grid resolution, heat transfer modelling, and material representation, and identifies important sources of uncertainty that affect the accuracy of the predictions.

Chapter 6 – Closing remarks

This final chapter summarises the main conclusions drawn from the preceding analyses and discusses their implications for flame spread modelling. It highlights limitations in current parameter estimation approaches and outlines recommendations for future work, including more comprehensive validation efforts and improved experimental methods. The chapter also reflects on the broader relevance of sensitivity analysis in understanding and improving simulation-based fire predictions.

Chapter 2

General methodology

This chapter provides an overview of the models employed in this work, including those used in the simulations and those used for sensitivity analyses. The focus is not to present a detailed theoretical framework, but rather to highlight the main equations and parameters used throughout the thesis.

2.1 Numerical modelling of flame spread

The simulation models investigated in the scope of this study were developed using the Fire Dynamics Simulator (FDS) [McGrattan et al., 2005]. FDS is a computational fluid dynamics (CFD) software widely used in fire research and fire safety engineering for simulating fire and smoke dynamics. The software has been designed to numerically solve the Navier-Stokes equations for incompressible flows, focusing on flows driven by the heat transport from fires.

FDS is composed by a large number of sub-models which are intended to represent the main phenomena involved in fires, such as turbulence, combustion, pyrolysis and heat transfer. Most of these sub-models can be changed or adjusted according to the target application, the level of detail desired, and the amount of information available. In its standard formulation, the turbulence problem is addressed following the Large Eddy Simulation (LES) approach. The governing flow equations are numerically solved on a rectilinear grid, while sub-grid phenomena are typically represented through empirical or semi-empirical correlations, or simplified physical models.

As in the real phenomenon, the simulation of flame spread results from the coupling of the solid and the gas phases, represented each by two sets of several sub-models [Drysdale, 2011; Rogaume, 2019]. It is therefore appropriate to present the modelling approaches for each phase separately. The next sub-sections provide a summary of the main sub-models that constitute the solid and the gas phases in the flame

spread simulations. Special attention is given to the solid phase, as the main focus of this work has been on the material properties and kinetic parameters associated with heat transfer and pyrolysis of the solid phase.

The FDS simulations were executed on the PLEIADES computing cluster at the University of Wuppertal [PLEIADES, 2025]. Pleiades is a high-performance computing (HPC) system that comprises 268 worker nodes with a total of 17,152 cores. Each worker node features 2 AMD EPYC 7452 32-Core processors, each operating at a base clock speed of 2.350 GHz, and is equipped with 256 GB of memory, corresponding to 4 GB per core.

2.1.1 Solid phase

The modelling of the solid phase is based on the approach referred to in the FDS User Guide [McGrattan et al., 2005] as the complex pyrolysis model. This approach takes into account the heat transfer within the solid, with pyrolysis rates coupled to the local temperatures of the solid material. Unlike the simpler methods available in FDS for representing pyrolysis, the complex pyrolysis model allows the heat release rates from the fire to be predicted by the simulation itself, rather than being prescribed.

The general formulation that allows self-sustained flame propagation in the simulation is based on heat and mass transfer between a gas cell and the surface of the solid. The heat released by the combustion reaction in the gas phase is transferred to the solid by radiation and convection. Some of this energy is absorbed, which eventually raises the temperature of the solid to its pyrolysis point and initiates thermal decomposition. The mass released from the solid is then injected into the gas phase for combustion, creating a continuous feedback loop that maintains the spread [Rogaume, 2019].

This process is illustrated in Figure 2.1, which shows the radiative ($\dot{q}''_{\mathrm{r}}$) and convective ($\dot{q}''_{\mathrm{c}}$) heat fluxes from a gas cell to the solid surface, and the mass flux ($\dot{m}''$) from the solid to the gas phase. The in-depth heat transfer processes of conduction and radiation in the solid were omitted for brevity, but will be described in more detail further in this section.

Heat conduction

The default one-dimensional heat conduction model in FDS is used. This means that heat conduction is considered only in the direction normal to the sample surface,

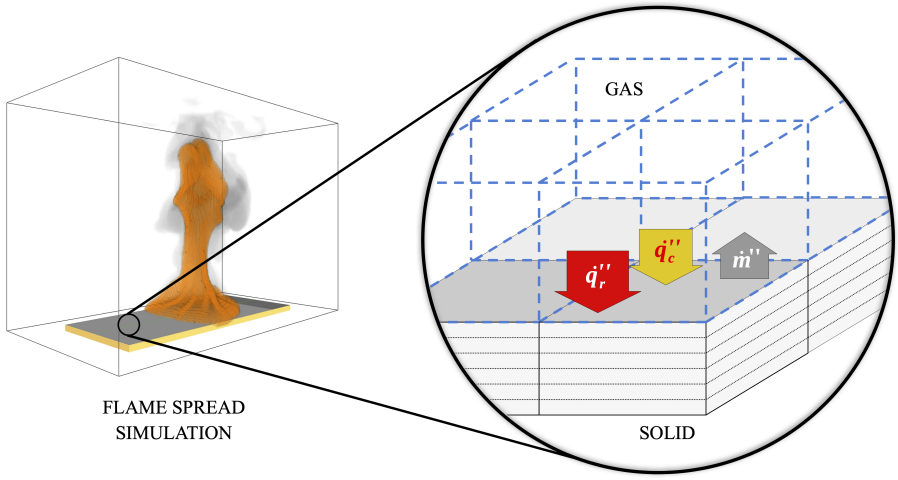

Figure 2.1: Illustration of incoming heat fluxes and evolving mass flux between a gas cell and a solid surface in FDS. Adapted from lecture slides by Prof. Simo Hostikka.

into the solid, which is here denoted by x. For every layer of a solid material, the following energy equation is solved:

$$\rho_s c_s \frac{\partial T_s}{\partial t} = \frac{\partial}{\partial x}\left(k_s \frac{\partial T_s}{\partial x}\right) + \dot{q}_s''' \tag{2.1}$$

where ρ_s denotes the density, c_s the specific heat capacity, k_s the thermal conductivity of the solid material. T_s denotes the temperature of the solid, and $\dot{q}_s'''$ is the heat source term, consisting of two contributions:

$$\dot{q}_s''' = \dot{q}_{s,c}''' + \dot{q}_{s,r}''' \tag{2.2}$$

where $\dot{q}_{s,c}'''$ accounts for the heat release or absorption due to chemical reactions. The term $\dot{q}_{s,r}'''$ corresponds to radiative heat absorbed or emitted in depth [McGrattan et al., 2013].

The source term due to chemical reactions is determined by:

$$\dot{q}_{s,c}'''(x) = -\sum_{\alpha=1}^{N_m} \sum_{\beta=1}^{N_{r,\alpha}} r_{\alpha\beta}(x) H_{r,\alpha\beta} \tag{2.3}$$

where $N_{r,\alpha}$ is the number of reactions for material component α, $r_{\alpha\beta}(x)$ is the rate of reaction β, N_m is the number of material components, and $H_{r,\alpha\beta}$ is the heat (enthalpy) of reaction β that component α can undergo.

The heat of reaction is by convention positive for endothermic reactions, and negative for exothermic reactions. The negative sign in Equation (2.3) accounts for this definition, ensuring that an endothermic reaction, which absorbs heat from the material, results in a cooling effect, while an exothermic reaction, which releases heat, contributes to heating the material. In the context of this study, the chemical reactions considered are pyrolysis reactions, which are predominantly endothermic.

Reaction rates

The rate of reaction is given by the following expression:

$$r_{\alpha\beta} = \rho_{\mathrm{s},\alpha}^{n_{\mathrm{s},\alpha\beta}} \quad [X_{\mathrm{O}_2}(x)]^{n_{\mathrm{O}_2,\alpha\beta}} \quad T_{\mathrm{s}}^{n_{\mathrm{t},\alpha\beta}} \quad k_{\alpha\beta} \tag{2.4}$$

where $\rho_{\mathrm{s},\alpha}$ represents the transient concentration of component α, $[X_{\mathrm{O}_2}(x)]$ accounts for oxygen-limited reactions, and T_{s} is a power function for the temperature. Each of these terms is raised to the power of the corresponding reaction order n. The last term on the right hand side of expression (2.4) is often referred to as the rate constant, given by the Arrhenius law [Arrhenius, 1889]:

$$k_{\alpha\beta} = A_{\alpha\beta} \exp\left(-\frac{E_{\alpha\beta}}{RT_{\mathrm{s}}}\right) \tag{2.5}$$

where $A_{\alpha\beta}$ is the pre-exponential factor, $E_{\alpha\beta}$ is the activation energy, R is the ideal gas constant, and T_{s} is the absolute temperature of the solid.

In a more specific formulation relevant to the pyrolysis modelling approach used in this work, the reaction rate, as presented in Equation 2.4, can be described as:

$$\dot{\omega} = k(T) f(\alpha) \tag{2.6}$$

where $k(T)$ is the Arrhenius law, presented in Equation 2.5, and $f(\alpha)$ is the reaction model, which depends on the progress of the reaction (conversion), denoted by α.

There are several possible functions to describe $f(\alpha)$, as discussed elsewhere [Rogaume, 2019; Vyazovkin et al., 2022]. However, the most commonly used is the n-th order reaction model:

$$f(\alpha) = (1 - \alpha)^n \tag{2.7}$$

where n is the reaction order, and $(1 - \alpha)$ corresponds to the unreacted fraction of the material. This is the reaction model currently implemented in FDS.

In-depth radiation

The source term $\dot{q}'''_{\mathrm{s,r}}$ in Equation (2.2) accounts for the in-depth penetration of thermal radiation into the solid material by means of the so-called two-flux model [Howell et al., 2020]:

$$\dot{q}'''_{\mathrm{s,r}}(x) = \frac{\mathrm{d}\dot{q}^{+}_{\mathrm{r}}(x)}{\mathrm{d}x} + \frac{\mathrm{d}\dot{q}^{-}_{\mathrm{r}}(x)}{\mathrm{d}x} \tag{2.8}$$

where the terms on the right-hand side of the equation denote respectively the radiative fluxes transported forwards (in the positive $+x$ direction), and backwards towards the surface (in the negative $-x$ direction).

The forward radiative heat flux entering the solid is given by the following expression:

$$\frac{1}{2}\frac{\mathrm{d}\dot{q}^{+}_{\mathrm{r}}(x)}{\mathrm{d}x} = \kappa_{\mathrm{s}}\left(\sigma T_{\mathrm{s}}^{4} - \dot{q}^{+}_{\mathrm{r}}(x)\right) \tag{2.9}$$

where κ_{s} is the absorption coefficient, σ is the Stefan-Boltzmann constant, and $\dot{q}^{+}_{\mathrm{r}}(x)$ is the self-absorption term. An equivalent expression for the backward radiative transport can be derived as in Equation (2.9).

Boundary conditions

The boundary condition at the surface of the solid ($x = 0$) is determined by the combined effect of convective ($\dot{q}''_{\mathrm{c}}$) and radiative ($\dot{q}''_{\mathrm{r}}$) heat fluxes from the gas phase:

$$-k_{\mathrm{s}}\frac{\partial T_{\mathrm{s}}}{\partial x}(0,t) = \dot{q}''_{\mathrm{c}} + \dot{q}''_{\mathrm{r}} \tag{2.10}$$

If the internal radiation model is used, radiation is assumed to penetrate in depth and the surface radiation term $\dot{q}''_{\mathrm{r}}$ in Equation 2.10 is set to zero. This is the case for the modelling applications in this study, as the material undergoing pyrolysis is assumed not to be opaque. The coupling between the radiation field and the solid temperature is therefore established by the source term of the heat conduction equation, as shown in Equations 2.8 and 2.9.

The boundary condition for Equation (2.9) at the surface of the solid is given by:

$$\dot{q}^{+}_{\mathrm{r}}(0) = \dot{q}''_{\mathrm{r,in}} + (1-\varepsilon)\dot{q}^{-}_{\mathrm{r}}(0) \tag{2.11}$$

where $\dot{q}^{-}_{\mathrm{r}}(0)$ is the backward radiative heat flux, which is the flux transferred from a certain depth towards the surface of the solid, and the term $\dot{q}''_{\mathrm{r,in}}$ accounts for the incoming radiative heat flux, given by the integral of radiative intensity over all incoming directions:

$$\dot{q}''_{\mathrm{r,in}} = \varepsilon \int_{\mathbf{s}'\cdot\mathbf{n}_{\mathrm{w}}<0} I_{\mathrm{w}}\left(\mathbf{s}'\right)\left|\mathbf{s}'\cdot\mathbf{n}_{\mathrm{w}}\right|\mathrm{d}\Omega \tag{2.12}$$

where ε is the emissivity of the solid material, $I_{\mathrm{w}}(\mathbf{s}')$ is the radiative intensity incident on the surface from direction $\mathbf{s}'$, and $\mathbf{n}_{\mathrm{w}}$ is the unit normal vector to the surface.

The convective heat flux to a solid surface in LES simulation mode is given by:

$$\dot{q}''_{\mathrm{c}} = h\left(T_{\mathrm{g}} - T_{\mathrm{w}}\right) \tag{2.13}$$

where h is the convective heat transfer coefficient, T_{g} is the temperature of the gas cell in contact with the surface of the solid. The convective heat transfer coefficient is taken as the maximum of the Nusselt (Nu) numbers for free and forced convection:

$$h = \frac{k}{L}\max\left(\mathrm{Nu}_{\mathrm{free}}\,, \mathrm{Nu}_{\mathrm{forced}}\,, \frac{2L}{\delta n}\right) \tag{2.14}$$

where k is the thermal conductivity of the gas, L is a characteristic length taken as 1 m for planar surfaces, and δn is gas cell edge length. The Nusselt numbers for both free and natural convection are calculated based on empirical correlations [McGrattan et al., 2013].

2.1.2 Gas phase

The gas phase modelling in FDS follows a formulation proposed by Rehm and Baum [Rehm and Baum, 1978] to describe the fluid dynamics induced primarily by the heat released from a fire. Under the low-Mach number assumption, the temporally and spatially resolved pressure p is divided into a mean pressure $\overline{p}$ and a perturbation pressure $\tilde{p}$ [McGrattan et al., 2013; Rehm and Baum, 1978].

The mean pressure, $\overline{p}(z,t)$, accounts for a stratified atmosphere, and is taken as the background pressure in the simulations. It is determined using the equation of state for an ideal gas:

$$\overline{p} = \frac{\rho R T}{\overline{W}} \tag{2.15}$$

where ρ is the mass density of the gas mixture, given by the sum of the partial densities of the gases composing the mixture; R is the ideal gas constant; T is the absolute temperature; and $\overline{W}$ denotes the average molecular weight of the gas mixture.

Since the background pressure $\overline{p}$ and enthalpy h are related ($h = e + \overline{p}/\rho$, where e is internal energy), $\overline{p}$ appears as well in the sensible enthalpy (h_s) transport equation:

$$\frac{\partial \rho h_s}{\partial t} + \nabla\cdot(\rho h_s \mathbf{u}) = \frac{\mathrm{D}\overline{p}}{\mathrm{D}t} - \nabla\cdot\dot{\mathbf{q}}'' + \dot{q}''' \tag{2.16}$$

where ∇ is the nabla operator; $\mathbf{u}$ is the velocity vector; the first term on the right hand side is the material derivative of the mean pressure; the term $\dot{\mathbf{q}}''$ denotes the

conductive, diffusive, and radiative fluxes. and $\dot{q}'''$ is a source term representing the heat release rate per unit volume from a combustion reaction [McGrattan et al., 2013].

The perturbation pressure $\tilde{p}(x, y, z, t)$ drives the fluid motion, and is the spatially non-uniform part of the pressure p which only appears in the momentum transport Equation [Rehm and Baum, 1978]:

$$\frac{\partial \rho \mathbf{u}}{\partial t} + \nabla \cdot (\rho \mathbf{u}\mathbf{u}) = -\nabla \tilde{p} - \nabla \cdot \boldsymbol{\tau} + (\rho - \rho_0)\,\mathbf{g} \tag{2.17}$$

where $\boldsymbol{\tau}$ is the shear stresses tensor, ρ_0 is the background density, and $\mathbf{g}$ is the gravitational acceleration vector. By combining the momentum and the continuity equations, an expression for $\tilde{p}$ can be derived, whose solution results in a wave function [Rehm and Baum, 1978].

Modelling a reacting flow requires accounting for the transport of each chemical species involved in the chemical reaction to be considered, which is in this case the combustion reaction. In FDS, this requirement is simplified using the lumped species approach, which will be explained later in Equation (2.20). The transport equation for a lumped species is given by:

$$\frac{\partial \rho Z_\alpha}{\partial t} + \nabla \cdot (\rho Z_\alpha \mathbf{u}) = \nabla \cdot (\rho D_\alpha \nabla Z_\alpha) + \dot{m}'''_\alpha + \dot{m}'''_{\mathrm{b},\alpha} \tag{2.18}$$

where α is a lumped species (i.e. fuel, air or products); Z_α is the mass fraction of α; D_α is the diffusivity; $\dot{m}'''_\alpha$ is the production rate of α due to the combustion reaction; and $\dot{m}'''_{\mathrm{b},\alpha}$ is a source term added to account for the production of species α due to evaporating droplets or particles.

The conservation of mass is ensured by summing Equation (2.18) over all the lumped species, leading to the continuity equation:

$$\frac{\partial \rho}{\partial t} + \nabla \cdot (\rho \mathbf{u}) = \dot{m}'''_{\mathrm{b}} \tag{2.19}$$

where the total density is given by $\rho = \sum(\rho Z)_\alpha$. Equation (2.19) is derived under the following considerations:

- the sum of diffusive fluxes is zero, $\sum \rho D_\alpha \nabla Z_\alpha = 0$;
- the mass fractions of all lumped species sum to unity $\sum Z_\alpha = 1$;
- the net sum of all source terms is zero, $\sum \dot{m}'''_\alpha = 0$, given that reactants have negative production rates and products have positive;
- the total mass source term satisfies $\sum \dot{m}'''_{\mathrm{b},\alpha} = \dot{m}'''_{\mathrm{b}}$.

Simulation mode

This work adopts the LES simulation mode, although the current default approach in FDS uses the Very Large Eddy Simulation (VLES) mode. This choice ensures consistency with previous related work [Hehnen and Arnold, 2023; Hehnen et al., 2020], while offering a more accurate representation of the flow compared to VLES.

It is important to note that in FDS the simulation mode refers not only to the turbulence model, but also to a number of other sub-models describing phenomena, such as flame extinction and near-wall interactions. When LES was selected as the simulation mode, all default settings relating to these other sub-models were left unchanged. These include the Deardorff model for subgrid scale eddy viscosity and the Wall-Adapted Local Eddy Viscosity (WALE) model for near-wall turbulence. The extinction model considers the calculated temperature at each gas cell in addition to the local oxygen concentrations to determine whether combustion is possible. The default numerical stability settings were also left unchanged [McGrattan et al., 2013].

Combustion

Combustion is handled by the mixing-controlled model, which assumes an infinitely fast chemistry, with the reaction rate limited only by the turbulent mixing time scale. To reduce the computational burden of solving a transport equation for each individual species involved in the combustion reaction, FDS employs the lumped species approach. In this approach, the primitive species – such as fuel, oxygen, carbon monoxide, carbon dioxide, and water vapour – are grouped into just three lumped species:

$$\text{Fuel} + \text{Air} \longrightarrow \text{Products}. \tag{2.20}$$

The mass fractions of the primitive species are retrieved from the stoichiometric coefficients given by the specified combustion reaction. The source term $\dot{m}_\alpha'''$ in each lumped species transport equation, presented in Equation (2.18), is modelled based on the Eddy Dissipation Concept (EDC) and the unmixed fraction formulation. It should be noted that the assumptions underlying the combustion model are independent of the extinction model.

Radiation

The default model in FDS for thermal radiation transport through a gaseous medium assumes no scattering, and considers only the absorption and emission of

radiation. To keep computation times within practical limits, the radiation spectrum is divided into a specified number of bands, for each of which a separate radiation transport equation is solved. The RadCal narrow band model is used to compute a single effective absorption coefficient for a given gas temperature and species composition [Grosshandler, 1993; McGrattan et al., 2005]. The effective absorption coefficient is assumed to be independent of wavelength and only a function of gas temperature, and composition, the path length, and the effective temperature of flame radiation.

The cell sizes typically used in the gas phase of most simulations are significantly larger than the thickness of the flame. This results in insufficient resolution of flame temperatures, which has a significant impact on the accuracy of predictions of the heat released as thermal radiation. As an alternative, FDS resorts to a prescribed radiative fraction, which determines the fraction of the total heat released by the fire as thermal radiation.

2.2 Input parameters of interest

The numerous sub-models that represent the physical and chemical phenomena in the simulations depend on a large number of parameters. In many cases, these parameters have no physical meaning and usually accompany empirical correlations implemented in CFD models to represent phenomena that are difficult to model or are not resolved by the grid. In other cases, these parameters are regarded as material properties, as they define the behaviour of fluids or solids under various physical conditions.

This study focuses on the latter, specifically on thermophysical and optical properties, as well as kinetic parameters. In FDS, they are required by the solid-phase solver as input variables. Most of these properties are grounded in fundamental physical laws and therefore carry physical meaning relevant to the models they are associated with. Below, short descriptions of the material properties that were considered in the sensitivity analyses conducted in this study are provided. They define how the heat transfer occurs within the solid phase and, in turn, influence the rates of pyrolysis and the predicted flame spread rate. Further details on the parameters composing the parameter sets investigated in this work will be given in relevant chapters, namely Chapters 3 and 4.

2.2.1 Thermophysical properties

The **specific heat capacity** $\boldsymbol{c}$, or simply specific heat, is generally defined as the property that determines the amount of heat required to raise the temperature of a

substance by one unit, per unit mass. In SI units, it is expressed in joules per kilogram per kelvin ($\mathrm{J\,kg^{-1}\,K^{-1}}$). It is a function of both temperature and pressure, and arises from the first law of thermodynamics applied to ideal gases, where it is defined as the derivative of enthalpy or internal energy with respect to temperature [Tester and Modell, 1997]. The specific heat is typically measured at either constant volume or constant pressure, and for solid materials, it is most commonly determined using, for example, a Bomb Calorimetry or a Differential Scanning Calorimetry (DSC).

The **thermal conductivity** $\boldsymbol{k}$ describes the rate at which heat is conducted through gases, liquids, or solids. It derives from Fourier's law of heat conduction as the proportionality constant between the heat flux and the temperature gradient, and is expressed in watts per metre per kelvin ($\mathrm{W\,m^{-1}\,K^{-1}}$) in SI units [Bird, 2002]. Although often approximated as a constant, it generally depends on temperature and pressure, particularly in gases and complex solid materials. In gases, it can be estimated using kinetic theory combined with experimental data, while in solids, it is typically measured using steady-state or transient techniques [Flynn et al., 2002; Assael et al., 2005; DiDomizio et al., 2024].

2.2.2 Optical properties

The **emissivity** $\boldsymbol{\varepsilon}$ is the ratio of thermal radiation emitted by a real surface to that of an ideal black body at the same temperature. It is a dimensionless parameter, equal to unity for a black body and less than unity for real, non-fluorescent surfaces [Bird, 2002]. Although emissivity can vary with wavelength and temperature, it is often approximated as a constant to simplify calculations, enabling direct application of the Stefan-Boltzmann law. This leads to the concept of gray bodies, which are idealised surfaces that emit radiation proportionally across all wavelengths [Drysdale, 2011]. The emissivity of solid materials, along with other radiative properties such as the refractive index and absorption coefficient, is commonly determined through spectroscopic measurements [Zhang et al., 2022; Boulet et al., 2014].

The **absorption coefficient** $\boldsymbol{\kappa}$ is the property that denotes the attenuation of radiative intensity as it penetrates in a medium per unit distance ($\mathrm{m^{-1}}$, in SI units). In its fundamental form, it appears as the proportionality constant in the monochromatic Beer–Lambert law, which describes the exponential decay of radiation at a given wavelength as it travels through an absorbing medium [Modest and Mazumder, 2021]. For the total (integrated) radiation spectrum, the absorption coefficient depends on wavelength, temperature, pressure, and composition. However, in most modelling

approaches, the gray gas (or gray body) approximation is applied, assuming the absorption coefficient is independent of wavelength [Wang et al., 2014].

The **refractive index** $\boldsymbol{n}$ of a medium is the ratio of the speed of light in vacuum to the speed of light in that medium. It is therefore a dimensionless optical property that indicates how much the speed of light is slowed down when passing through a medium compared to its speed in a vacuum. For absorbing media, it is often expressed as a complex number, where the real part is the refractive index as defined here, and the imaginary part is the medium absorptive index [Modest and Mazumder, 2021]. In FDS, refractive indices are only considered for particles and, in some FDS versions, it is accounted for in the 3D heat conduction solver. Although none of these models are used in this work, this parameter is introduced here because it belongs to the set of material parameters studied in Chapter 3, developed by Hehnen and Arnold [2023]. The developers of the investigated parameter set may have mistakenly included this parameter in the pyrolysis model, and therefore it is not expected to influence the simulation predictions analysed in this work.

2.2.3 Kinetic parameters

The Arrhenius law given in Equation (2.5) is one of the most fundamental relations in chemical kinetics. It is considered to date the most generalised approach to relate reaction rate and temperature [Arrhenius, 1889, 1967; Laidler, 1984]. Although it has been empirically derived, significant effort has been made to attribute physical meaning to the parameters A and E, on the basis of thermodynamics concepts, the kinetic theory of gases and statistical mechanics [Laidler and King, 1983]. The **pre-exponential factor** $\boldsymbol{A}$ is largely described as the factor representing the frequency of collisions between the reacting molecules, which is most commonly considered a constant parameter. The **activation energy** $\boldsymbol{E}$ is associated with the height of the energy barrier that needs to be overcome for the reaction to occur.

2.3 Sensitivity analysis

Sensitivity analysis refers to a set of techniques used to determine how variations in model inputs influence the model outputs. It is an essential component of uncertainty analysis and model evaluation, as it helps identify the most influential inputs and guides efforts in model simplification, parameter estimation, and experimental design [Saltelli et al., 2008].

An important aspect to consider when conducting sensitivity analysis is the selection of an appropriate method, as a distinction exists between local and global approaches. Local sensitivity analysis assesses the impact of small perturbations around a nominal set of input values. Although computationally inexpensive, it is limited to linear approximations and does not capture parameter interactions or non-linear effects. In contrast, global sensitivity analysis investigates the entire input space, accounting for the full range of variability in each parameter. As highlighted by Saltelli et al. [2008, 2019], global methods are more suitable for complex and non-linear models, as they can capture interaction effects and offer a more comprehensive understanding of the relationships between inputs and outputs.

For these reasons, the sensitivity analyses conducted in this work are based primarily on a global method, namely, the Sobol indices. This choice is well justified given the inherently non-linear nature of FDS, which integrates several coupled non-linear equations to model fire dynamics. Moreover, since the parameters are varied simultaneously during the inverse modelling and optimisation process, a global approach is necessary to account for potential interactions between parameters and to fully explore their influence on the model outputs.

2.3.1 Sobol indices

The sensitivity analyses performed in this work are mainly discussed in terms of the Sobol indices [Sobol, 2001; Saltelli, 2002], a robust global sensitivity analysis method based on the decomposition of variances. By varying input parameters simultaneously and not one at a time, the method is capable of quantitatively capturing interaction effects between input parameters on the model output of interest. It is therefore suitable for determining the sensitivities of non-linear and high-dimensional models, such as the complex flame spread models in question.

Sensitivities are determined based on the degree of contribution that a certain input parameter has to the uncertainty (variance) of the model output. It has been applied in the field of fire safety science to investigate the influence of inputs on environmental fire spread models [Ujjwal et al., 2021], and on the mass loss rate (MLR) calculated by the Arrhenius equation [Batiot et al., 2016].

In the mathematical formulation of the method proposed by Sobol [2001], the model can be described as a multivariable function $Y = f(\mathbf{X})$, where Y is a scalar output and $\mathbf{X} = (X_1, X_2, ..., X_k)$ is a point in a k-dimensional parameter space. If f is square-integrable, with independent inputs, it can be decomposed into terms of

increasing dimensions:

$$f = f_0 + \sum_i f_i(X_i) + \sum_i \sum_{j>i} f_{ij}(X_i, X_j) + \ldots + f_{12\ldots k} \quad . \tag{2.21}$$

Each individual term is a function only of the inputs in its index, that is, f_0 corresponds to the constant part of the function, $f_i = f_i(X_i)$ depends only on one component (here X_i) of the parameter vector $\mathbf{X}$, $f_{ij} = f_{ij}(X_i, X_j)$ depends on two components and so on. The total number of terms is equal to 2^k, out of each k terms are called first-order function f_i, f_{ij} are second-order functions, and so forth. Equation 2.21 can be squared and integrated to generate the decomposition of variances:

$$V(Y) = \sum_i V_i(X_i) + \sum_i \sum_{j>i} V_{ij}(X_i, X_j) + \ldots + V_{12\ldots k} \tag{2.22}$$

where the total variance of the output $V(Y)$ is split down into $2^k - 1$ different partial variances, each accounting for fractions of the output variance that is induced by the corresponding input, or combinations of inputs. For example, $V_i(X_i)$ is the induced variance on the output when X_i is varied alone, while $V_{ij}(X_i, X_j)$ is the induced variance when X_i and X_j are varied together. Two parameters are said to interact when their combined effect on the output is different from the sum of their single effects.

The Sobol indices are obtained by dividing each partial variance in Equation 2.22 by the total variance of the output $V(Y)$, giving:

$$\sum_i S_i + \sum_i \sum_{j>i} S_{ij} + \ldots + S_{123\ldots k} = 1 \tag{2.23}$$

where the indices S_i, S_{ij}, etc, are ratios varying from 0 to 1. Following a similar terminology used for the decomposition in Equation 2.21, different types of sensitivity indices are defined:

- S_i: first-order indices, provide a measure of main effects, i.e. the fractional contribution of X_i to the total variance of Y;
- $S_{ij..k}$: higher-order indices, measure interaction effects between the inputs indicated in their subscripts;
- ST_i: total-order indices, account for all the effects due to variations in X_i, i.e. first-order effects and interaction effects.

The indices provide a measure of importance of each input parameter by quantifying how much the variance of the output could be reduced if a given input parameter, or combination of parameters, could be fixed. For example, $S_i = 0.10$ means that 10% of the variance of the output could be reduced if X_i is fixed to a known value. Similarly, $ST_i = 0$ implies that X_i is non-influential and can be fixed anywhere in its distribution without affecting the variance of the output [Saltelli et al., 2008]. When interaction effects exist, the sum of all total-order effect indices is greater than unity.

As the number of sensitivity indices to be computed in Equation 2.23 increases exponentially with the number of input parameters, the calculation of high-order indices can become expensive. It is therefore convenient and often sufficient to express sensitivities in terms of first-order and total-order sensitivity indices. The difference between ST_i and S_i provide a measure of how much X_i is involved in interactions with any other input parameter.

For a better understanding, an example is given for a function of the form $Y = f(\mathbf{X})$ with $\mathbf{X} = (\mathrm{A,B,C})$, for which Equation 2.23 becomes:

$$S_\mathrm{A} + S_\mathrm{B} + S_\mathrm{C} + S_\mathrm{AB} + S_\mathrm{AC} + S_\mathrm{BC} + S_\mathrm{ABC} = 1 \tag{2.24}$$

where S_A, S_B, and S_C are the first-order indices, accounting for the main effects of A, B, and C respectively. The second-order indices S_AB, S_AC and S_BC account for the interaction effects between the pairs of inputs in their subscripts. Accordingly, S_ABC is the third-order index which accounts for the interaction effects on the output when A, B and C are varied together. In this example, the total-order indices of inputs A, B and C are given as:

$$ST_\mathrm{A} = S_\mathrm{A} + S_\mathrm{AB} + S_\mathrm{AC} + S_\mathrm{ABC} \tag{2.25}$$

$$ST_\mathrm{B} = S_\mathrm{B} + S_\mathrm{AB} + S_\mathrm{BC} + S_\mathrm{ABC} \tag{2.26}$$

$$ST_\mathrm{C} = S_\mathrm{C} + S_\mathrm{AC} + S_\mathrm{BC} + S_\mathrm{ABC} \tag{2.27}$$

in which the total effect of ST_i is the sum of all the terms in Equation 2.23 where the parameter X_i is considered.

In this work, the Sobol indices are calculated by means of two distinct methods. In Chapter 3, they are determined using quasi-Monte Carlo estimations [Saltelli, 2002]. In this approach, the indices are calculated by comparing simulation outputs generated from structured input samples, following a specific sampling scheme that will be introduced later in Chapter 3 in more detail [Saltelli, 2002].

The analysis presented in Chapter 4, on the other hand, is based on a surrogate model. The surrogate is constructed as a polynomial expansion [Sudret, 2008]. In

this approach, Sobol indices are derived analytically or semi-analytically from the coefficients of the surrogate model. This makes the estimation process far more computationally efficient than the approach used in Chapter 3, as only a small number of model evaluations (runs) are required to train the metamodel. Further details will be presented in Section 4.2.3.2.

Chapter 3

Transferability of effective properties estimated from cone calorimeter data

The contents of this chapter are based on the article entitled *Sensitivity analysis for an effective transfer of estimated material properties from cone calorimeter to horizontal flame spread simulations* [Quaresma et al., 2024].

3.1 Introduction

The cone calorimeter is a standard bench scale experimental apparatus widely used in the field of fire safety to measure the heat release rate (HRR) of combustible materials [Babrauskas, 1982]. Simply put, it consists of exposing a sample, often with dimensions of 10 cm × 10 cm, to a radiant heat flux generated by a conical heater. In addition to the HRR, the cone calorimeter can also be used to measure mass loss rate, time to ignition and effective heat of combustion [Babrauskas, 2016]. Because of its relative simplicity and low operating cost, it is one of the most commonly used apparatuses to characterise the reaction to fire of solid materials [for Standardization , ISO].

As previously discussed in Section 1.2.1, a common strategy for estimating the material properties required to model pyrolysis is to use data collected from cone calorimeter experiments in an inverse modelling process. The HRR, mass loss rate and rear surface temperatures of the sample are good examples of data from cone calorimeter experiments that have been used as targets in the optimisation [Lautenberger et al., 2006; L. et al., 2018; Hehnen and Arnold, 2023; Viitanen et al., 2022]. In this process, the optimisation algorithm works to find the set of input parameters

that leads to the closest fit between the simulation output and the experimental data. The fitness is evaluated by a cost function, which quantifies the deviation between the experimental targets and the simulated output [Lauer et al., 2020].

The ultimate goal of this strategy is to use the estimated parameter set, often viewed as a set of effective material properties, in a simulation model capable of predicting flame spread behaviour and fire growth. In other words, the estimated parameter set is *transferred* to the flame spread simulation model, as illustrated in Figure 3.1.

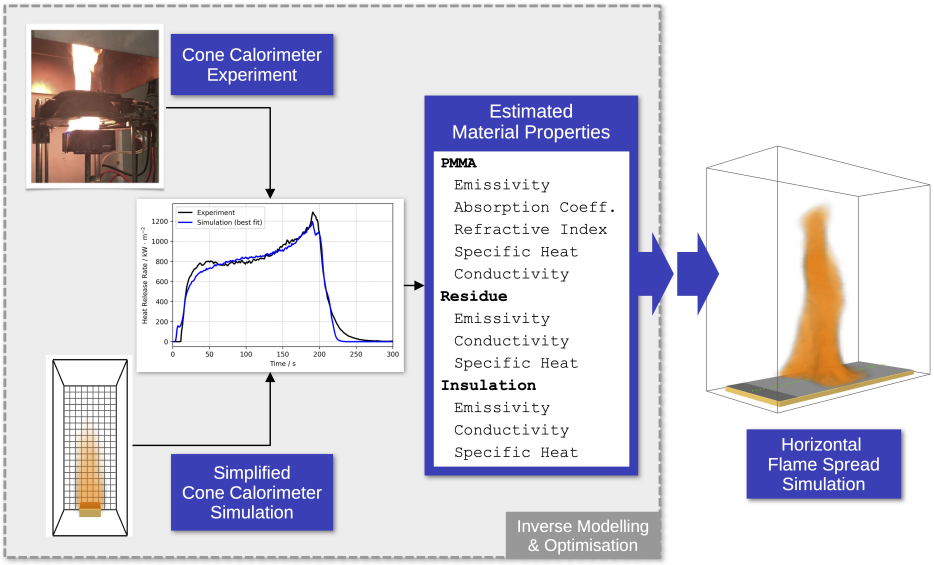

Figure 3.1: The set of effective material properties estimated in a inverse modelling process is transferred to a simulation model to predict flame spread behaviour.

The underlying assumption of the approach shown in Figure 3.1 is that the estimated parameters are transferable across inherently different setups. Yet, there are several factors that may challenge this assumption, particularly when the estimated parameter set is applied to larger scale flame spread simulations. A major limitation is that most bench-scale experiments are not designed to study flame spread. Cone calorimeter experiments, for example, are conducted under conditions where flame spread is either negligible or entirely absent, due to small sample sizes and uniform heating.

Furthermore, in most cases it is difficult to model the experimental conditions sufficiently well because of unknown boundary conditions or limitations in existing

sub-models. The use of fine grid resolutions is also restricted by the high computational cost of the optimisation process, which requires a large number of model runs. As a result, an estimated parameter set that provides a good fit to cone calorimeter data does not necessarily guarantee an equally satisfactory outcome when applied to flame spread simulations [Hehnen and Arnold, 2023]. Of course, it is important to keep in mind that low prediction accuracy can stem from various sources of error (e.g. inadequate representation of physical mechanisms, numerical errors) and is not solely attributable to uncertainties in the parameter sets.

In this context, a fundamental requirement for this transfer is that the simulation model used in the optimisation is sufficiently sensitive to the input parameters of interest. If the model lacks sensitivity to certain parameters, the estimated values will have higher associated uncertainty. This occurs because the optimisation algorithm can freely assign any value to insensitive parameters from their predefined sampling bounds, as their influence on the cost function is expected to be small. The main concern is that if such parameters are relevant to the flame spread simulation, their uncertainty will propagate through the model, potentially compromising the reliability of the predicted results when compared to experimental data.

This chapter focuses on addressing the following question: How sensitive is the cone calorimeter simulation to the parameters that are important to the target flame spread simulation? To answer this question, a methodology is proposed to compare the sensitivities of two representative simulation models – one for the cone calorimeter experiment and the other for flame spread – to the same set of input parameters. The goal is to use sensitivity analysis to identify potential discrepancies in the responses of each simulation model to the inputs, which can be used to improve the optimisation strategy and minimise uncertainties in the estimated parameters.

The cone calorimeter model selected for this investigation was developed and employed in a study by Hehnen and Arnold [2023] to estimate thermophysical and optical properties of PMMA and an insulation material. The flame spread simulation, developed specifically for the present study, represents a simplified sandbox setup, where a self-sustained flame spreads over a horizontal PMMA slab of bench-scale dimensions. The descriptions of the simulation models as well as the sensitivity analysis methodology are presented in the next section.

3.2 Methods

3.2.1 Cone calorimeter simulation

The parameter set investigated is taken from a previous study by Hehnen and Arnold [2023]. In their study, a full set of input parameters is determined in two independent inverse modelling steps. In the first step, the pyrolysis reaction scheme is designed, for which the kinetic parameters and heats of reaction are estimated. After the successful completion of the first step, thermophysical parameters are determined in the second step, using a simplified cone calorimeter simulation setup. Since the pyrolysis reaction scheme is considered fixed at this point, in the present study the focus lies only on this second step.

The simplified cone calorimeter simulation used in the present study was developed the in work of Hehnen and Arnold [2023]. To ensure consistency, all simulations presented in this chapter were performed using FDS version FDS6.7.6-810-ge59f90f-HEAD [McGrattan et al., 2005], which is the same version applied in the referenced study. The simulation model was originally developed to estimate PMMA properties through an inverse modelling process, using cone calorimeter experimental data as a target.

In the experiments, a square sample of black cast PMMA with an edge length of 10 cm and a thickness of 6 mm is exposed to a radiative heat flux of 65 $\mathrm{kW\,m^{-2}}$. A layer of insulation material, equal in surface area to the PMMA sample, is placed beneath it for thermal insulation, with a thickness of 2 cm. The experimental data used as target in the optimisation was provided by the Aalto University to the publicly available MaCFP database [Leventon et al., 2022].

The cone calorimeter simulation setup 'Cone_04', shown in Figure 3.2a, was designed to closely replicate the experimental conditions while keeping it simple due to the practical limitations of the optimisation process. In the simulation, the radiative heat flux is applied directly to the sample surface, eliminating the need to explicitly model the heater. To account for the non-uniform heating caused by the conical heating element, multiple surface regions with slightly varying heat flux values are defined, as illustrated in Figure 3.2b. Following a methodology proposed and described in their paper [Hehnen and Arnold, 2023], the heat flux distribution is derived from high-resolution simulations of the cone calorimeter experiment.

Among the various cone calorimeter models developed and studied by Hehnen and Arnold [2023], Cone_04 model was selected because of two main reasons. First, it provided a set of thermophysical and optical properties that resulted in the best fit to

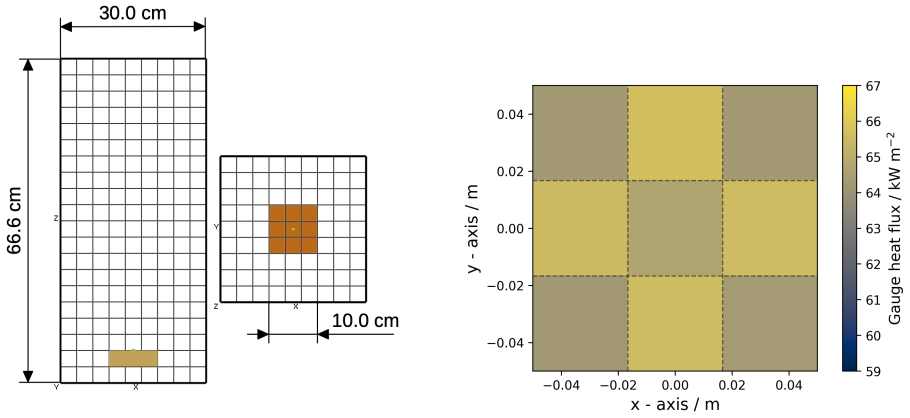

(a) (b)

Figure 3.2: The simplified cone calorimeter simulation, 'Cone04', used by Hehnen and Arnold [2023] for estimating PMMA properties. (a) Overview of setup; (b) Uneven heat flux applied to the sample surface.

the target data during the optimisation, which is shown in Figure 3.3a. Additionally, when these estimated properties were applied to a real-scale flame spread simulation of the parallel panel experiment, they produced the most accurate prediction of the experimental HRR, as can be seen in Figure 3.3b.

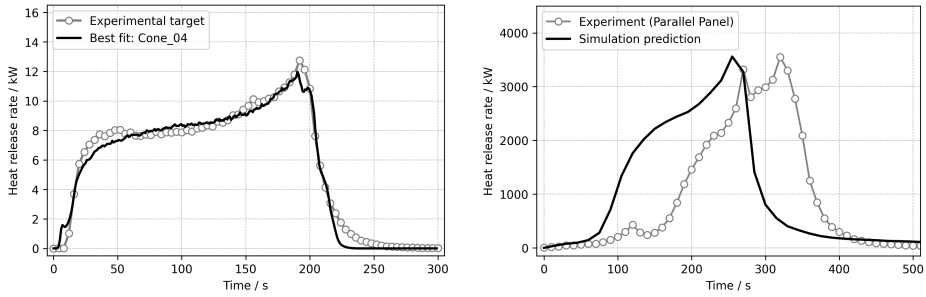

(a) (b)

Figure 3.3: Performance of the parameter set estimated using Cone_04. (a) Best fit in the optimisation to target cone calorimeter data; (b) Validation against the Parallel Panel experiment [Hehnen and Arnold, 2023].

The coarse gas cell resolution of 3.33 cm was chosen due to the large number of simulations required during the optimisation process [Hehnen and Arnold, 2023].

Yet, it is important to emphasise that Cone_04 model employs a higher resolution compared to similar approaches in the field, where cone calorimeter models have also been used for material property estimation. Studies by Viitanen et al. [2022], Hehnen et al. [2020], McCoy et al. [2019], and Beji and Merci [2019] used gas cell sizes of 5 cm or larger, whereas Cone_04 applies a finer resolution of 3.33 cm, as illustrated in Figure 3.2.

3.2.1.1 Gas-phase grid sensitivity

In order to evaluate the effect of gas-phase grid sizes on the sensitivities to inputs, three additional simulation cases were derived from the reference case Cone_04, each using a different gas cell size. The gas cell sizes were chosen based on the feasibility of implementing these resolutions in a model suitable for optimisation in terms of computational cost [Hehnen and Arnold, 2023]. The objective of this analysis is to assess whether the sensitivities to input parameters remain consistent across different resolutions that could be used in an optimisation framework.

Following the terminology proposed by Hehnen and Arnold [2023], Cone_04 is here designated as C3, referring to the 3×3 division of the sample surface, as illustrated in Figures 3.2a and 3.2b. The first alternative case, C2 (2×2 divisions), corresponds to 5 cm gas cells. The second, C5 (5×5 divisions), features 2 cm gas cells, while the third, C7 (7×7 divisions), employs 1.43 cm gas cells. The heat flux mapping applied to the sample surface is adjusted for each resolution (C2, C5, and C7) and is presented in Appendix A, Section A.3.

It is important to note that C5 and C7 represent refinements that would impose a significant computational burden in an optimisation setting. For this reason, resolutions finer than C7 were not explored. The heat release rate (HRR) predicted for cases C2, C5, and C7, alongside the reference C3 (Cone_04), is shown in Figure 3.4.

As can be seen in Figure 3.4, the simulated HRR is slightly affected by grid refinement in the gas phase. The overall trend of the curve is preserved, with the primary effect being a shift to earlier times of the HRR peak as resolution increases. Given this, the relative importance of input parameters to the simulated HRR is expected to remain consistent across the tested gas cell sizes. Nonetheless, a sensitivity analysis was performed for the C2 and C5 cases in addition to the reference C3 case.

3.2.1.2 Solid phase modelling

The pyrolysis reaction mechanism employed by Hehnen and Arnold [2023] to describe PMMA decomposition considers a single-step, first-order reaction model. In this

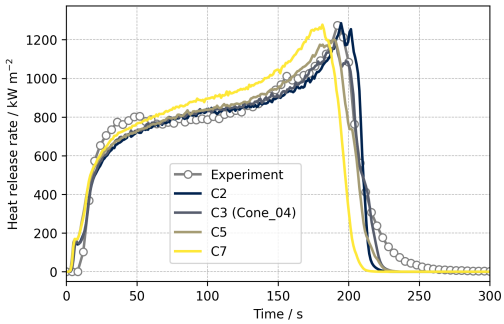

Figure 3.4: Effect of different gas-phase grid resolutions on the simulated HRR of the simplified cone calorimeter simulation.

approach, PMMA is assumed to decompose into a mixture of combustible gases (Fuel Mixture) and a small fraction of solid residue, as illustrated in Figure 3.5.

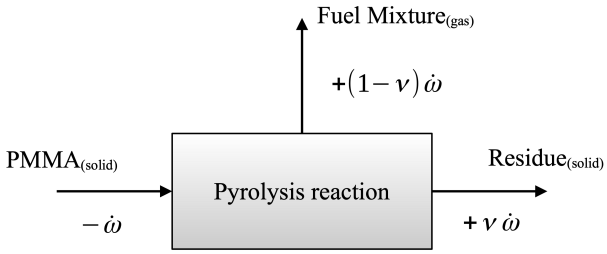

Figure 3.5: Schematic representation of a single-step reaction mechanism of PMMA pyrolysis. Adapted from Batiot et al. [2016].

The rate of PMMA decomposition is denoted by $\dot{\omega}$ in Figure 3.5. The rate of production of Fuel Mixture is then given by $(1-\nu)\dot{\omega}$, where ν is the solid residue yield, taken as 1 %. The reaction rate $\dot{\omega}$ follows the general formulation presented earlier in Equation 2.6, which is expressed as the product of the Arrhenius law (Equation 2.5) and the reaction rate function $f(\alpha)$ (Equation 2.7). The Fuel Mixture is assumed to consist of methane, ethylene and carbon dioxide, and the Residue is assumed to be an inert solid product.

As a strategy to achieve a better fit to the experimental data, it was assumed that different fractions of the virgin PMMA sample decompose at different rates, as described in [Hehnen and Arnold, 2023]. In the FDS implementation, this is represented by eight separate decomposition reactions. However, each of these reactions actually

follows the same underlying mechanism shown in Figure 3.5, with a fixed residue yield. They only differ in terms of kinetic parameters (A and E), heat of pyrolysis, and mass fractions. The kinetic parameters, heat of pyrolysis, and corresponding PMMA mass fractions were determined in an initial optimisation step, using MCC and TGA data as targets [Hehnen and Arnold, 2023]. In this same step, the volume fractions of the gas species composing the Fuel Mixture were also determined. In the analysis presented in this chapter, the kinetic parameters remain fixed and do not take part in the sensitivity analysis.

The set of material properties of interest, estimated using Cone_04, is presented in Table 3.1. It includes the thermophysical and optical properties of PMMA, the insulation material, and the pyrolysis residue, which total 15 input parameters. The input parameters related to the pyrolysis kinetics of the sample, which are not included in the analysis, are provided in Table A.1.

Table 3.1: Set of effective material properties estimated using Cone_04 [Hehnen and Arnold, 2023].

	Material	Parameter	Estimated value	Unit
1	PMMA	Emissivity	0.94	-
2		Absorption coefficient	7979	$\mathrm{m^{-1}}$
3		Refractive index	2.85	-
4		Conductivity at 150 °C	0.38	$\mathrm{W\,m^{-1}\,K^{-1}}$
5		Conductivity at 480 °C	0.02	$\mathrm{W\,m^{-1}\,K^{-1}}$
6		Conductivity at 800 °C	4.34	$\mathrm{W\,m^{-1}\,K^{-1}}$
7		Specific heat at 150 °C	0.77	$\mathrm{kJ\,kg^{-1}\,K^{-1}}$
8		Specific heat at 480 °C	3.81	$\mathrm{kJ\,kg^{-1}\,K^{-1}}$
9		Specific heat at 800 °C	7.28	$\mathrm{kJ\,kg^{-1}\,K^{-1}}$
10	Residue	Emissivity	0.55	-
11		Conductivity	4.51	$\mathrm{W\,m^{-1}\,K^{-1}}$
12		Specific heat	5.89	$\mathrm{kJ\,kg^{-1}\,K^{-1}}$
13	Backing	Emissivity	0.44	-
14		Conductivity	2.41	$\mathrm{W\,m^{-1}\,K^{-1}}$
15		Specific heat	4.07	$\mathrm{kJ\,kg^{-1}\,K^{-1}}$

The PMMA properties considered are emissivity, absorption coefficient, refractive index, specific heat, and thermal conductivity. Both thermal conductivity and specific heat are defined as temperature-dependent values, following a piecewise linear function with reference points at 150 °C, 480 °C, and 800 °C, as shown in Figure 3.6. The property values at temperatures between the reference points are determined

by FDS through linear interpolation. For temperatures outside the given range, the property values are assumed constant, equal to the first or last specified value.

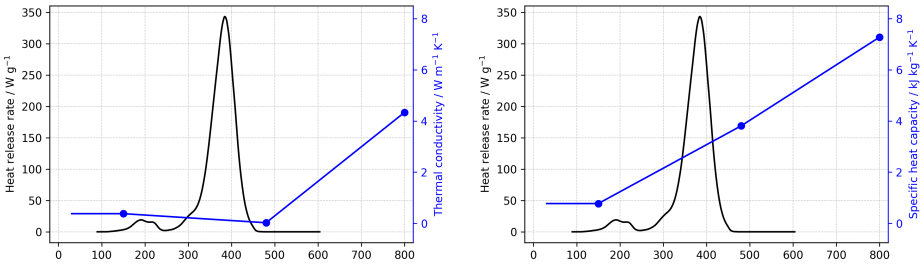

(a) (b)

Figure 3.6: Piecewise linear functions for (a) thermal conductivity and (b) specific heat of PMMA. The experimental MCC data is plotted to highlight the temperature range at which the material pyrolyses.

In Figure 3.6, the MCC data is included on a secondary y-axis to highlight the temperature range associated with PMMA decomposition. It is worth noting that although 800 °C exceeds the upper temperature limit indicated by the MCC data (600 °C), this point helps to estimate values within the 480 °C to 600 °C range. However, as the MCC data shows that PMMA is almost completely degraded below 500 °C, the 800 °C point is expected to have little or no effect on the simulation results. In contrast, as most PMMA degradation occurs between 150 °C and 500 °C, material property values within this range are expected to have a more significant influence.

The value of PMMA density was directly calculated from reported mass and dimensions of the sample. Density of the residue was fixed to an arbitrary value due to lack of information, and density of the insulation material was taken from the MaCFP database [Leventon et al., 2022]. The material definition in the FDS input file is provided in Section A.2.

The default one-dimensional heat conduction model in FDS, previously described in Section 2.1.1, was used. To prevent numerical instability, the solid-phase solution is updated at every time step by setting `WALL_INCREMENT` to 1.0. The node spacing in the PMMA layer is uniform, whereas the insulation material layer follows the default stretched node spacing.

The default FDS grid resolution in both layers is increased by a factor of 10 by setting the `CELL_SIZE_FACTOR` to 0.10. As a result, the PMMA layer is discretised into 96 equally spaced cells, while the insulation material layer is divided into 11 stretched

cells. However, the cell size in the PMMA layer is automatically redefined during the simulation, as temperature-dependent parameters influence thermal diffusivity and layer thickness changes due to sample consumption.

3.2.1.3 Gas phase modelling

The sub-models used to represent the gas phase in the simplified cone calorimeter simulation were previously described in Section 2.1.2. The combustion of the Fuel Mixture is assumed to be mixing-controlled, with a soot yield of $0.022\,\mathrm{g\,g^{-1}}$, taken from Quintiere [1998]. The radiative fraction, which determines the portion of total heat release emitted as thermal radiation, is automatically set by FDS to 0.35, which is the default value for unspecified species. The initial ambient temperature is set to 30.85 °C, matching the conditions reported in the experiment.

The computational domain extends in the x- and y-directions from $-15\,\mathrm{cm}$ to $15\,\mathrm{cm}$, and in the z-direction from $-6.6\,\mathrm{cm}$ to $60.0\,\mathrm{cm}$. A uniform grid is defined by assigning $9 \times 9 \times 20$ cells in the x-, y-, and z-directions, respectively, resulting in cells of $3.33\,\mathrm{cm}$ edge length. A single mesh is used for the entire domain, with open boundary conditions. The centre of the sample is positioned at the origin $(0, 0, 0)$. The sample holder is modelled as an inert obstruction with an edge length of $10\,\mathrm{cm}$ in the x- and y-directions and $3.33\,\mathrm{cm}$ in the z-direction. An overview of the geometry, domain, and mesh resolution is shown in Figure 3.2a.

In this subsection, concise descriptions of the cone calorimeter modelling were provided, focusing on the aspects that are most relevant to this work. For further details and additional resources, the reader should refer to Section 2.1, the original work by [Hehnen and Arnold, 2023] and to the FDS User's Guide [McGrattan et al., 2005].

3.2.2 Horizontal flame spread simulation

The flame spread simulation considered in the sensitivity analysis represents a simplified horizontal configuration, in which a self-sustained spread develops over a slab of PMMA. No influence of ventilation or wind conditions is considered, ensuring that the flame is not affected by external flow disturbances.

The solid phase modelling in the flame spread simulation is taken directly from the cone calorimeter simulation. This means that the PMMA sample definition, pyrolysis scheme, insulation material and solid phase resolution are the same as described in Section 3.2.1, which also includes the parameter set in Table 3.1. This consistency

is essential as the primary objective of this work is to compare the responses of both simulations to variations in the same set of material properties taken as input parameters.

In the flame spread setup, the PMMA sample is placed on top of an inert ochre obstruction, which serves as a sample holder (see Figures 3.7a and 3.7b). The sample dimensions are 23 cm × 9.5 cm × 0.6 cm, and an external heat flux of 65 kW m^{-2} is applied for 100 s to an area of 2.5 cm × 9.5 cm to initiate ignition. The ignition area is located at the left end of the sample and is represented by the dark brown patch in Figures 3.7a and 3.7b.

The dimensions of the computational domain are 26 cm × 12.5 cm × 11 cm, divided into 26 meshes of 2.0 cm × 12.5 cm × 5.5 cm each to enable parallel computation. The gas cell size for the flame spread simulation is set to 5 mm. The gas-phase modelling differs from the cone calorimeter simulation only in terms of cell size. The simulation mode, combustion, and radiation modelling follow the same approach as in the cone calorimeter simulation, as described in Section 3.2.1. An overview of the horizontal flame spread simulation is presented in Figure 3.7.

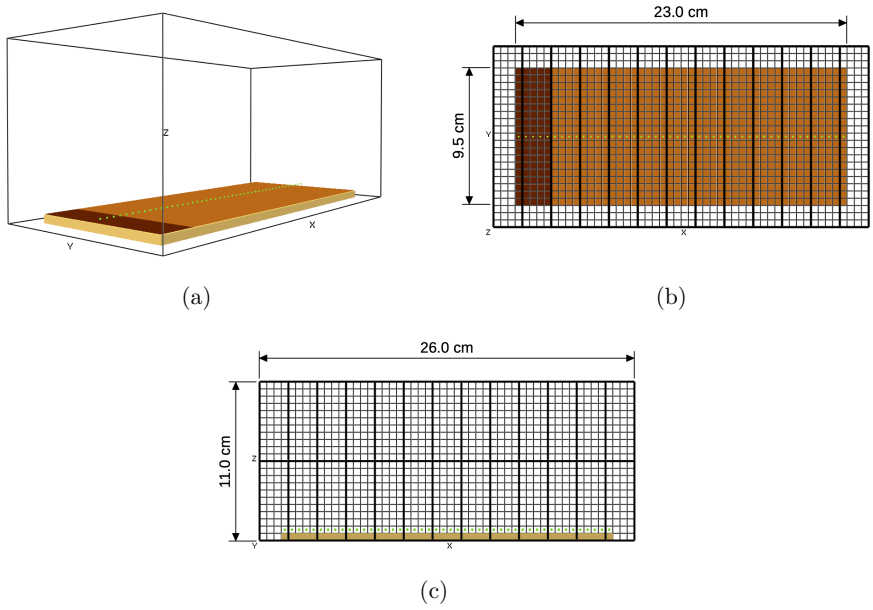

Figure 3.7: Overview of the horizontal flame spread simulation, showing the gas phase grid resolution, meshes and dimensions. Bold lines indicate mesh borders. (a) Perspective view; (b) Top view; (c) Side view.

Given its dimensions, the horizontal flame spread simulation can be viewed as a simplified small-scale setup, comparable in scale to the cone calorimeter simulation. An external heat flux of $65\,\mathrm{kW\,m^{-2}}$ is applied to the dark brown patch for 100 s to start ignition. This heat flux is intentionally set to the same value used in the cone calorimeter. These similarities enable the flame in the flame spread simulation to transition from the ignition stage – where sample heating is modelled as in the cone calorimeter model – to a self-sustained stage of spread.

To establish a reference flame spread simulation case, the set of material properties used in Cone_04 was transferred to the horizontal flame spread setup. The cell size of 5 mm was found to be the largest size among the tested ones that allowed sustained flame propagation over the sample. Several attempts were made with larger cell sizes (3 cm, 2 cm, 1 cm) but in these cases the flame did not spread significantly beyond the ignition zone and extinguished shortly after the external heat flux was cut off.

Testing a higher grid resolution with 2.5 mm cells resulted in an increased HRR and a higher spread rate compared to the 5 mm case, indicating that grid independence was not achieved. Grid dependence in flame spread simulations based on material pyrolysis appears to be a current limitation of FDS. This issue has been attributed to the approaches implemented in FDS to compute the convective heat transfer coefficient. At such fine grid resolutions, FDS computes the convective heat transfer based on temperature gradient at the sample surface and the size of the gas cell adjacent to the wall [McGrattan and Floyd, 2021; Maragkos and Beji, 2021; Dehghani et al., 2025].

Figure 3.8 presents slices of HRR per unit volume (HRRPUV) taken along the central plane of the domain ($y = 0$) along the x-axis at different time points. The magenta-coloured patches in the slices indicate the leading edge of the flame, defined here as the gas cell containing the maximum HRRPUV value in the one-dimensional row of gas cells in contact with the sample surface.

The HRRPUV slices in Figure 3.8 were generated using `fdsreader` version 1.9.9, an open-source Python module developed for reading FDS output data [Vogelsang and Arnold, 2023].

3.2.2.1 Determining the rate of spread (ROS)

The ROS is an important quantity to represent the flame spread phenomenon in the context of fire safety, because it describes how fast a fire can grow in a compartment, impacting the degree of damage and the time to reach flashover for example. Because of that, it is important to consider the ROS as one of the simulation outputs of interest,

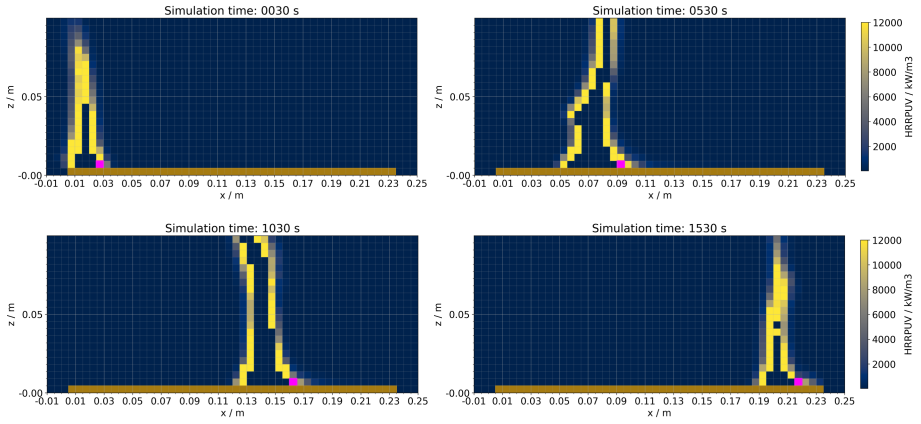

Figure 3.8: Slices at $y = 0$ showing the HRRPUV of the reference flame spread simulation, at different points in time. The gas cells coloured in magenta indicate the flame leading edge.

in addition to the temporal development of the simulated HRR. However, the ROS is not a direct output of the simulation software, and an additional post-processing step is required to determine it.

The flame leading edge is defined as the gas cell with the highest HRRPUV value along the centreline of the sample, in the row of cells adjacent to the sample surface. Initially, at time step zero, the leading edge is located at $(x = 0, z = 0)$, which serves as the first reference point. For subsequent time steps, the search for the maximum HRRPUV value is restricted to positions ahead of the last recorded location, only along the row of cells adjacent to the sample surface. This ensures that only the leading edge is tracked, preventing any HRRPUV maxima from being mistakenly identified at the trailing edge of the flame. In FDS, the values of HRRPUV can be read either from slice files, as shown in Figure 3.8, or from multiple devices that can be positioned along the centre line of the sample, as indicated by the green dots in Figures 3.7 and 3.9a.

The recorded positions of the leading edge were plotted against time for the reference simulation case, as shown in Figure 3.9a. Small plateaus in the black curve indicate intervals where the flame leading edge remains stationary. The vertical blue dashed line at 100 s marks the end of ignition, when the external heat flux is removed. The resulting trend suggests the existence of three distinct spread zones: (1) ignition, (2) self-sustained spread, and (3) extinction, influenced by the end of the

sample. These spread zones are visually marked on the sample in the simulation, as illustrated in Figure 3.9b, after being identified in the plot.

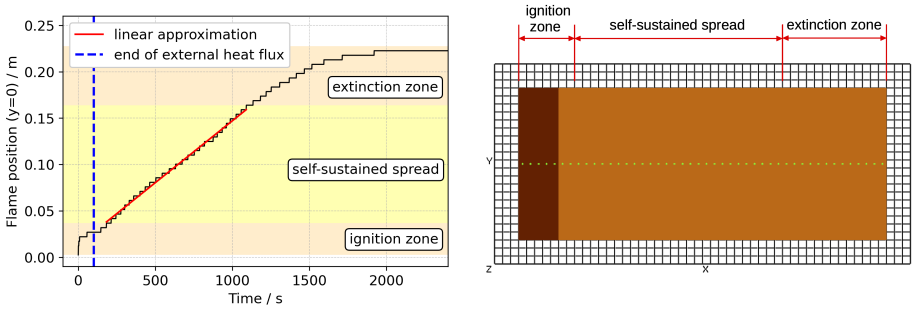

(a) (b)

Figure 3.9: Determining the ROS for the reference case of the horizontal flame spread simulation. (a) Flame position (leading edge) *vs* time; (b) Zones of spread.

Excluding the ignition and extinction zones, the change in position of the flame leading edge over time during the self-sustained phase can be reasonably approximated by a linear function, represented by the red curve in Figure 3.9a. The ROS is then determined as the angular coefficient of this linear function.

3.2.3 Sensitivity Analysis

The sensitivity analyses conducted in this chapter follow the methodology of the Sobol sensitivity indices, a global sensitivity analysis method based on the decomposition of variances [Sobol, 2001]. For analytical models, the integrals related to the calculation of variances can be solved also analytically. However, this is not the case for the simulation models investigated in this work.

The approach used here for estimating the indices assumes that the simulation model is a "black box", and no information on model behaviour is known other than what is perceived through variations in the model's inputs and outputs. The partial variances are calculated by quasi-Monte Carlo estimates and therefore a large number of simulations needs to be conducted, one for each sample of model inputs [Saltelli, 2002].

Input parameters are assumed to be independent and uniformly distributed within their sampling limits, and samples of parameters are generated by employing the Saltelli's sampling scheme [Saltelli, 2002], which is based on the Sobol sequence. The

Sobol sequence is a type of low-discrepancy quasi-random sequence that creates an efficient space filling sampling of the high dimensional parameter space. The sensitivity analyses, including sampling, estimation of the indices and confidence intervals, are carried out within the SALib Python library (version 1.4.5) [Iwanaga et al., 2022; Herman and Usher, 2017].

The confidence intervals for the sensitivity indices are calculated using the bootstrap resampling technique. This method involves generating multiple resampled datasets by randomly selecting and replacing data points from the original dataset. Sensitivity indices are then computed for each resampled dataset, creating a distribution of indices. The standard deviation of these resampled sensitivity indices is calculated, and confidence intervals are established based on a confidence level of 95 %. These intervals provide an estimate of the uncertainty associated with the sensitivity indices, indicating the range within which the true values are likely to lie.

The sampling limits of the 15 input parameters were defined by taking 15 % of variation around the best parameter set, which are presented in Table 3.1. A restriction is imposed only for the upper limit of emissivity, such that it would not exceed the value of 0.99. The sampling limits and units of each input parameter are shown in Table 3.2. In order to achieve better uniformity, the sampling scheme requires the number of samples N to be generated as powers of 2, i.e. $N = 2^q$, particularly when sampling high-dimensional parameter spaces.

The effect of sample size on the accuracy of Sobol index estimation was analysed for the cone calorimeter simulation. The indices were computed using sample sizes of 2^{13}, 2^{14}, 2^{15}, 2^{16}, and 2^{17}. The estimation quality is assessed through the confidence intervals of the indices, which are wider for smaller sample sizes and progressively narrow as the number of samples increases. The results for all sample sizes are presented, however the main discussion focuses on the largest sample size, 2^{17}, as it provides the most reliable estimates. Based on the results obtained for the cone calorimeter case, the number of samples for the flame spread simulation was set to $q = 15$. A smaller sample size was chosen due to the significantly higher computational cost of the flame spread simulation.

The main objective of the sensitivity analyses in this chapter is to compare how the two reference simulation cases – the simplified cone calorimeter and the flame spread simulation – respond to variations in the same set of input parameters. This parameter set is composed by 15 effective material properties and is listed in Table 3.1. The sensitivity of each reference simulation case is assessed by evaluating the effects

Table 3.2: Sampling limits and units of the input parameters considered in the sensitivity analyses.

	Material	Parameter	Sampling limits	Unit
1	PMMA	Emissivity	[0.80; 0.99]	-
2		Absorption coefficient	[6782; 9176]	m^{-1}
3		Refractive index	[2.43; 3.28]	-
4		Conductivity at 150 °C	[0.32; 0.44]	$W\,m^{-1}\,K^{-1}$
5		Conductivity at 480 °C	[0.02; 0.03]	$W\,m^{-1}\,K^{-1}$
6		Conductivity at 800 °C	[3.69; 4.99]	$W\,m^{-1}\,K^{-1}$
7		Specific heat at 150 °C	[0.66; 0.89]	$kJ\,kg^{-1}\,K^{-1}$
8		Specific heat at 480 °C	[3.24; 4.38]	$kJ\,kg^{-1}\,K^{-1}$
9		Specific heat at 800 °C	[6.18; 8.37]	$kJ\,kg^{-1}\,K^{-1}$
10	Residue	Emissivity	[0.47; 0.64]	-
11		Conductivity	[3.83; 5.19]	$W\,m^{-1}\,K^{-1}$
12		Specific heat	[5.01; 6.78]	$kJ\,kg^{-1}\,K^{-1}$
13	Backing	Emissivity	[0.38; 0.51]	-
14		Conductivity	[2.05; 2.77]	$W\,m^{-1}\,K^{-1}$
15		Specific heat	[3.46; 4.68]	$kJ\,kg^{-1}\,K^{-1}$

that changes in input parameters induce in selected simulation predictions, which are here referred to as outputs of interest:

- the HRR predicted by the simulations;
- the ROS, calculated for the flame spread simulation;
- and the RMSE, calculated between the simulated HRRs of the cone calorimeter setup and the measured HRR.

Therefore, the influences of the 15 input parameters on two types of outputs are evaluated, namely 'multiple-value' and 'single-value' outputs. The simulated HRR is a time-series, therefore it is a multiple-value output. In this case, the sensitivity indices are calculated at every point in time, and, consequently, are presented also as time-series. This is convenient to evaluate how the influence of a given input parameter varies over the course of the simulation.

With respect to the single-value outputs, two indirect quantities are calculated from the simulated HRRs: the RMSE for the cone calorimeter; and the ROS for the flame spread simulation, see Section 3.2.2.1. Here, the RMSE is calculated as:

$$\mathrm{RMSE} = \sqrt{\frac{1}{N}\sum_{i=1}^{N}\left[\mathrm{HRR}_{(\mathrm{simulated})i} - \mathrm{HRR}_{(\mathrm{measured})i}\right]^2} \tag{3.1}$$

where N is the number of points in the HRR curve, and the $HRR_{(measured)}$ is the experimental HRR curve shown in Figure 3.3a, which was used as the target for optimisation in earlier work [Hehnen and Arnold, 2023].

Table 3.3 shows for each simulation setup the outputs of interest taken in the sensitivity analyses, their type, and how the Sobol indices will be presented.

Table 3.3: Simulation outputs of interest considered in the sensitivity analyses.

Simulation setup	Output of interest	Type of output	Sobol indices presented as
Cone calorimeter	HRR	multiple-value	time-series
	RMSE	single-value	bar plots
Flame spread	HRR	multiple-value	time-series
	ROS	single-value	bar plots

The Sobol indices provide a simple and concise way of ranking the input parameters according to their importance by providing a quantitative measure of the sensitivities. This is advantageous when dealing with multidimensional parameter spaces. However, the indices do not provide the type of relationship (i.e. linear, non-linear) between the model output and each input, which is also a meaningful aspect of the analysis. This gap is filled by a complementary qualitative analysis using scatter plots. The scatter plots aim to show the relationship between the output and the two most influential parameters previously identified by the indices. Only single value outputs (RMSE and ROS) are considered in the scatter plot analysis.

3.3 Results and discussion

3.3.1 Effects on the HRRs

The effects of the 15 input parameters on the HRRs of the cone calorimeter and flame spread simulations are analysed through the time-series of the total-order (ST) and first-order (S1) sensitivity indices. The ST and S1 indices for the cone calorimeter simulation are presented in Figure 3.10. For the flame spread simulation, Figure 3.12 shows the ST and S1 indices calculated up to the initial 300 s, while Figure 3.13 presents the indices calculated up to 2000 s of the simulated HRRs.

In these plots, confidence intervals are shown as shaded areas around the solid curves, representing the uncertainty in the estimation of the sensitivity indices. The shaded regions for the cone calorimeter case are noticeably narrower than those for the

flame spread case. This difference stems from the sample sizes used in each analysis: the cone calorimeter indices were estimated using a larger sample size (2^{17}), resulting in tighter confidence bounds, while the flame spread case, based on a smaller sample size (2^{14}), shows broader intervals reflecting greater uncertainty. The effect of sample size on the estimation of the indices related to the cone calorimeter simulation is given in Figure 3.11.

3.3.1.1 Cone calorimeter simulation

As can be seen in Figure 3.10a, within the initial 5 s of the cone calorimeter simulation, only three parameters have non-zero ST indices: PMMA emissivity, conductivity at 150 °C and specific heat at 150 °C. Given that the ST indices provide the overall influence of the parameters on the model output, this means that these are effectively the only parameters affecting the HRR up to this point in time, whereas all the other parameters remain unimportant. At about 10 s, the importance of the specific heat at 150 °C momentarily drops, while the influence of the same property at 480 °C increases.

This can be explained by the dependency of the specific heat on temperature, established by the piecewise linear function. As the sample heats up, higher temperatures are reached, causing the value of the property to change, and consequently its influence over the HRR. Soon after that, at about 25 s, the importance of the specific heat at 150 °C increases again, and it becomes, together with the specific heat at 480 °C, the two most important parameters to affect the HRR of the cone calorimeter. At the same time, the initial total-order effects of PMMA emissivity and conductivity decrease to a practically negligible value for the rest of the simulation time.

It is important to distinguish, however, two stages of influence of the values of specific heat on the HRR, which become evident when Figures 3.10a and 3.10b are compared. The stages are defined by the nature of the effects of the input parameters on the HRRs, which is related to how the difference between the ST and S1 indices of each parameter change over time. That is, the degree of interaction effects among the parameters can be obtained from the difference between ST and S1 indices, as previously illustrated in Section 2.3 by Equations 2.25, 2.26, and 2.27.

In the first stage, ranging from about 25 s to 120 s, the difference between ST and S1 is small, indicating that the interaction effects are also small. This implies that the HRR is affected predominantly by first-order effects of the two parameters, expressing that the effects of changing them individually is dominant to the HRR at this stage. In the second stage, from 120 s to 150 s, an approximately synchronised and significant

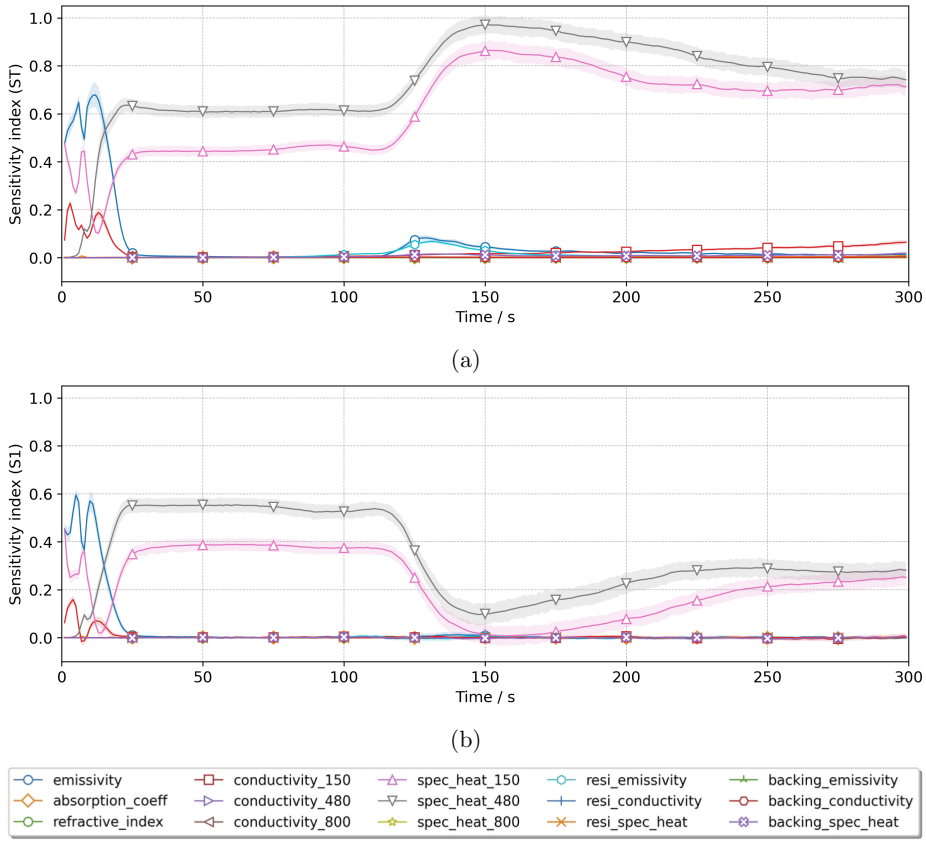

Figure 3.10: Time-series of the (a) ST and (b) S1 sensitivity indices, indicating respectively the total- and first-order effects on the HRRs of the cone calorimeter simulation.

increase of the ST indices is observed. At the same time, their corresponding S1 indices decline in a similar trend, as presented in Figure 3.10b. This large discrepancy between ST and S1 from 120 s to 150 s, together with the fact that all the other parameters have ST indices close to zero, indicate that strong interaction effects between the values of specific heat at 150 °C and at 480 °C dominate the HRR from this point forward in the cone calorimeter simulation. Still, at around 125 s, a timid increase in the ST indices of the PMMA samples and the emissivity of the residue are almost solely related to interaction effects, given that their correspondent S1 indices are very close to zero.

In addition to revealing differences between the cone calorimeter and the horizontal flame spread setups, the sensitivity analysis on the cone calorimeter disclosed that

only 4 out of 15 input parameters have non-negligible influences. In terms of thermo-physical properties, these four parameters are in fact three: emissivity, conductivity, and specific heat of the PMMA sample. This observation is similar to the results found in the work of Fleurotte et al. [2022], who conducted a sensitivity analysis based on the Morris method to determine which parameters are more important to the HRR of a cone calorimeter model.

In their work, PMMA emissivity and specific heat capacity are among the most influential parameters, along with activation energy and density. Yet, it is important to bare in mind that other parameters which were not included in the sensitivity analyses can play a significant role in the model, and their effects on the output must be assessed in case they are included in the optimisation strategy. Thus, ranking the parameters according to their importance allows for model simplification, by excluding the non-influential inputs and/ or fixing them in the optimisation. This approach can potentially reduce the computing time by orders of magnitude, depending on the characteristic of the optimisation method used [Hehnen and Arnold, 2023].

Sensitivities across gas-phase resolutions

In addition to the C3 case, the sensitivity analysis was performed for the C2 and C5 resolutions. For brevity, results for the C2 and C5 cases are not shown here but are available in Appendix A, Section A.3. As expected, the sensitivity indices were highly consistent across these cases, confirming that the HRR response to input parameters remains stable across the evaluated gas-phase grid resolutions. The C7 case was excluded due to its significantly higher computational cost. However, given the similarity in HRR profiles shown in Figure 3.3a and the consistent sensitivities observed for C2, C3, and C5, it is reasonable to assume that the C7 case would exhibit similar parameter sensitivities. Therefore, only the sensitivity analysis results for the reference case (C3, Cone_04) are presented and discussed.

Effect of sample size

The effect of sample size on the estimation of the sensitivity indices for the cone calorimeter simulation was analysed using 2^{13}, 2^{14}, 2^{15}, 2^{16}, 2^{17} samples. As previously discussed, increasing the number of samples improves the estimation of the indices, as indicated by narrower confidence intervals. This trend is illustrated in Figure 3.11, where the mean confidence intervals of the ST indices for the 15 input parameters decrease exponentially as the sample size increases. The x-axis is in log scale, base

2. The mean confidence intervals were computed by averaging the values associated with the ST indices over 300 s of the HRR simulations.

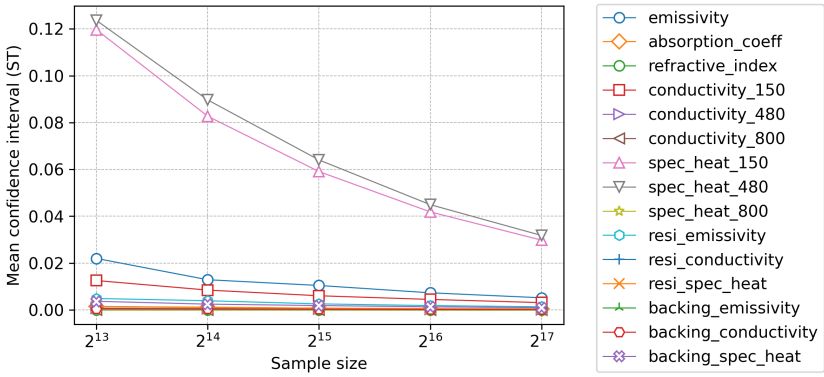

Figure 3.11: Effect of sample size on the estimation of the Sobol indices for the cone calorimeter simulation.

Although sufficiently accurate estimations were achieved with 2^{14} samples, results for the cone calorimeter are presented and discussed in this section based on the 2^{17} sample case. Results for smaller sample sizes are provided in Appendix A, Section A.4.

3.3.1.2 Flame spread simulation

The vertical blue dashed line at 100 s in Figures 3.12 and 3.13 marks the end of the external heat flux and thus the transition from the ignition phase to the phase where the spread is self-sustained. From these figures a clear transition from one phase to another can be observed, which is highlighted by an abrupt change in the importance of some parameters.

The initial 100 s in these figures present very similar trends to those observed in Figure 3.10, where the indices express the effects of input parameters on the cone calorimeter HRRs. This similarity is explained by the way the dark brown part of the sample is ignited, through the application of the external heat flux, as introduced in Section 3.2.2. Since this heating approach is identical to that used in the cone calorimeter, where the entire sample is exposed to the external flux, the sensitivity indices in this stage were able to effectively capture the similarity in modelling through the `EXTERNAL_FLUX` function in FDS.

The ignition patch receives a large heat flux, consisting of the prescribed external flux of 65 kW m^{-2} and the heat feedback of the flame. This heat flux is larger than

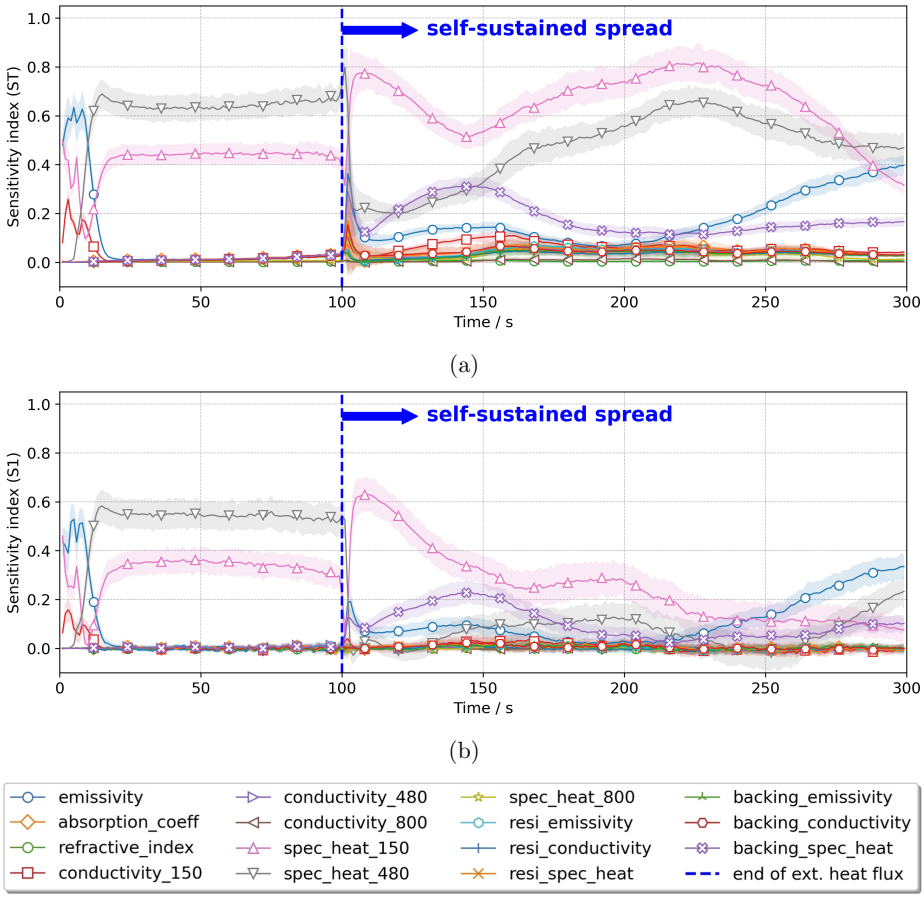

Figure 3.12: Time-series of the (a) ST and (b) S1 sensitivity indices, indicating respectively the total- and first-order effects on the HRRs of the flame spread simulation – zoom into the initial 300 s.

that during the steady-state self-sustained spread. Once the external flux is shut off, the initial flame shrinks rapidly. The flame takes some time to recover and grow to the size of the steady-state. This is reflected in the increased effect of the specific heat of PMMA at 150 °C between 100 s to 270 s. However, after approximately 270 seconds of simulation, their roles reverse, and the specific heat at 480 °C becomes more influential than that at 150 °C for the remaining simulation time. As more of the material heats up and its temperature increases, the specific heat at 480 °C prevails, as presented in Figure 3.13.

Figure 3.13 also shows that, despite oscillations, after the initial 300 s, the specific heat values along with emissivity, conductivity at 150 °C of PMMA, and the specific heat of the insulation material remain as the most influential parameters affecting the HRR. Another important observation concerns the least important parameters, whose effects on the HRR, although smaller, are not insignificant. The only exception is the refractive index, whose indices turned out to be zero in both simulation setups.

The fact that an input parameter has sensitivity indices equal to zero indicates that it has no influence on the model outputs. As this is the case for the refractive index, it can be concluded that this parameter has no impact on the simulation predictions. This behaviour had already been anticipated in Chapter 2, Section 2.2.2. The refractive index plays no role in the pyrolysis models in question and has most likely been included in the model developed by Hehnen and Arnold [2023] by mistake. Nevertheless, this observation demonstrates the ability of the sensitivity analysis method to capture sensitivities and reveal technical errors in the model [Saltelli et al., 2008].

In addition, it is important to mention that the low importance of the absorption coefficient might be reduced due to model-related details.

Figures 3.12 and 3.13 also show that the specific heat of the insulation material transitions from having no relevance during the ignition phase to becoming one of the most influential parameters affecting the spread. This discrepancy is potentially related to the amount of heat flux heating up the material in the two different stages. Throughout ignition, the sample receives substantial $65\,\mathrm{kW\,m^{-2}}$ plus the heat feedback from the flame. The rapid heating minimises the time period during which the insulation layer can impact the temperature distribution within the sample, which, in turn, impacts pyrolysis and the HRR. In contrast, during the spread phase, the total heat flux is considerably lower, and the overall system is less dominated by the intensity of the heat input. Therefore, changes in the specific heat of the insulation material, which directly affect its ability to store thermal energy, can have a comparatively larger impact on the temperature distribution of the sample.

The existence of a transition in parameter importance, defined by the end of the ignition phase and the start of a self-sustained spread, highlights the differences between the cone calorimeter and the flame spread heating conditions. That is because both in the ignition phase of the flame spread simulation, and in the cone calorimeter setup, the sample is subject to a considerably higher heat flux than that of the self-sustained spread. As previously discussed, the elevated heat flux tends to dominate the thermal behaviour of the system, effectively masking the effects of changes

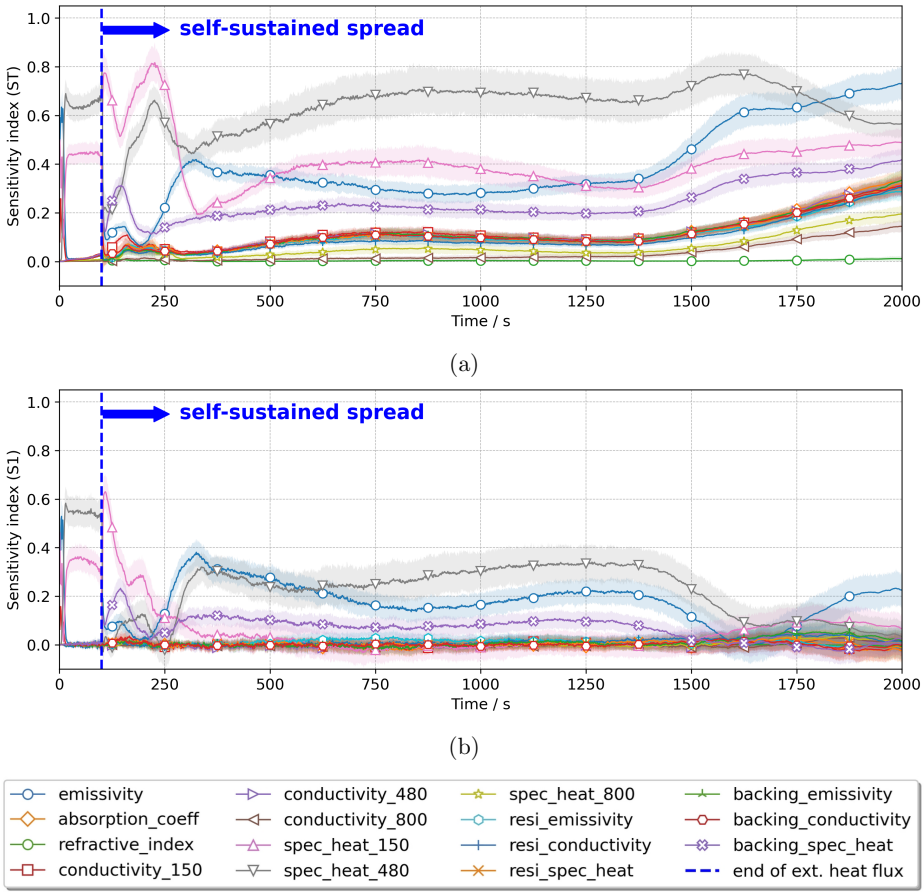

Figure 3.13: Time-series of the (a) ST and (b) S1 sensitivity indices, indicating respectively the total- and first-order effects on the HRRs of the flame spread simulation, up to 2000 s.

in parameters that are crucial to the spread, such as the specific heat of the insulation material. Consequently, given the cone calorimeter insensitivity to changes in this parameter, attempting its estimation through an optimisation based on the cone calorimeter would involve a high level of uncertainty. This implies that not all parameters that are important to the flame spread can be well estimated with optimisations based solely on the cone calorimeter setup.

3.3.2 Effects on the global RMSE and ROS

The effects of the 15 input parameters on the RMSE and on the ROS are presented respectively in Figures 3.14a and 3.14b. Since both are single-value outputs, sensitivities are described by a single set of indices for each case and not a time series. Confidence intervals are presented by error bars. For indices very close to one, such as the ST of specific heat at 480 °C in Figure 3.14a, confidence intervals can indicate that possible values for the associated sensitivity index exceed unity. In general, increased sample sizes ensure narrower confidence intervals and indices that fall within the expected range of 0 to 1. Nonetheless, the presented results were considered satisfactory for the objectives of this work. Moreover, some S1 indices present negative values, which are due to numerical artefacts in the estimates. This issue has been reported before as a common characteristic of Saltelli's method that is often associated with the value of the index being close to zero.

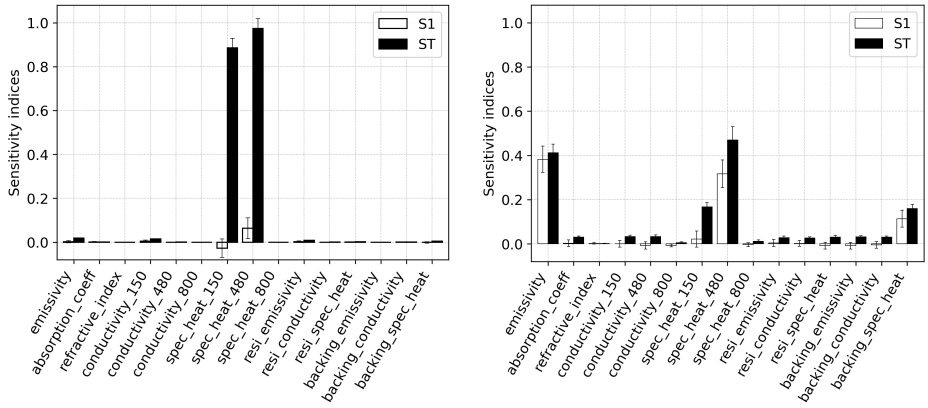

(a) (b)

Figure 3.14: Sobol sensitivity indices indicating the effects of the 15 input parameters on the single-value outputs of the two simulations setups. (a) Effects on the global RMSE - cone calorimeter simulation; (b) Effects on the ROS - horizontal flame spread simulation.

Dominant interaction effects on the RMSE

It can be seen from Figure 3.14a that the specific heat at 150 °C and at 480 °C are effectively the only two input parameters that significantly affect the RMSE, calculated as established in Equation 3.1. As discussed in the previous section, this

influence is characterised by strong interaction effects, due to the negligible S1 and dominant ST values. This means that the effect on the RMSE highly depends on how the values of these two parameters are combined.

Indeed, the combination between the specific heat at 150 °C and at 480 °C defines the slope of the linear curve that relates the two values in the piecewise linear function, see Figure 3.6b. The slope is in turn related to how fast the increase in the specific heat will occur as a function of temperature. For example, if the specific heat changes from a low value to a high value abruptly, suddenly more energy is required to cause the temperature of the material to change. In this case, this would reduce the local rates of pyrolysis, slowing down the production of combustible gases which then burn, releasing heat. Ultimately, this translates into flattened HRR curves. This change in the HRR shape determines how much each simulated curve deviates from the experimental HRR curve. This effect is then captured by the RMSE.

A complementary approach to visualise these strong interaction effects is presented in Figure 3.15. The plots show all 2^{17} (131,072) simulated HRR curves from the cone calorimeter, with colours representing their respective sample values of specific heat at 150 °C in Figure 3.15a, and specific heat at 480 °C in Figure 3.15b. The samples of these parameters are used to create the colour maps, which are then assigned to the HRR curves. This provides a visual representation of the specific heat values used in each simulation. The colour map illustrates how the shape of the HRR is influenced by combinations of values of these two parameters. For example, it becomes evident that flattened HRR curves, which also burn for longer times, result from a combination of low values of specific heat at 150 °C (dark blue in Figure 3.15a), and high values of specific heat at 480 °C (yellow in Figure 3.15b). The magenta curve is the HRR from cone calorimeter experiments, taken as reference for determining the RMSE.

Influence of emissivity

In comparison to what is observed for the RMSE, a different scenario of sensitivities is identified for the ROS, as depicted in Figure 3.14b. The ST and S1 indices show that PMMA emissivity and specific heat at 480 °C are, in order, the two most important parameters to affect the ROS amongst the ones investigated here, and no meaningful interaction effects are observed. Amongst the input parameters with lower importance, the specific heat of the insulation material and the specific heat of PMMA at 150 °C are the two most important ones.

Given that in FDS the flame is assumed to be optically thick, the role of emissivity in affecting the predicted HRR is related to the amount of radiative heat flux absorbed

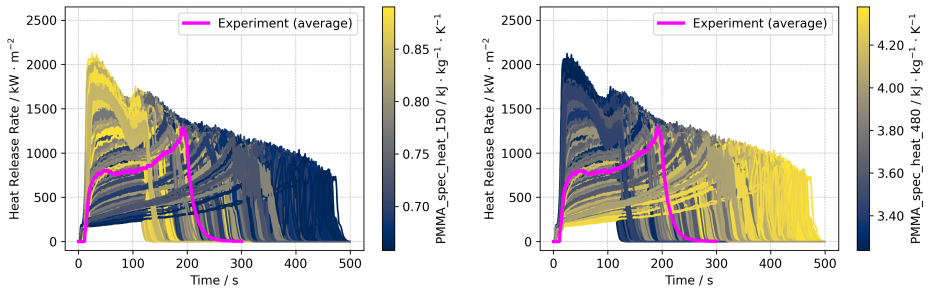

(a) (b)

Figure 3.15: Visualisation of the interaction effects between the time-dependent values of specific heat on the HRR curves of the cone calorimeter simulation. (a) Colour map: samples of specific heat at 150 °C; (b) Colour map: samples of specific heat at 480 °C.

by the material. It is therefore expected that the PMMA emissivity is more important during ignition, after which the residue emissivity should control the level of absorbed radiative heat flux once the first reactions have taken place at the surface. In the cone calorimeter simulation, however, the importance of the residue emissivity is lower than expected. One possible reason is the significantly higher importance of the specific heats in the cone calorimeter simulation (through interaction effects), which may be masking the influence of other parameters, such as the residue emissivity.

In the flame spread simulation, the PMMA emissivity is continuously important to the ROS, since the ROS is determined by how quickly the material ahead of the flame leading edge heats up to the ignition temperature. The low importance of the residue emissivity to the ROS may be related to the limited amount of residue formed at the moving leading edge, such that its associated parameters become comparatively uninfluential.

The optically thick assumption for horizontally spreading flames over PMMA samples of this size is supported by the heat flux measurements reported by Jiang et al. [2017]. In their work, for a PMMA sample of the same thickness and similar width (10 cm), radiation was the dominant mode of heat transfer from the flame to the solid. It should be noted however, that the lower part of a real flame, where the leading edge is located, the flame is usually weakly radiative and dominated by conduction in the gas phase, therefore being considered optically thin. For PMMA flames, this characteristic is perceived by a transparent faint blue colour at the flame base, see for example the work of Morrisset et al. [2024]. Since this effect is not

accounted for in the model, dependence on radiation might be overpredicted in the simulations, which would be reflected in an increased sensitivity of the ROS to changes in the material emissivity. Moreover, uncertainties related to the specified radiative fraction, which controls the amount of radiated heat from the flame, might contribute as well to an artificially enlarged sensitivity to emissivity.

Implications for transferability of parameter set

At this point, it is important to emphasise what is the main implication to the optimisation revealed by the sensitivity indices shown in Figure 3.14. The RMSE is a common approach to measure deviations between two sets of data, and therefore it is commonly used as cost function during the inverse modelling [Lauer et al., 2020]. This means that whatever influence an input parameter has on the model output (in this case, the HRR of the cone calorimeter), it should be reflected in the RMSE for an effective estimation.

However, comparison of Figures 3.10a and 3.14a suggests that the initial importance of PMMA emissivity and specific heat at 150 °C to the HRR observed in Figure 3.10a is not manifested to the same level in the RMSE. This implies that not only is it necessary that the direct model output is sufficiently sensitive to the inputs that are important to the flame spread, but also that the cost function is. In this regard, neither of these two requirements were met, since there are several other input parameters affecting the flame spread (reflected both in the HRR and ROS) that have little or no importance to the HRR in the cone calorimeter and/ or to the RMSE.

3.3.3 Effects on partial RMSEs

Motivated by the results shown in Figure 3.10, where differences exist in parameter importance between the initial 20 s and the rest of the simulation, additional sensitivity analyses were conducted. This time, partial RMSEs were computed, taking two different stages of the HRR time history as reference. In the first stage, a partial RMSE is calculated up to 20 s of simulation time (RMSE_0-20) and deviations to the experimental data are calculated accordingly up to the 20th second. Similarly, in the second stage, the RMSE is calculated from 21 s to 300 s (RMSE_20-300). Sensitivity indices are presented for these two approaches in Figures 3.16a and 3.16b, respectively.

As expected, the results for each partial RMSE show a clear correspondence with the different sensitivity profiles presented in Figure 3.10. That is, the ranking of pa-

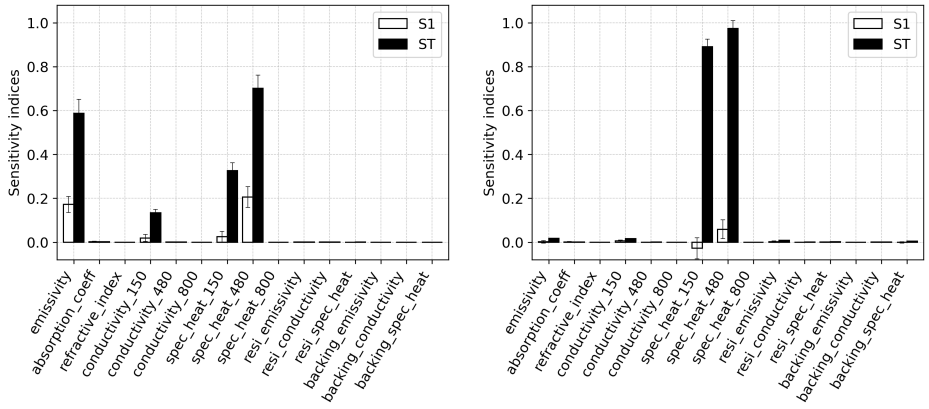

(a) (b)

Figure 3.16: Sobol sensitivity indices indicating the effect of input parameters on the RMSE calculated over different stages of the cone calorimeter simulation. (a) Effects on the RMSE over 0 - 20 seconds; (b) Effects on the RMSE over 20 - 300 seconds.

rameter importance for the first 20 s of the HRR time series aligns with the results shown in Figure 3.16a for the RMSE_0-20, where only the emissivity, thermal conductivity at 150 °C, and specific heat at 150 °C and 480 °C are influential. A similar trend is observed for the second stage of the simulation. The growing influence of the specific heat values beyond the 20-second mark is reflected in the RMSE_20-300 results shown in Figure 3.16b.

This analysis helps understand why the global RMSE seems not to be significantly influenced by any other parameter than the specific heat at 150 °C and at 480 °C. Since the importance of these two values is higher for the most part of the simulation, the brief influence of emissivity and conductivity at 150 °C in the early stages gets diluted when the whole HRR time-series is condensed in a single RMSE value.

These observations highlight the importance of making use of cost functions that are as sensitive to the input parameters as the model outputs. as the model outputs that they intend to represent. This way, a new design of cost functions can be defined. Instead of optimising for the global RMSE, which may be dominated by only a subset of sensitive parameters, a combination of RMSE at different phases of the experiment may cover the full set of sensitive parameters. In the case of the cone calorimeter investigated here, this would involve considering partial RMSEs calculated up to the initial 20 seconds and another one calculated from 21 to 300 seconds of the experiment, such that the estimations of emissivity and conductivity at 150 °C are improved. Still,

this strategy would not be sufficient to estimate well all parameters that are important to the flame spread, such as the specific heat of the insulation material, as the cone calorimeter is insensitive to it.

Alternatively, optimisation targets measured from bench-scale flame spread experiments could be employed rather than those from the cone calorimeter. Specifically, the ROS could be measured and incorporated as target in the optimisation, enabling a comparison with the simulated ROS calculated for example as introduced in Section 3.2.2. Yet, this strategy may be computationally expensive and further research on this idea is needed, particularly because it does not exist to date a typical bench-scale flame spread experiment as the cone calorimeter that provides standardised guidelines for measuring the HRR and the MLR along with the ROS.

A good starting point towards such an experiment could be the standard reaction-to-fire test methods described in ISO 5658-2, ISO 9239-1, and ISO 12468-1. These could potentially be adapted to allow measurements of the required quantities while maintaining a scale comparable to that of cone calorimeter. Another promising alternative is the small-scale flame spread experiments investigated in the work of Morrisset et al. [2023, 2024], which enable the determination of solid-phase temperature profiles in addition to the ROS. Their work and methods will be discussed in more detail in Chapter 5.

3.3.4 Scatterplots

Figure 3.17 shows the global RMSE values plotted against the samples of its two most influential parameters: the specific heat at 150 °C and at 480 °C. The result is a 3-D plot, where a well-defined surface allows the graphical interpretation of the interaction effects between the two inputs on the RMSE.

The 3-D surface reveals a dark-blue valley for which the RMSE values are minimised when certain combinations of the two parameters are taken. A 2-D projection over the axes of input parameters shown in Figure 3.17b clarifies that such combinations belong to a linear shaped subset of samples in their parameter space. Another interesting region in the 3-D surface is the plateau formed by nearly constant values of RMSE. The existence of a plateau reveals a significant portion of the input space that leads to no meaningful change in the RMSE. This is particularly important for the optimisation, because it can decrease its efficiency and lead to convergence to local minima.

A very similar relation to the one shown in Figure 3.17, is presented in the work of Batiot et al. [2016], where the effects of two interacting parameters on the quadratic

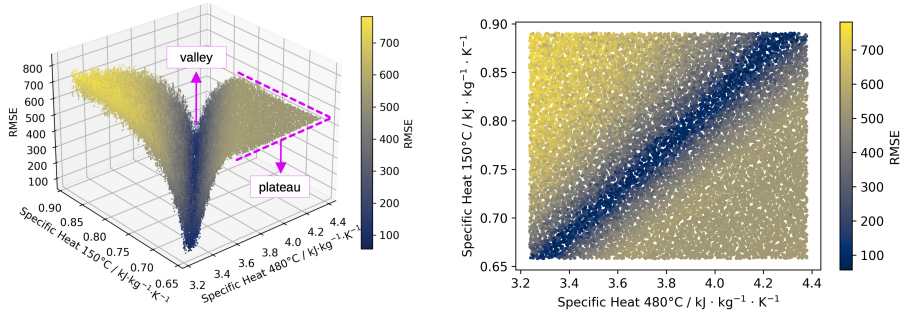

(a) (b)

Figure 3.17: Values of RMSE plotted against its two most influential parameters. (a) 3-D surface; (b) 2-D projection.

error is discussed also in the context of their consequences to the optimisation. In their work, the two interacting parameters are the pre-exponential factor A and the activation energy E of the Arrhenius equation, and the quadratic error is calculated over the material MLR. Batiot et al. [2016] used the Sobol indices to discuss the well-known compensation effect between A and E in terms of the interaction effects captured by the second-order index. Given the similarity between the applied methodologies and the produced outcomes, it could be said also here that the linear relation between values of specific heat at 150 °C and at 480 °C translate into compensation effects and trade-offs during the optimisation.

3.4 Conclusions

The sensitivity analyses presented in this chapter provided useful information on the differences in parameter importance between the cone calorimeter and flame spread simulations in FDS. These differences have direct implications for inverse modelling strategies based on the cone calorimeter, which are used to generate material properties for pyrolysis modelling in predictive flame spread simulations. The most relevant remarks are:

- The Sobol indices indicated that the cone calorimeter simulation is not sufficiently sensitive to all parameters that influence flame spread. As a result, parameters that are unimportant in the cone calorimeter setup will be estimated with greater uncertainty, which is then propagated to the flame spread simulation.

- Some parameters briefly affect the cone calorimeter simulation but lose their influence when the HRR evolution is summarised into a single-value output, such as the global RMSE. Only the specific heat values at 150 °C and 480 °C have a noticeable impact on RMSE, mainly through interaction effects, while the influence of the remaining parameters is negligible.

Chapter 4

The influence of small mass loss rate peaks on flame spread predictions

The contents of this chapter are based on the article entitled *The influence of small mass loss rate peaks on the rate of spread of predictive flame spread simulations: A theoretical study* [Quaresma et al., 2025].

4.1 Introduction

Commonly used engineering approaches for determining pyrolysis rates are based on MLRs derived from TGA measurements. Peaks in the MLR curve – often, derivative thermogravimetric (DTG) curve – are interpreted as pyrolysis reactions, with the associated rates typically modelled using the Arrhenius equation (see Equation 2.5). For each identified peak, kinetic parameters, the pre-exponential factor (A) and activation energy (E), must be estimated. Various estimation methods exist, including analytical approaches (e.g., conventional, direct differential) and curve-fitting optimisation techniques [Vyazovkin et al., 2011; Hurley et al., 2015].

The study presented in this chapter falls within the latter approach, where pyrolysis models are coupled with optimisation algorithms to determine A and E by inverse modelling. In this process, the first step requires analysing the topology of the MLR curve, where commonly several fluctuations exist. However, pyrolysis models rarely capture the full complexity of MLR measurements, and often such small fluctuations in the data are neglected. This happens for at least two reasons:

(i) the number of modelled reactions is limited for practical purposes, despite experimental data often suggesting the presence of additional reactions;

(ii) experimental data can be inconsistent, showing variability in individual measurements or discrepancies across different apparatuses [De Lannoye et al., 2024].

The MLR data can exhibit significant variability due to several factors. Specifically for PMMA, these include the polymerisation method used (e.g. free radical initiation, anionic initiation [Zeng et al., 2002; Holland and Hay, 2002]), the manufacturing process (e.g. extruded, cast [Fiola et al., 2021]), the molecular weight [Ferriol et al., 2003], samples provided by different vendors, experimental conditions, material colour, sample preparation [DiDomizio and McKinnon, 2023], and device calibration [De Lannoye et al., 2024]. Moreover, the application of smoothing techniques to reduce noise in MLR data can result in loss of information and potentially lead to inaccurate representation of the real MLR behaviour [Morrisset et al., 2022].

Previous TGA studies on PMMA thermal degradation under nitrogen atmosphere and varying heating rates have attributed small, low-temperature peaks to the volatilisation of impurities, such as residual monomer or additives [Holland and Hay, 2002; Hirata et al., 1985]. However, other research attributes these peaks to the onset of depolymerisation, triggered by the breaking of weak linkages at the polymer chain ends – a behaviour particularly common in radically polymerised PMMA [Ferriol et al., 2003; Manring, 1989; Manring et al., 1989; Kashiwagi et al., 1986]. It is important to note, however, that in practical applications, especially in fire modelling, pyrolysis models are primarily developed to estimate the rates at which combustible gases are released into the gas phase for combustion, rather than to replicate the precise chemical mechanisms occurring during pyrolysis.

Specifically for PMMA, different reaction schemes have been proposed for modelling pyrolysis based on the MLR curve profile. These differences involve not only the number of identified MLR peaks but also the serial or parallel nature of the defined pyrolysis reactions. In some studies, PMMA pyrolysis is very simplified, being described by a single reaction representing the main MLR peak [Bolshova et al., 2023; Vermesi et al., 2016]. Other approaches account for two reactions, which can be either in series [Fiola et al., 2021] or in parallel [Lauer et al., 2021, 2023].

In these models, the first reaction represents a smaller MLR peak observed at lower temperatures, while the second represents the main peak at higher temperatures. Yet, comparison against the utilised MLR data shows that in these cases, only the most significant peaks were modelled, while small peaks were neglected. Exceptions to this trend are, for example, the works of Ferriol et al. [2003] and Hehnen and Arnold

[2023], where a general framework of multiple parallel reactions was proposed as a strategy to improve the fitness to the target MLR data.

In this context, the following question naturally arises: Do small MLR fluctuations matter, particularly when the pyrolysis model is used to predict flame spread? The current assumption is that they do not, as small fluctuations are often ignored, leading to slight deviations between pyrolysis schemes and experimental MLR data. However, the extent to which such deviations affect key model predictions remains unknown. This chapter challenges that assumption by introducing a small MLR fluctuation into an established pyrolysis model and evaluating its effect on the predicted ROS.

The scenario considers a horizontal flame spread simulation over a PMMA sample, where pyrolysis is described by the UMD Pyrolysis Model [Fiola et al., 2021]. This formulation was particularly chosen because it is currently recommended by the MaCFP working group for modelling PMMA pyrolysis [Leventon et al., 2023]. In this original form, the model accounts for two decomposition reactions. In this study, an additional reaction is introduced to represent a small MLR fluctuation, and its impact on the predicted ROS is assessed using two different sensitivity analysis methods. Details of the methodology are provided in the next section.

4.2 Methods

4.2.1 PMMA pyrolysis model

In this study, the selected PMMA pyrolysis model was developed in previous work of Fiola et al. [2021] based on TGA data of cast black PMMA. The model provides a complete set of kinetic parameters and material properties which are currently recommended by the MaCFP working group for modelling PMMA pyrolysis [Leventon et al., 2023]. It is referred to in that context as the UMD Pyrolysis Model, but for brevity, it will simply be called the UMD Model here.

MaCFP's recommendation is based on validation exercises conducted in 2023 that defined the best performing parameter set as the one which closest predicted MLR measurements produced with the NIST Gasification Apparatus. The parameter set has been employed before to simulate real-scale flame spread experiments, as the Single Burning Item (SBI) setup [Chaudhari et al., 2021], and the Parallel Panels Test during the 2023 MaCFP workshop (MaCFP-3) and is part of the FDS validation suite [NIST, 2023b].

Figure 4.1 presents the UMD Model alongside the experimental normalised residual mass (Figure 4.1a) and the MLR curve (Figure 4.1b). The experiments were

conducted using a heating rate of $10\,\mathrm{K\,min^{-1}}$ and nitrogen atmosphere, resulting in MLR profiles where small peaks at low temperatures and a large peak at high temperatures can be observed.

The experimental curves were obtained by averaging TGA data reported by several different institutes to the MaCFP database (namely NIST, TIFP, UMD, and UQ). Here, experimental MLR data from various contributions are intentionally presented to emphasise the variability in the data, which is represented by the shaded areas around the solid gray curves in Figure 4.1. The kinetics of PMMA pyrolysis in this model are represented by two serial first-order reactions, capturing two main peaks observed in Figure 4.1b.

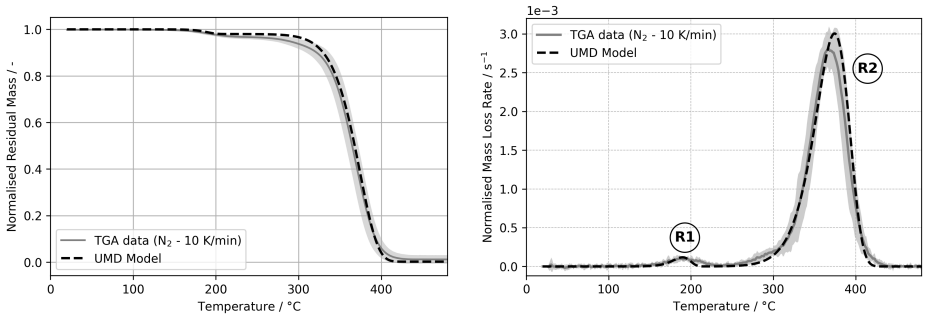

(a) (b)

Figure 4.1: Comparison of the original UMD model with TGA data from the MaCFP Database [Fiola et al., 2021; Leventon et al., 2023]. The experimental data represents the average of multiple datasets provided by NIST, TIFP, UMD, and UQ. (a) Normalised residual mass; (b) mass loss rate.

The first reaction (here named R1) was introduced to represent a small MLR peak observed at approximately 190 °C in Figure 4.1b. It was described considering that the melted polymer ($\mathrm{PMMA_{melt}}$) produces 2 % of a combustible gas ($\mathrm{PMMA_{gas}}$), and 98 % of an intermediate component ($\mathrm{PMMA_{int}}$). It was then assumed that the production of $\mathrm{PMMA_{int}}$ triggers a secondary pyrolysis reaction (here, R2), which in turn produces 0.2 % of char and 99.8 % of the same combustible gas as in reaction R1, $\mathrm{PMMA_{gas}}$.

The kinetic parameters for each reaction were determined by inverse modelling, using the TGA data produced by UMD as target. Data of DSC measurements were used to determine the heats of reaction of R1 and R2, as well as the material specific heat capacity, as described elsewhere [Fiola et al., 2021; Li and Stoliarov, 2013]. The

reactions R1 and R2 are shown in Table 4.1, and their respective kinetic parameters and heats of reaction are presented in Table 4.2.

Table 4.1: Scheme of reactions representing PMMA pyrolysis.

Label	Pyrolysis reactions	Source
R1	$PMMA_{melt} \longrightarrow 0.98\ PMMA_{int} + 0.02\ PMMA_{gas}$	UMD Model, by
R2	$PMMA_{int} \longrightarrow 0.002\ PMMA_{char} + 0.998\ PMMA_{gas}$	[Fiola et al., 2021]
R3	$PMMA_{imp} \longrightarrow 0.002\ PMMA_{char} + 0.998\ PMMA_{gas}$	This work

Table 4.2: Kinetic parameters of PMMA pyrolysis reactions.

Label	A / s^{-1}	E / $J\,mol^{-1}$	Peak temperature (T_p) / °C	Pyrolysis range (ΔT) / °C	Heat of reac. / $kJ\,kg^{-1}$
R1	4.95e+16	1.64e+05	189.95	59.0	5.0
R2	1.35e+11	1.64e+05	374.3	115.3	817.0
R3	2.06e+12	1.32e+05	210.0	80.0	5.0

The pyrolysis scheme in the UMD Model, defined by reactions R1 and R2, captures the main MLR peaks observed in the variability of the experimental data, as shown in Figure 4.1. However, they are insufficient to account for smaller additional MLR peaks or fluctuations observable throughout the temperature range where PMMA pyrolyses. As a consequence, the total MLR obtained with the two-reaction UMD Model deviates from the MLR derived from TGA experiments. Some of these deviations can be observed, for example, in the 210 °C to 310 °C range, and above 400 °C, as indicated by the red arrows in Figure 4.2.

Additionally, a significant deviation from the experimental data is observed at the main peak associated with reaction R2. The model displays a higher MLR peak than the average experimental data, with a slight shift toward higher temperatures. Assuming that all pyrolysis reactions of PMMA are of first-order, such deviations in the total MLR can only be reduced if more pyrolysis reactions are included in the model.

On this basis, a third parallel reaction (R3) is introduced to represent a small peak that is not accounted for by the UMD Model. R3 is defined to yield 0.2 % of char and 99.8 % of $PMMA_{gas}$, similar to reaction R2, as shown in Table 4.1. Considering the regions indicated by the red arrows in Figure 4.2, there are several possible combinations of peak temperature, pyrolysis range, and mass fractions that can characterise

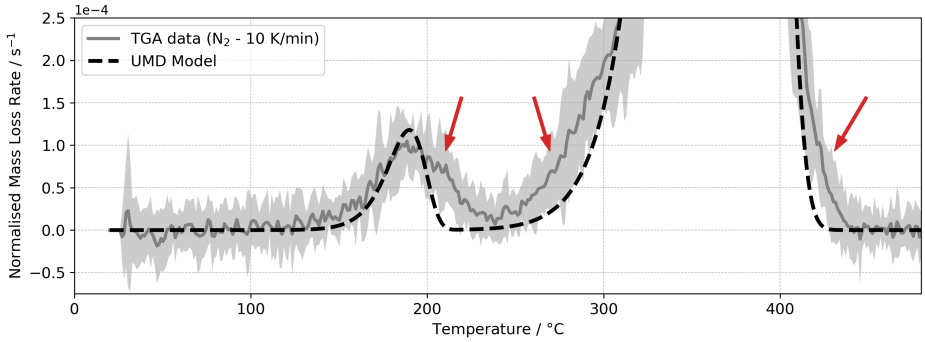

Figure 4.2: Zoomed-in view of the mass loss rate curve, emphasising the deviations between the original UMD Model and the experimental average data (indicated by the red arrows).

a small peak to improve agreement with the experimental data. Understanding how this variability in the R3 peak affects the ROS is the main objective of this study, and will be addressed in detail later in the text.

4.2.2 Flame spread simulation

The simulation setup was designed to enable a steady-state, self-sustained flame spread on a horizontal PMMA plate of bench-scale dimensions. The FDS version FDS6.7.9-0-gec52dee-HEAD, was used as the modelling framework. An overview of the most refined case is presented in Figure 4.3 for illustration purposes.

Similarly to the methodology presented in Chapter 3, Section 3.2.2, the numerical model was developed to serve as a simplified sandbox case to apply state-of-the-art approaches for predicting flame spread within FDS. Key aspects of the solid-phase definition, including sample dimensions, material properties, and pyrolysis kinetics, were tailored to replicate the characteristics of black cast PMMA, consistent with the material used in the MaCFP studies.

The sample thickness is set to 6 mm. Width and length of the sample were assigned to have approximately 100 mm and 200 mm, respectively. The values of width and length were slightly adjusted to conform with the tested gas phase cell sizes. An external heat flux of 65 kW m^{-2} is applied to one of the sample ends for 100 s to start ignition. The dark grey patch in Figures 4.3a and 4.3b extends for 30 mm in the x-direction, indicating the region where the sample is ignited.

The zones of spread depicted in Figure 4.3a, as well as the methodology used to determine the ROS, have been previously described in Chapter 3, Section 3.2.2.1.

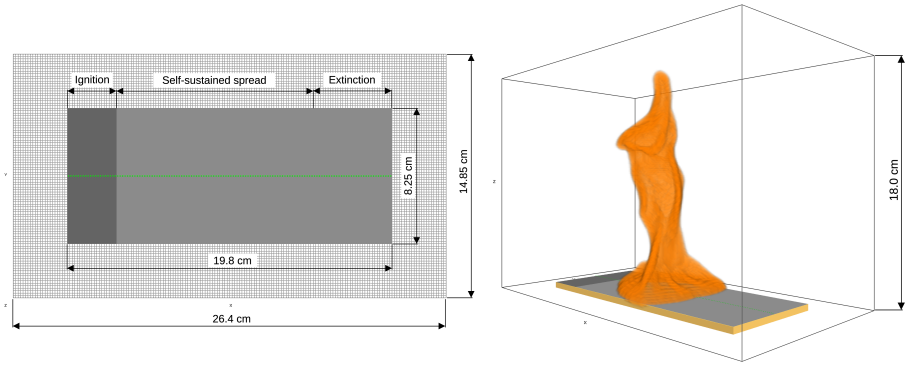

(a) (b)

Figure 4.3: Simulation setup of a self-sustained flame spread over a horizontal PMMA sample. The most refined case is shown, consisting of 1.5 mm gas-phase cells. (a) Top view of computational domain showing the zones of spread; (b) perspective view showing a self-sustained spreading flame.

The rear side of the sample is insulated with a board of Marinite 20 mm thick, whose width and length correspond to those of the sample. No wind or forced ventilation conditions were considered. Further details on the modelling of the solid and gas phases, as well as details on grid analyses and other simulation settings are provided in the following subsections.

4.2.2.1 Solid phase

The rates at which the solid material looses mass due to pyrolysis were defined to vary exponentially with the local temperatures of the solid, as established by the Arrhenius equation (see Equation 2.5). In general, four input parameters are required to define a rate of reaction: the pre-exponential factor A, the activation energy E, the mass fraction of the solid, and the order of reaction.

Alternatively, in FDS, pyrolysis rates can be defined in terms of the parameters `PYROLYSIS_RANGE` (ΔT), `REFERENCE_TEMPERATURE` (T_p), and `HEATING_RATE` ($\dot{T}$), instead of A and E. The parameter ΔT refers to the width of the peak, assuming its shape to be approximately triangular, whereas T_p is simply the peak temperature. From ΔT and T_p, FDS calculates A and E using the following relations:

$$r_p = \frac{2\dot{T}}{\Delta T} Y_\mathrm{s}(0)\,(1-\nu_\mathrm{s}) \tag{4.1}$$

$$E = \frac{\mathrm{e} r_p}{Y_s(0)} \frac{R T_p^2}{\dot{T}} \tag{4.2}$$

$$A = \frac{\mathrm{e} r_p}{Y_s(0)} \exp\left(\frac{E}{RT_p}\right) \tag{4.3}$$

where r_p is the peak reaction rate, $\dot{T}$ is the heating rate used in the TGA experiment, $Y_s(0)$ is the initial mass fraction of the solid, and ν_s is the yield of the solid residue [McGrattan et al., 2005].

In the investigations carried out in this chapter, the pyrolysis reactions will be described and discussed in terms of ΔT and T_p, as performed in previous inverse modelling studies by Hehnen and Arnold [2023], and Lauer et al. [2023]. This approach allows for a direct representation of the MLR peaks within the pyrolysis temperature ranges of interest, making sampling more efficient and representative of the behaviour of real materials.

The default 1-D conduction model available in FDS was selected, as described in Section 2.1.1. Spatial discretisation of the PMMA layer was set to uniform, whereas the default stretched node spacing for the layer of the insulation material was adopted. The parameter controlling the solid phase discretisation `CELL_SIZE_FACTOR` was set to 1.0, as it was found that values lower than unity (0.1, 0.5), which lead to increased resolution, had negligible effects on the ROS, while significantly increasing the computational cost.

The thermophysical and optical parameters describing the PMMA sample in the UMD Model follow the specifications proposed by Fiola et al. [2021]. Both $\mathrm{PMMA_{melt}}$ and the residue $\mathrm{PMMA_{char}}$ were described by the same set of properties. For consistency, here $\mathrm{PMMA_{imp}}$ is also described using these properties. The parameter set includes sample emissivity, absorption coefficient, density, thermal conductivity and specific heat capacity. The thermal conductivity and the specific heat capacity are given as temperature-dependent parameters, determined by piecewise linear functions. The values for sample emissivity, absorption coefficient, and density are 0.96, $2870\,\mathrm{m^{-1}}$, and $1210\,\mathrm{kg\,m^{-3}}$, respectively. For associated uncertainties and details on the estimation procedure to obtain these parameters, the reader should refer to the original work of Fiola et al. [2021].

The material definition used for the insulation board was taken from the Parallel Panel simulation setup by NIST, which is publicly available in the FDS validation repository [NIST, 2023a]. The properties correspond to those of Marinite, a common insulating material in fire experiments. The density and emissivity of Marinite were set to $737\,\mathrm{kg\,m^{-3}}$ and 0.90, respectively. The thermal conductivity and specific heat capacity were assumed to be constant at $0.12\,\mathrm{W\,m^{-1}\,K^{-1}}$ and $1.20\,\mathrm{kJ\,kg^{-1}\,K^{-1}}$, respectively.

4.2.2.2 Gas phase

The combustible gas $PMMA_{gas}$ produced by the defined pyrolysis reactions was described with the properties of the monomer methyl methacrylate (MMA). The combustion of MMA was assumed to be mixing-controlled, and the LES simulation mode in FDS was selected. All default settings that accompany LES were applied, which are summarised in Section 2.1.2 and can be found in detail in McGrattan et al. [2013]. The default radiation model based on the grey gas assumption was used, and a specified radiative fraction determines the portion of the total heat released as thermal radiation.

The thermophysical properties of MMA and the yields of its combustion products follows the description used in the Parallel Panel validation cases by NIST [NIST, 2023b]. The specific heat capacity of MMA was fixed at $1.10\,\mathrm{kJ\,kg^{-1}\,K^{-1}}$, and its thermal conductivity and diffusivity were calculated by FDS from the prescribed Lennard-Jones parameters $\sigma = 4.701\,\text{Å}$, and $\varepsilon/k = 205.78\,\mathrm{K}$. The yields of soot and CO were assigned respectively to $0.022\,\mathrm{g\,g^{-1}}$ and $0.01\,\mathrm{g\,g^{-1}}$. Based on the chemical formula of MMA ($C_5H_8O_2$), and the specified yields of soot and CO, the heat of combustion is given as $24265.3\,\mathrm{kJ\,kg^{-1}}$. The radiative fraction of the MMA gas is set to 0.31.

A grid sensitivity study was carried out with different gas phase cell sizes: 3.0 mm, 2.5 mm, 2.0 mm, and 1.5 mm. It was observed that a stable self-sustained spread did not occur for cell sizes larger than 2.0 mm, as the flame extinguished soon after the end of ignition. In the 2.5 mm case, although propagation towards the end of the sample was observed, the flame assumed an asymmetrical and unstable shape along the way.

For each of the 1.5 mm, 2.0 mm, and 2.5 mm cases, the impact on the ROS due to the number of radiation angles (NRA) was evaluated. Three values of NRA (104 , 1208 , 3016) were tested, and it was found that the effect of the NRA was insignificant across all gas phase resolutions. In light of this, this study will focus on the 1.5 mm and 2.0 mm cases only, each considering default settings of NRA (= 104).

The size of the computational domain was determined such to encompass the entire height of the flame in the positive z-direction, and to reduce possible effects of domain boundaries. In the 1.5 mm case, the sample is 82.5 mm wide and 198 mm long; and the domain extends for $264\,\mathrm{mm} \times 148.5\,\mathrm{mm} \times 180\,\mathrm{mm}$ in the x-, y- and z-directions. In the 2.0 mm case, the sample is 102 mm wide and 192 mm long; and the domain extends for $256\,\mathrm{mm} \times 170\,\mathrm{mm} \times 150\,\mathrm{mm}$ in the x-, y- and z-directions. The simulation domains were subdivided into multiple meshes to enable parallel computation. The

most refined case, with 1.5 mm cells, was divided into 162 meshes, while the 2.0 mm cells were divided into 80 meshes.

4.2.3 Analysis of small MLR peaks

In order to evaluate the effect of small MLR fluctuations on the flame spread predictions, a small MLR peak is added to the original UMD Model. The small MLR peak is defined as a pyrolysis reaction consuming from 0.5 % to 2 % of the initial mass of the sample, represented as reaction R3 in Table 4.1.

The mass fraction decomposed by R3, named PMMA_{imp}, represents a portion of the virgin PMMA sample that may contribute to small MLR fluctuations. While PMMA_{imp} does not represent a specific chemical component, it serves as a placeholder for minor impurities or alternative degradation pathways not captured by the reactions in the original model (R1 and R2 in Tables 4.1 and 4.2).

The effect of the introduced R3 peak will be described and analysed through the following three parameters:

- the peak temperature (T_p);
- the pyrolysis range (ΔT), i.e. peak width;
- the initial mass fraction (m_0) of PMMA_{imp} decomposed by R3.

All pyrolysis reactions of PMMA are assumed first-order, i.e. $n = 1$ in Equations 2.4 and 2.7, and the influence of reaction order is not included in the analysis. Furthermore, as the focus lies on the kinetic parameters defining R3, the importance of the heat of reaction of R3 is also not evaluated in this study, and its value is fixed at $5.0\,\text{kJ} \cdot \text{kg}^{-1}$ as presented in Table 4.2.

In Figure 4.2, red arrows highlight three positions in the temperature range of pyrolysis, where introducing a small peak could enhance the model's alignment with the experimental data. For instance, a small peak with a pyrolysis range of $\Delta T = 80\,^{\circ}\text{C}$, decomposing 1 % of the initial mass of the material, can be placed at 210 °C, 284 °C or 420 °C, as shown in Figure 4.4a.

The total resulting MLRs, presented in Figure 4.4b, which combine the UMD Model with the R3 peak at each location, show better agreement with the experimental data than the original UMD Model alone. This improvement in fit is reflected in Figure 4.5, where the RMSE quantifies the enhanced match between each modified model and the experimental TGA data. However, multiple combinations of peak temperature, peak width, and mass fraction could define a small peak like R3 that

enhances the fit of the model within these regions, allowing for further exploration of optimal parameters.

In this sense, another aspect of this study is to systematically examine the relationship between the simulation model and the introduced small peak, extending beyond the three main regions highlighted by the red arrows in Figure 4.2. By varying the position of the small peak across the full temperature range associated with PMMA pyrolysis, the model's sensitivity to this peak is evaluated in a broader context. This is motivated by generalised approaches [Ferriol et al., 2003; Hehnen and Arnold, 2023], where adding a third peak (R3) can be used to improve the overall fit to the experimental data, not only in regions where distinct peaks are observed but also in areas where it might overlap with existing peaks in the model.

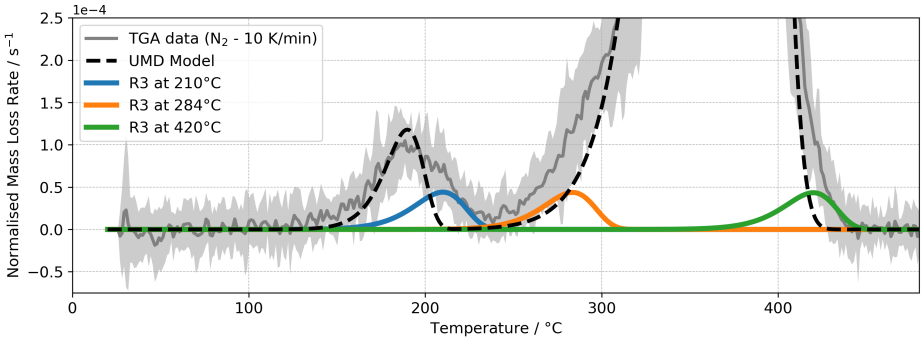

(a)

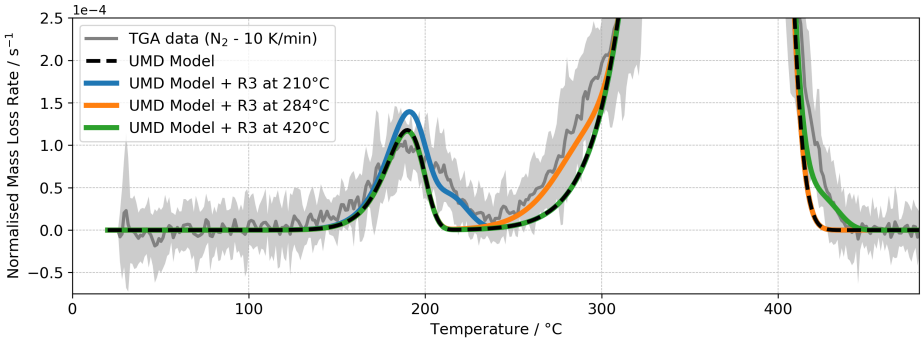

(b)

Figure 4.4: Zoomed-in view of the normalised MLR curves. Figure (a) shows possible locations for the small R3 peak, which can improve agreement with the experimental TGA data. Figure (b) displays the total MLR resulting from the UMD Model in presence of the R3 peak at each of these locations.

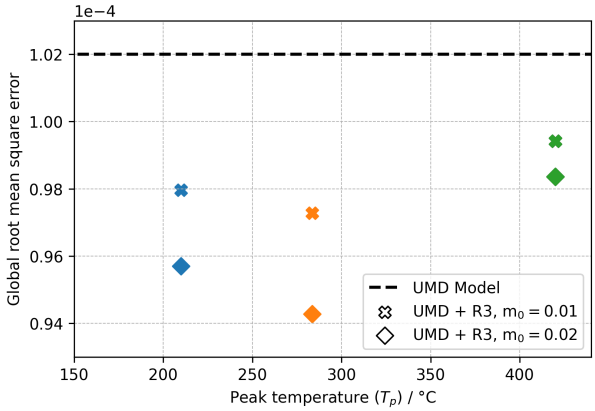

Figure 4.5: RMSE calculated between the original and the modified UMD Models, in which the R3 peak is incorporated, for mass fractions of $m_0 = 0.01$ and $m_0 = 0.02$, at 210 °C, 284 °C, and 420 °C. The inclusion of the R3 peak at these temperatures in the original model generally reduces the RMSE, indicating improved agreement with experimental data.

Two different methods were used to evaluate the effect of small MLR peaks on the ROS. In the first method, the parameters T_p, ΔT and m_0 were varied one-at-a-time to assess their individual impacts on the ROS, with results discussed relative to different simulation references. While this approach can highlight individual parameter effects, it does not fully capture how each parameter contributes to the overall variability of the ROS across its entire range of values. This is because it only measures responses to isolated changes rather than the cumulative impact of each parameter as it varies throughout the entire parameter space. This means that it may overlook how sensitive the ROS is to the full scope of possible variations in each parameter, providing only a partial assessment of their relative importance. To address this limitation, the second method combines an uncertainty analysis with a global sensitivity analysis, both performed using a polynomial chaos expansion (PCE) approach. These methods offer a more comprehensive view and are described in detail in the following sections.

4.2.3.1 One-at-a-time analysis

In this approach, the goal is to investigate the individual impacts of the parameters defining the small R3 peak (T_p, ΔT, m_0) on the ROS. Four groups of simulations were created, considering two mass fractions of PMMA_{imp}: $m_0 = 0.01$ and $m_0 = 0.02$; and two gas phase resolutions of 1.5 and 2.0 mm cells.

The groups were labelled with two characters for easier reference: the first character denotes the $PMMA_{imp}$ mass fraction, and the second character denotes the cell size. A mass fraction of 0.01 is represented by "1", and 0.02 is represented by "2". Similarly, a cell size of 1.5 mm is represented by "a", and 2.0 mm is represented by "b". For example, "Group 2a" is composed by simulations where the mass fraction of $PMMA_{imp}$ is fixed at 0.02 , and the gas phase cell size is 1.5 mm. Additionally, two simulation cases corresponding to the same cell sizes, where only the original UMD Model is used, were named Cases 0a and 0b. Table 4.3 presents a summary of the simulation groups and cases considered in the analysis.

Table 4.3: PMMA composition and gas cell sizes considered in each simulation group.

Label	PMMA composition	Cell size (gas phase)
Case 0a	100 % $PMMA_{melt}$	1.5 mm
Case 0b	100 % $PMMA_{melt}$	2.0 mm
Group 1a	99 % $PMMA_{melt}$ + 1 % $PMMA_{imp}$	1.5 mm
Group 1b	99 % $PMMA_{melt}$ + 1 % $PMMA_{imp}$	2.0 mm
Group 2a	98 % $PMMA_{melt}$ + 2 % $PMMA_{imp}$	1.5 mm
Group 2b	98 % $PMMA_{melt}$ + 2 % $PMMA_{imp}$	2.0 mm

For each group of simulations detailed in Table 4.3, the peak temperature T_p was varied one-at-a-time, while maintaining ΔT at constant 80 °C. Then, T_p was held fixed at 210 °C and ΔT was varied independently, but only in the coarser simulation cases, i.e. Groups 1b and 2b. This limitation aimed to save computing time, considering the expected lower impact of ΔT in comparison to T_p. The variation intervals for these parameters were established based on their initial values: $T_p = 210\,°C$ and $\Delta T = 80\,°C$ for the R3 peak, as well as on the observed variability in the total MLR from TGA data (see Figure 4.2 and Table 4.2).

Table 4.4: Reaction scheme and varied parameters of R3 in each simulation group.

Label	Reaction scheme	Varying parameters (R3)
Case 0a	R1 + R2	-
Case 0b	R1 + R2	-
Group 1a	R1 + R2 + R3	Peak temperature (T_p)
Group 1b	R1 + R2 + R3	Peak temperature (T_p), Pyrolysis range (ΔT)
Group 2a	R1 + R2 + R3	Peak temperature (T_p)
Group 2b	R1 + R2 + R3	Peak temperature (T_p), Pyrolysis range (ΔT)

Starting from an initial peak temperature of $T_p = 210\,°C$, the variation interval for T_p was defined to range from 80 % to 200 % of 210 °C, resulting in a range of 168 °C to 420 °C. From the lower limit of this interval, temperature points for T_p were sampled at increments of 10.5 °C (5 % of 210 °C). This strategy produced 25 samples, each of which was used in a different flame spread simulation, with all other simulation settings kept fixed and unchanged within a group. The 25 different positions of peak R3 associated with the T_p samples are illustrated in Figure 4.6. Overall, 100 simulations were conducted to study the effect of T_p across the four simulation groups.

Similarly, the variation interval for ΔT was defined to range from 80 % to 200 % of 80 °C, resulting in a range of 64 °C to 160 °C. From this interval, 25 samples were generated at increments of 4 °C, which corresponds to 5 % of 80 °C. The R3 peaks resulting from the ΔT samples are presented in Figure 4.7, where the effect on the width of R3 can be clearly observed. As ΔT is varied within Groups 1b and 2b only, a total of 50 flame spread simulations were performed to analyse the effect of this parameter considering the current approach.

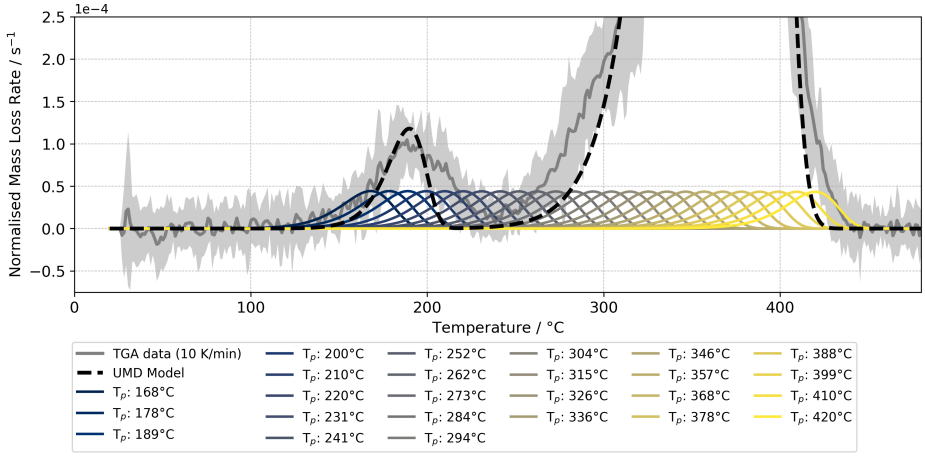

Figure 4.6: Variation of the R3 peak position by adjusting the peak temperature (T_p) incrementally between 168 °C and 420 °C. Each position creates a distinct pyrolysis model, used in the flame spread simulation to evaluate the impact of R3 position on the ROS.

The effects of the parameters T_p and ΔT on the ROS of the flame spread simulations were assessed as percentage variations relative, to a reference ROS, as described

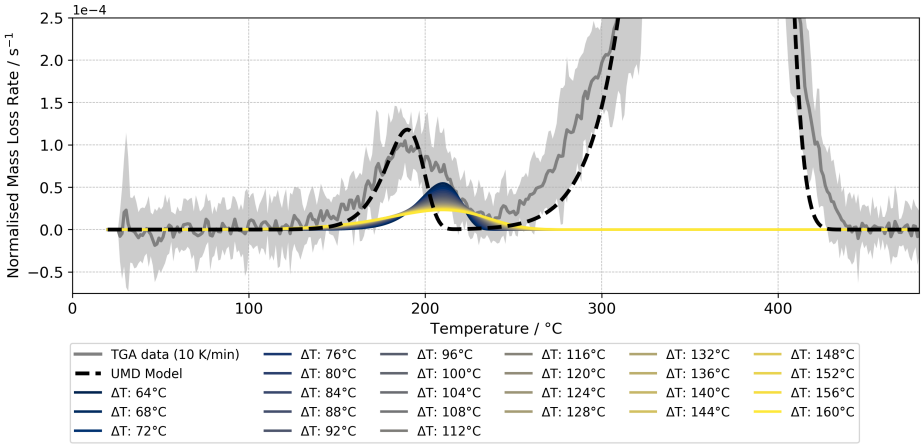

Figure 4.7: Variation of the R3 pyrolysis range (ΔT), shifted one-at-a-time between 64 °C and 160 °C. Each ΔT value results in a different pyrolysis model, used in the flame spread simulation to evaluate the impact of R3 width on the ROS.

by the following expression:

$$\text{Variation} = \frac{(\text{ROS}_{\text{param}} - \text{ROS}_{\text{ref}})}{\text{ROS}_{\text{ref}}} \times 100 \tag{4.4}$$

Here, $\text{ROS}_{\text{param}}$ denotes the ROS calculated from simulations with varied T_p and ΔT, while ROS_{ref} represents the ROS associated with the reference simulation case. The expression provided by Equation 4.4 enables the evaluation of negative and positive changes in the ROS, depending on the position and the amplitude of the small R3 peak.

In the analysis, simulation Cases 0a and 0b were chosen as references to determine ROS_{ref}. This provides a suitable starting point, as these cases employ the original UMD Model without the R3 peak. To ensure consistency, only simulations with the same gas-phase cell size were compared against each other. Specifically, Case 0a was used as the reference for simulation Groups 1a and 2a, while Case 0b served as the reference for Groups 1b and 2b. This baseline comparison allows to quantify the overall influence of incorporating the R3 peak into the UMD Model, assessing how the inclusion of a small R3 peak affects the ROS relative to the original model.

4.2.3.2 Sensitivity analysis with PC-based Sobol indices

The influence of the small R3 peak on the predicted ROS is further examined through a global sensitivity analysis using PC-based Sobol indices [Sudret, 2008]. The signif-

icance and interpretation of the indices remain the same as discussed in Chapter 2, Section 2.3.1, and Chapter 3, Section 3.3. However, in this case, the indices are derived using the Polynomial Chaos Expansion (PCE) approach, which approximates the simulation model with a set of polynomials, based solely on its input-output data. This method treats the simulation model as a "black box", representing its input parameters as random variables and constructing an expansion of orthogonal polynomials to capture their effects on the output. The PCE-based analysis described in this section was carried out using the Python library `chaospy` created by Feinberg and Langtangen [2015].

PCEs were specifically designed for facilitating uncertainty quantification and sensitivity analysis. It provides a significantly more computationally efficient framework for estimating sensitivity indices compared to Monte Carlo-based methods. Monte Carlo approaches require an extremely large number of model runs to accurately determine statistical properties, which can be prohibitively expensive for complex models such as the flame spread simulations considered in this work. This limitation was evident in the analysis conducted in Chapter 3, where tens of thousands of simulations were required to obtain reliable estimates of the indices.

The uncertainty intervals of the parameters defining the small R3 peak used in the PCE analysis were the same as those used for the one-at-a-time analysis. The uncertainty intervals are summarised in Table 4.5. The uncertainty intervals for the peak temperature (T_p) and the pyrolysis range (ΔT) follows the same approach as in the previous analysis. Yet, the uncertainty in the mass fraction (m_0) decomposed by the small peak is extended at its lower limit to account for even smaller peaks, which are considered to decompose between 0.5 % and 2 % of the total mass of the material.

Table 4.5: Uncertainty intervals of the parameters defining the small R3 peak.

Parameter	Uncertainty intervals	Units
Peak temperature (T_p)	[168; 420]	°C
Pyrolysis range (ΔT)	[64; 160]	°C
Mass fraction (m_0)	[0.005; 0.02]	-

The flame spread simulation is represented by a function f that provides the output of interest Y; f varies in space $\boldsymbol{x}$ and time t, and depends on a vector of input parameters $\boldsymbol{Q} = (Q_1, Q_2, ..., Q_d)$, as expressed in the following equation:

$$Y = f(\boldsymbol{x}, t, \boldsymbol{Q}) \tag{4.5}$$

Here, the model output of interest is the ROS, and the uncertain parameters are those describing the small peak, as defined earlier: T_p, ΔT, and m_0. A general polynomial approximation for f can be defined as:

$$f \approx \hat{f}(\boldsymbol{x}, t, \boldsymbol{Q}) = \sum_{n \in I_N} c_n(\boldsymbol{x}, t) \boldsymbol{\Phi}_n(\boldsymbol{Q}), \quad I_N = \{0, \ldots, N\} \tag{4.6}$$

where n ranges over I_N and N represents the highest order of the polynomials used in the expansion. The term $c_n(\boldsymbol{x}, t)$ denotes the coefficients of the expansion, and $\boldsymbol{\Phi}_n(\boldsymbol{Q})$ represents the polynomials in the expansion. The PCE is constructed so that the polynomials are orthogonal to the joint probability density function of the uncertain inputs. The three-term recurrence relation is used to compute the PCE [Feinberg and Langtangen, 2015].

The coefficients of the expansion $c_n(\boldsymbol{x}, t)$, also known as the Fourier coefficients, can be estimated using various methodologies, including intrusive and non-intrusive approaches [Feinberg and Langtangen, 2015]. Recently, Jamil and Brännström [2024] compared the performance of both intrusive and non-intrusive methods for quantifying uncertainties in pyrolysis models based on PCE. They concluded that the non-intrusive projection method led to faster convergence than the point collocation method, particularly when dealing with a limited number of uncertain inputs. Given these findings and the complexity of the flame spread simulation model, which makes intrusive methods impractical, the projection method was chosen for this work.

The projection method approximates the coefficients of the PCE using a numerical integration scheme. The Gaussian quadrature was employed, which requires the function to be evaluated at specific points, known as quadrature points, that correspond to samples of the input parameters. The number of samples is determined by the order of the PCE N and the number of uncertain input parameters d, as defined by: $(N+1)^d$. The PCE order is chosen to match the order used in the quadrature rule.

Once the PCE representation of the simulation model is available, the Sobol indices can be computed analytically, directly from its coefficients [Sudret, 2008]. The response expansion coefficients are simply gathered according to the dependency of each basis polynomial, square-summed and normalised. In other words, the variance of the model output is decomposed into the contributions of the individual polynomial terms, and the sensitivity indices are obtained by summing the variances associated with the terms corresponding to each input parameter. The first-order Sobol index for a given parameter is calculated from the variance of polynomial terms that depend

solely on that parameter, while the total-order Sobol index accounts for all terms where the parameter appears, including interaction effects.

In this study, two PCEs were developed for orders 2 and 3. The quality of these approximations was evaluated based on a global RMSE, using input-output data from the one-at-a-time analysis of Groups 1b and 2b. The best PCE approximation is determined based on the lowest value of global RMSE. For each order, the number of samples (and consequently the number of simulation runs) was 27 for the second-order PCE and 64 for the third-order PCE, given that the number of uncertain parameters describing the small peak is 3. The uncertainty in the ROS induced by these uncertain parameters is expressed in terms of the standard deviation.

4.3 Results and discussion

4.3.1 One-at-a-time analysis

The influence of the input parameters defining the small R3 peak is first examined qualitatively, focusing on their effects in simulations from Group 2b. This group is selected because its simulations exhibited the strongest response to variations in T_p and ΔT. This increased sensitivity is attributed to the larger fraction of material decomposed by the small peak in Group 2b, where it accounts for 2 % of the total material mass, compared to 1 % in Groups 1a and 1b. The impact of the decomposed mass fraction will be further explored in the next section.

The HRR responses to changes in the peak temperature T_p and the pyrolysis range ΔT are shown respectively in Figures 4.8a and 4.8b. Similarly, responses of the flame position curves to changes in T_p and ΔT are shown in Figures 4.9a and 4.9b. In these plots, the curves are colour-coded according to the specific values of T_p and ΔT used in each simulation, following the colour scheme previously introduced in Figures 4.6 and 4.7. These plots indicate that both the HRR and the flame position curves exhibit greater variability when T_p is varied compared to when ΔT is varied, suggesting that the peak temperature has a greater impact on the predictions than the peak width

The effect of the peak temperature T_p on HRR and flame spread is inverse; both model responses decrease as T_p increases. This trend is evident in Figure 4.8a, where the HRR curves shift to the right, particularly after the ignition phase ends and self-sustained flame spread begins. This behaviour occurs because at higher T_p values (see Figure 4.6), the material associated with the R3 peak decomposes only at elevated

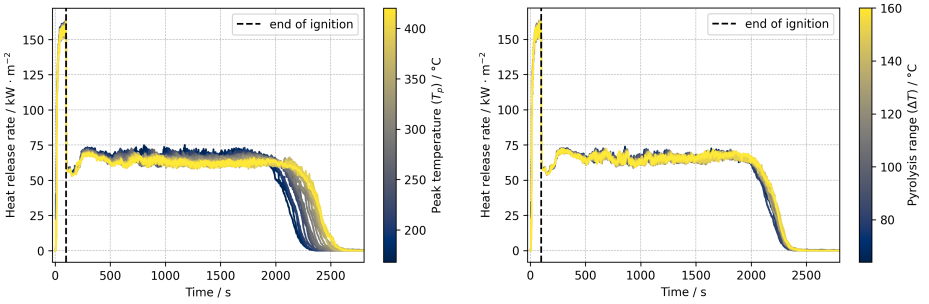

(a) (b)

Figure 4.8: Qualitative effects on the HRR induced by changes in the (a) peak temperature (T_p) and (b) pyrolysis range (ΔT) of the small peak in simulations from Group 2b.

temperatures, reducing the available combustible mass at lower temperatures. As a result, the delayed decomposition leads to a lower HRR, as shown in Figure 4.8a.

This reduction in HRR, in turn, lowers the heat flux reaching the sample surface, slowing down the heating process and reducing pyrolysis rates. Consequently, the flame propagates more slowly over the unburnt material. This effect is reflected in the flattened slopes of the flame position curves, particularly in Figure 4.9a. At the same time, Figure 4.8a also illustrates the opposite trend: as T_p decreases, the material pyrolyses earlier, releasing more mass for combustion at lower temperatures. This leads to earlier sample consumption and higher HRRs, which in turn enhances the spread. This effect is represented by steeper slopes in the flame position curves.

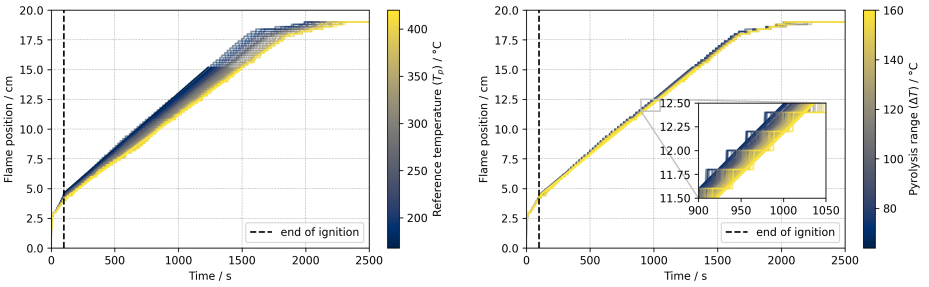

(a) (b)

Figure 4.9: Qualitative effects on the flame position curves induced by changes in the (a) peak temperature T_p and (b) pyrolysis range ΔT of the small peak in simulations from Group 2b.

Similarly, higher values of the pyrolysis range ΔT lead to a slight decrease in both the HRR (Figure 4.8b) and the slope of the flame position curves (Figure 4.9b). Initially, wider peaks were expected to increase the HRR, as higher decomposition rates at the peak tails would contribute more mass to combustion. However, a competing effect arises: as ΔT increases, the peak's maximum rates are reduced, as shown in Figure 4.7. This effect dominates because a greater fraction of mass decomposes at these lower rates. As a result, larger ΔT values lead to slower overall pyrolysis and lower HRRs.

The qualitative analysis suggests that variations in both T_p and ΔT produce a similar overall trend: increasing either parameter leads to an inverse effect on HRR and the slope of the flame position curves (Figure 4.9). However, the influence of ΔT is practically negligible compared to that of T_p. Therefore, from this point forward, the discussion will primarily focus on the effects of T_p and m_0 across all simulation groups described in Table 4.3.

4.3.1.1 Effects on the ROS

The predicted ROS values for each simulation within each group are plotted against the corresponding T_p values used in each simulation and presented in Figure 4.10. In this plot, the two gas-phase grid resolutions are distinguished by different markers: triangles represent the 1.5 mm resolution, while circles indicate the 2.0 mm resolution.

Solid markers highlight key positions of the R3 peak at 210 °C, 284 °C, and 420 °C, which correspond to locations of interest within the MLR temperature range, as previously illustrated in Figure 4.4. Additionally, ROS values for the reference simulation cases (Case 0a and 0b), which used the original UMD Model, are also included for comparison. Since the reference cases do not feature a small peak like R3, it is not meaningful to establish a direct relationship between ROS and the parameters defining the small peak. Therefore, their ROS values are represented as horizontal lines, serving as a baseline for comparison.

The trend observed in Figure 4.10 shows that the ROS decreases more rapidly at lower T_p values, with the rate of decline slowing as T_p increases. This suggests that at higher temperatures, ROS values gradually converge toward those of the reference cases (Case 0a and 0b), becoming nearly identical as T_p approaches 420 °C. Groups 1a and 2a, which share the same gas-phase cell size, align with Case 0a, while Groups 1b and 2b align with Case 0b.

Understanding this behaviour is crucial for assessing the impact of incorporating a small peak like R3 into the pyrolysis model. It highlights that the influence on

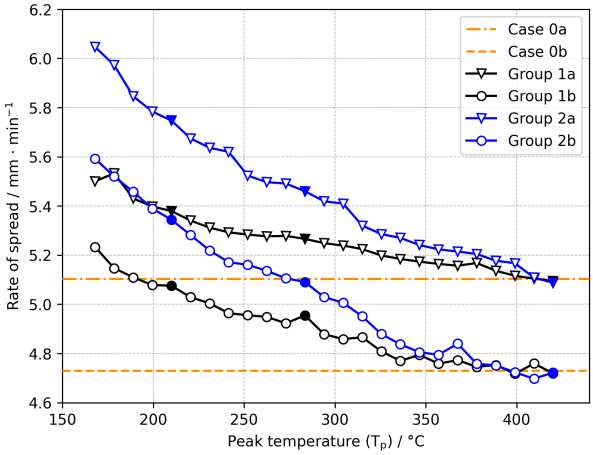

Figure 4.10: Effects on the ROS induced by changes in the peak temperature T_p of the small R3 peak. Results in black refer to peak mass fractions of $m_0 = 0.01$, and blue results refer to peak mass fractions of $m_0 = 0.02$. Solid markers highlight the positions of the R3 peak at 210 °C, 284 °C and 420 °C.

ROS is most significant when the small peak is positioned at lower temperatures and becomes practically negligible at higher temperatures.

Moreover, Groups 2a and 2b start with higher ROS values and show a steeper decline compared to Groups 1a and 1b. This observation suggests a stronger sensitivity of Groups 2a and 2b to T_p changes, indicating that the simulations in these groups are more affected by T_p than those in Groups 1a and 1b. This increased sensitivity comes from the larger mass fraction decomposed by the small peak in simulations from Groups 2a and 2b (2 % PMMA_{imp}, $m_0 = 0.02$), as opposed to simulations in Groups 1a and 1b (1 % PMMA_{imp}, $m_0 = 0.01$). When T_p is reduced, a greater amount of material in Groups 2a and 2b undergoes pyrolysis at these lower temperatures.

With this, more combustible gas is released earlier from a burning surface cell, leading to a larger flame. The flame in turn releases more heat and heats up surrounding, not yet burning, surface cells faster. Consequently, this feedback loop leads to an increased HRR and sustains the flame spread.

In this sense, the larger initial mass fraction in Groups 2a and 2b results in a more pronounced effect of T_p changes on the ROS, leading to the observed steeper decline in ROS as the material decomposes more rapidly at lower temperatures. This dynamic highlights the critical role of both T_p and m_0 in determining the ROS sensitivity to the inclusion of the small R3 peak in the original model.

Relative effects on the ROS

The influence of variations in the peak temperature T_p on the ROS is more clearly illustrated through its percentage change, as shown in Figure 4.11. For reference, the ROS of Case 0a is used as the baseline for Groups 1a and 2a, while Case 0b serves as the reference for Groups 1b and 2b. The grey-shaded region in Figure 4.11 denotes a 5 % variation around the reference cases (0a and 0b), which is highlighted as an indicator of low variation.

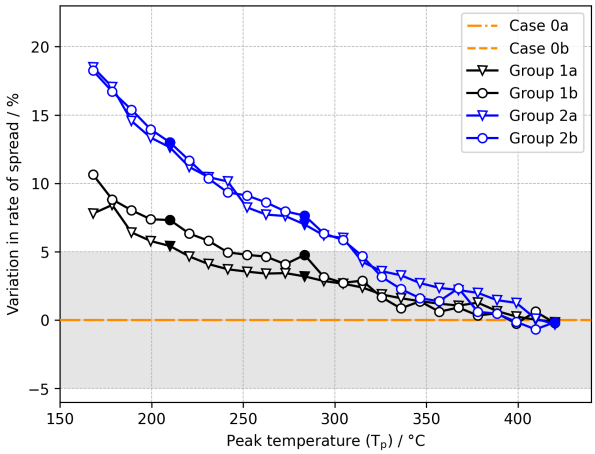

Figure 4.11: Variation in the ROS induced by changes in the peak temperature T_p of the small R3 peak, relative to the reference simulation Cases 0a and 0b. Solid markers highlight the positions of the R3 peak at 210 °C, 284 °C and 420 °C.

The plot in Figure 4.11 shows that percentage variations in ROS consistently exceed the 5 % threshold across all simulation groups as T_p decreases. In Groups 2a and 2b, this threshold is surpassed when R3 is positioned within the temperature range of approximately 168 °C to 310 °C. For Group 1a, the ROS exceeds this threshold when R3 is located between 168 °C to 210 °C, while in Group 1b, the threshold is surpassed for R3 placements within 168 °C to 240 °C.

The largest ROS increase observed is over 18 % for peaks with a mass fraction of 0.02 and 10 % for peaks with a mass fraction of 0.01, occurring when $T_p = 168$ °C. These maximal ROS variations, ranging from 10 % to 18 %, represent the theoretical upper limits of the ROS's sensitivity to the addition of the small R3 peak at 168 °C. Along with the intermediate variations observed as the R3 peak is shifted across the

pyrolysis temperature range, these results provide insight into the extent to which the predicted ROS responds to this adjustment in the original model.

Particular attention should be paid to the solid markers in Figures 4.10 and 4.11, which identify specific cases where the R3 peak is positioned at 210 °C, 284 °C, and 420 °C. These peak positions are especially significant as they improve the alignment between the model and the experimental TGA data by refining the fit at the shoulders of the main peaks in the original model. Among these configurations, the largest ROS variations occur when the R3 peak is positioned at 210 °C. This placement leads to an approximate ROS increase of 13 % for a mass fraction of 0.02 and 6 % for a mass fraction of 0.01, as shown by the solid markers in Figure 4.11.

In the context of the present theoretical study, these variations are considered to represent a significant influence on the ROS when the R3 peak is placed at 210 °C, particularly given that they result from the inclusion of a small peak decomposing only 1 % to 2 % of the material's total mass. However, in practical applications, the acceptability of such variability in the ROS depends on the specific context, and the degree of variability regarded as tolerable for a given application. This judgment should be informed by comparisons with experimental data and, most importantly, the associated experimental uncertainties. Typically, the predicted ROS should be evaluated relative to an experimentally averaged ROS and its uncertainty range to determine whether the observed variability falls within acceptable limits.

Implications for optimisation strategies

As shown in Figure 4.5, the fit to experimental TGA data improves across all tested R3 peak locations (solid markers in Figure 4.11) compared to the original model, with the best agreement achieved when R3 is positioned at 284 °C. However, for a fixed mass fraction, this position – while yielding the lowest RMSE relative to the TGA data – does not correspond to the largest variations in ROS. This distinction highlights a key trade-off between optimising model fit to TGA data and the sensitivity of ROS to the inclusion of the small R3 peak.

Although placing R3 at 284 °C ensures the most accurate reproduction of experimental MLR data, its impact on ROS remains relatively moderate compared to positioning it at 210 °C. This finding suggests that improving agreement with TGA data does not necessarily lead to proportional changes in ROS predictions. More importantly, it highlights which specific deviations between the original model and experimental data, illustrated in Figure 4.2, should be prioritised when refining the

model fit. In particular, adjustments in the low-temperature region should take precedence over those in the high-temperature range, as the ROS is more sensitive to variations in the lower-temperature region, making them more influential in determining ROS behaviour.

Effect of gas-phase resolution and validation

Another important factor influencing the ROS predictions in Figure 4.10 is the gas-phase cell size. In both simulation groups, higher-resolution cases (Group 1a and Group 2a) predict larger ROS values than their lower-resolution counterparts (Group 1b and Group 2b). In this setup, the 'a' denotes higher resolution, which leads to increased ROS predictions (see Table 4.3). Finer mesh resolutions improve the spatial accuracy of heat transfer calculations, resulting in higher heat fluxes reaching the sample and, consequently, greater ROS values. However, while finer resolutions theoretically enhance predictive accuracy, validation against experimental data is necessary to confirm actual improvements. Further validation is also needed to assess whether the ROS variations observed in this study translate into meaningful enhancements in model predictions.

Regarding experimental validation of the simulated ROS values, no small-scale flame spread data for MaCFP PMMA was available at the time of this study. However, a qualitative comparison can be drawn with Korobeinichev et al. [2018], who conducted horizontal flame spread experiments on cast PMMA of the same width (100 mm) under open-air conditions, placed on insulating material. Their sample was thinner (5 mm) than the 6 mm used by Fiola et al. [2021]. They reported a ROS of $6.0\,\mathrm{mm\,min^{-1}}$, while the baseline simulations in this study (original UMD Model) predicted $5.10\,\mathrm{mm\,min^{-1}}$ and $4.73\,\mathrm{mm\,min^{-1}}$ for gas-phase resolutions of 1.5 mm and 2.0 mm, respectively. Since thinner samples generally yield faster spread rates [Korobeinichev et al., 2018; Jiang et al., 2017], the predicted ROS values in this study appear reasonable.

Given also the lack of reported experimental uncertainties in the work of Korobeinichev et al. [2018], which further limits direct comparisons, the simulation models used here are considered an adequate representation of expected spread rates. The selected sub-models follow state-of-the-art practices within FDS for flame spread predictions. As such, these results highlight the importance of accounting for small MLR peaks in the pyrolysis model, particularly those occurring at lower temperatures, in accurately predicting ROS. Later in this thesis, specifically in Chapter 5,

small-scale flame spread experiments are conducted and used for further comparison with simulation results.

4.3.2 PCE-based analysis

To determine which of the chosen PCE orders best represents the general model behaviour, both second- and third-order PCEs were tested against the samples used in the one-at-a-time analysis. Specifically, input samples of T_p and ΔT from simulation Groups 1b and 2b were supplied to the PCE approximations to predict the ROS. It is important to note that such datasets were used solely for testing, and not for training the PCEs. The results for PCE orders 2 and 3 are shown in Figure 4.12, where the solid circles represent the PCE predictions of the ROS, and the white circles the actual FDS predictions.

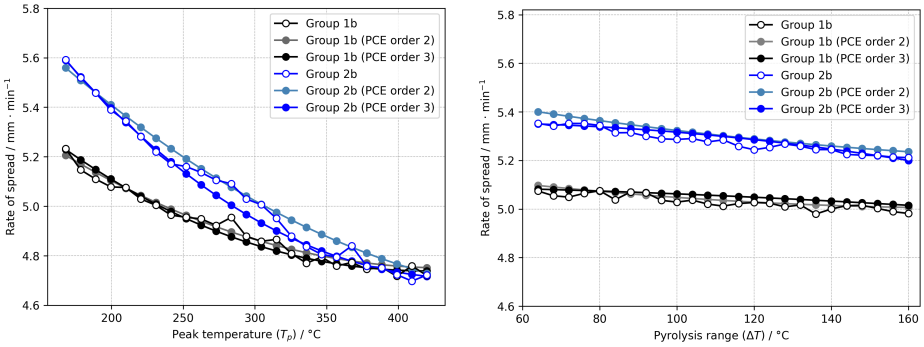

(a) (b)

Figure 4.12: Validation of PCE orders 2 and 3 against simulation data used in the one-at-a-time analysis.

From Figure 4.12 it can be seen that both PCE orders were able to capture the overall trend of the relationships between the ROS and the input parameters describing the small peak. As previously discussed, the fluctuations present in the FDS data are assumed to be artefacts related to the spatial resolution in the simulations. Therefore, not capturing these fluctuations in detail is not considered problematic. Instead, the focus is on capturing the general trends exhibited by the actual simulation data.

The proximity of PCE predictions and FDS predictions is measured by the RMSE. The RMSE results for each case in Figure 4.12 are presented in Table 4.6. It can be observed that for datasets in Group 1b, the lowest RMSEs correspond to PCE order 2, whereas for datasets in Group 2b, the lowest RMSEs correspond to PCE order 3.

These results indicate that the relationship between the ROS and the one-at-a-time variations in T_p and ΔT is better represented by the second-order PCE when the peak consumes 1 % of the total material mass, and by the third-order PCE when the peak consumes 2 % of the mass. This occurs because the second-order PCE is sufficient to capture the lower level of non-linearity observed for simulations in Group 1b. Similarly, the third-order PCEs can better capture increased non-linearities, which are more characteristic of the simulations in Group 2b.

Table 4.6: Root mean square errors (RMSE) calculated for each test dataset.

	RMSE (Group 1b)	RMSE (Group 2b)	Mean RMSE
PCE order 2	0.024	0.041	0.033
	0.019	0.031	0.025
PCE order 3	0.027	0.036	0.031
	0.028	0.019	0.023

4.3.2.1 Sensitivity analysis

The results obtained from the PCE analysis for orders 2 and 3 are presented in Table 4.7. Both PCE orders lead to similar estimations of mean and standard deviation: the mean ROS converges to $4.9\,\mathrm{mm\,min^{-1}}$, and the standard deviation converges to $0.2\,\mathrm{mm\,min^{-1}}$. The mean ROS represents the overall expected ROS, taking into account the uncertainty in all three inputs T_p, ΔT and m_0, while the standard deviation represents the variability around this mean value, representing the uncertainty in the ROS. In terms of relative values, this result corresponds to $\pm 8\,\%$ (two standard deviations) of variability in the ROS, induced solely by the uncertain parameters defining the small R3 peak.

Despite the consistent mean and standard deviation values obtained from both PCE orders, the sensitivity indices calculated from the second- and third-order PCE approximations show some non-negligible variability. As seen in Table 4.7, these differences are more significant for S1 and ST indices associated with parameters T_p and m_0. These differences can be attributed to the improved ability of higher-order polynomials to capture non-linearities. Since the sensitivity indices are calculated from the coefficients of the PCE, the inclusion of higher-order terms changes these coefficients and their contribution. Consequently, the calculated sensitivity indices can vary, even though the mean and standard deviation might not significantly change, as the overall distribution shape is well captured by the lower-order terms.

Table 4.7: Uncertainty quantification and Sobol sensitivity indices.

	PCE order 2	PCE order 3
Mean ROS ($\mathrm{mm\,min^{-1}}$)	4.938	4.931
Standard deviation ($\mathrm{mm\,min^{-1}}$)	0.219	0.224
S1 (T_p)	0.76	0.81
S1 (ΔT)	0.02	0.01
S1 (m_0)	0.12	0.09
S2 (T_p, ΔT)	0	0
S2 (T_p, m_0)	0.09	0.08
S2 (ΔT, m_0)	0	0
S3 (T_p, ΔT, m_0)	0.01	0.01
ST (T_p)	0.85	0.90
ST (ΔT)	0.03	0.01
ST (m_0)	0.22	0.18

For instance, with the PCE order 2, the S1(T_p) is equal to 0.76, indicating that 76 % of the uncertainty in the ROS stems from varying the position of the small peak (T_p) individually. In contrast, the PCE order 3 estimates this value to be 0.81 (81 %). In both PCE approximations, the estimations of the S2(T_p, m_0) indices are similar, showing that around 8 % to 9 % of the ROS uncertainty is caused by interaction effects between the peak position and the mass fraction of the small peak (m_0). Similarly, the S3 index, which indicates the interaction effects when all three inputs (T_p, ΔT, and m_0) are varied together, also does not change significantly between the PCE orders. Therefore, the variations observed in the ST indices between PCE orders mainly reflect the variation in the S1 indices.

Although the estimates of the ST indices vary between PCE orders, the overall ranking of parameter importance remains similar in both polynomial approximations. The consistently large values of ST(T_p) highlight the dominant role of the peak position (T_p) in the ROS uncertainty. To a considerably smaller extent, the peak mass fraction (m_0) is the second most important factor, followed by the minor role of the peak width (ΔT). This ranking of parameter importance aligns with the findings of the one-at-a-time analysis, which also demonstrated that the influence of the small peak on the ROS was primarily governed by T_p.

It is worth pointing out that the indices capture the influence of the parameters not only at the specific samples used in the one-at-a-time analysis, but across the entire parameter space defined by the uncertainty intervals of each parameter. They

therefore provide a global measure of parameter importance that extends beyond the limited scope of discrete sampling points.

To better illustrate how the parameters defining the small peak influences the ROS, the sensitivity indices in Table 4.7 estimated based on the third-order PCE are shown in a bar plot in Figure 4.13. The plot highlights the dominance of the peak temperature T_p, with both first-order (S1) and total-order (ST) indices being significantly higher than those of m_0 or ΔT. While m_0 exhibits limited sensitivity, ΔT has negligible impact, consistent with the trends discussed above.

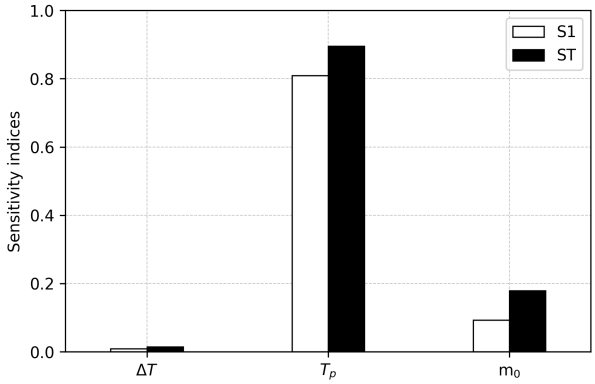

Figure 4.13: First- (S1) and total-order (ST) indices of the parameters defining the R3 peak, estimated using the third-order PCE.

It is important to distinguish between the significance of the S1 indices and the one-at-a-time analysis. The one-at-a-time approach examines the effect of varying a single parameter while holding all others constant, highlighting the influence of individual parameters. However, it does not capture the full extent of each parameter's contribution to ROS variability over its full range. This limitation arises because it only considers isolated changes rather than the cumulative effect of a parameter within the wider parameter space.

In contrast, the S1 indices quantify the influence of each parameter on output variability across the parameter space, isolating its independent effects while considering its contribution to overall variability. As a result, the individual analysis provides useful preliminary insights, whereas the S1 indices provide a more comprehensive and quantitative assessment of parameter importance.

Figure 4.14 shows the response surface illustrating how variations in ROS relate to the two most influential parameters of the small peak: the peak temperature T_p

and the initial mass fraction m_0. The ROS values were obtained from the third-order PCE approximation, and the variations are expressed relative to the ROS of Case 0b. The colour scale highlights certain regions in the parameter space, which visually demonstrate how different combinations of T_p and m_0 affect the ROS. For example, regions where T_p is low and m_0 is high result in the largest increases in ROS, represented by yellow tones, while dark blue areas indicate lower ROS variations associated with higher T_p and lower m_0 values.

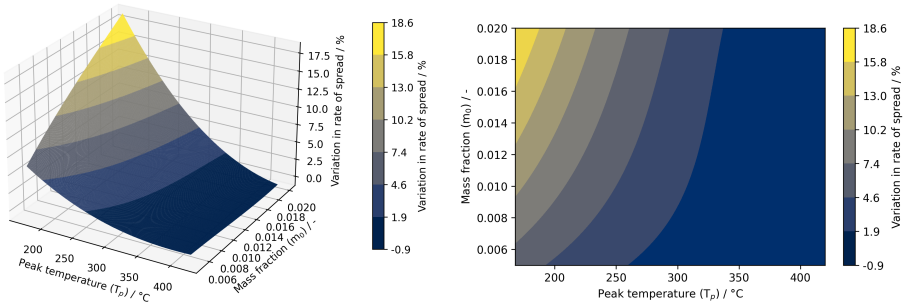

(a) (b)

Figure 4.14: Response surface highlighting regions in the parameter space where different combinations of T_p and m_0 influence the ROS response (%). (a) 3-D surface (b) 2-D projection.

4.4 Conclusions

In the study presented in this chapter, the effect of accounting for a small fluctuation in the MLR observed in TGA data of PMMA on the predictions of a flame spread simulation was investigated. The results suggest that the common assumption that MLR fluctuations can be neglected in pyrolysis modelling may not always be valid. It was shown, that there is at least one scenario where the MLR fluctuations had a non-negligible effect on the predicted ROS, highlighting the need for further investigation.

The following findings of the study are highlighted:

- The peak temperature has the most significant effect on ROS, followed by the peak mass fraction, while peak width has little or no effect.

- The inclusion of a small peak can significantly alter ROS predictions when located at lower temperatures, whereas peaks at higher temperatures have minimal effect.
- This effect becomes more pronounced for larger mass fractions, with ROS increases of 6 % to 13 % observed for peaks decomposing 1 % to 2 % of the total sample mass.
- In the context of this theoretical study, these variations reflect the global behaviour of the simulation model, which incorporates state-of-the-art sub-models for predicting flame spread in FDS. Accordingly, these results emphasise the importance of refining pyrolysis models by considering small MLR peaks: while those occurring at higher temperatures can be reasonably ignored, those at lower temperatures can lead to enhanced spread rates and should not be overlooked.
- In practical applications, the acceptability of these variations in ROS will ultimately depend on the specific context and the level of uncertainty deemed tolerable. Ideally, this should be assessed by comparison with experimental data, particularly taking into account the associated uncertainties.

Chapter 5

Horizontal flame spread: experiment and simulation

5.1 Introduction

The sensitivity analysis studies presented in Chapters 3 and 4 both considered small-scale horizontal flame spread simulations conducted using FDS. Given the focus on understanding how solid-phase parameters influence simulation predictions of interest, gas-phase modelling relied mostly on FDS default settings. Each study used a different parameter set to describe PMMA pyrolysis and heat transfer, and explored how changes in these parameters affected important model predictions such as the ROS and HRR.

An important point, however, is that none of these simulation models have been validated against experimental data. Although theoretical investigations are an important tool for improving the understanding of highly complex models such as the simulations in question, validation is necessary. This is because the ultimate objective is that these simulation models are able to predict flame spread in real fire scenarios with a sufficiently good degree of accuracy. Moreover, up to this point, none of the flame spread simulation models investigated in previous chapters have been assessed in more detail apart from their ROS and HRR predictions.

The purpose of this chapter is to address this gap. A small-scale flame spread experiment was conducted in the horizontal configuration and measurements of surface and in-depth temperatures were taken to determine the ROS and full temperature fields within the solid. The experiments were performed by the author of this thesis, in collaboration with the Fire Research Centre at the University of Edinburgh, following a methodology developed and described mainly by Morrisset et al. [2023, 2024].

Readers of this thesis are strongly encouraged to consult these original publications for a more detailed understanding and information on the experimental methods.

The simulations are built as simplified representations of the experiment and follow setups similar to those explored in earlier chapters. Predicted temperature profiles within the solid are compared against experimental measurements, along with ROS values. The sensitivity analysis in this chapter focuses on how variations in gas-phase grid resolution influence simulation predictions, namely, in-depth temperature profiles, surface heat fluxes near the flame, and ROS. To explore this, four different gas-phase cell sizes are tested.

5.2 Methods

5.2.1 Experimental setup

The flame spread experimental setup described here closely resembles the simulation cases studied in Chapters 3 and 4. In both setups, the sample is ignited at one end, leading to a self-sustained horizontal flame spread over a PMMA sample, with all measurements taken along the centreline of the sample. The main differences between the experimental setup and the earlier simulation cases are related to the sample dimensions and the boundary conditions. Specifically, the experimental samples were thicker and narrower, and the rear and side faces were water-cooled rather than insulated.

Transparent cast PMMA samples measuring 50 mm × 200 mm with a thickness of 12 mm were used. Each sample was tightly fitted into an aluminium holder to maintain isothermal boundary conditions and promote a uniform flame front. Ignition was achieved using a 0.5 mm diameter hot wire (80 % Ni / 20 % Cr), powered at approximately 70 W. The wire remained in contact with the sample for around 90 s before being withdrawn, after which the flame spread became self-sustained. An overview of the experimental setup before and after ignition is shown in Figures 5.1 and 5.2, respectively.

Experiments were conducted in open air, under natural buoyancy conditions. To further stabilise the environment near the flame, a metal mesh, shown in Figure 5.2, was placed around the sample holder to shield the flame from random air drafts and minimise flow instabilities. This metal mesh was not part of the original setup used in the experiments by Morrisset et al. [2024] but was introduced in the trials reported here.

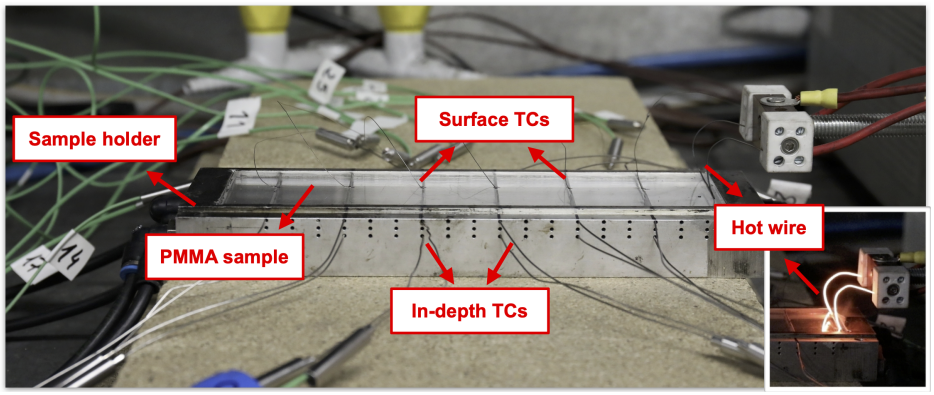

Figure 5.1: Overview of the flame spread experimental setup, before ignition. Temperature measurements were collected from six evenly spaced stations of thermocouples along the sample.

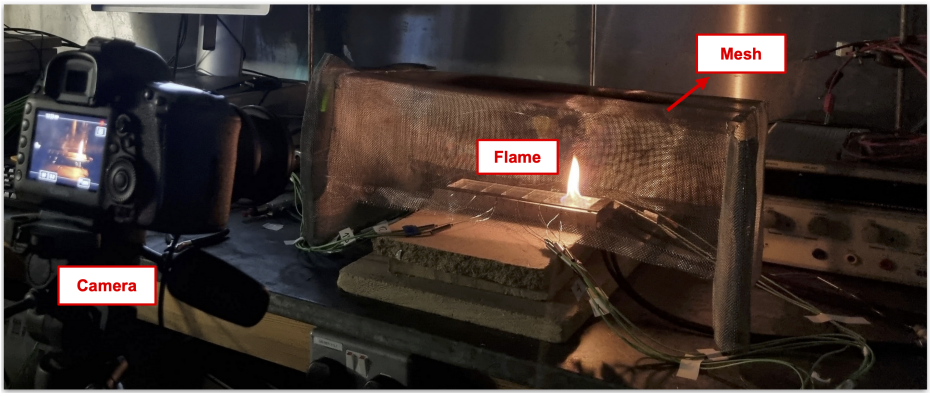

Figure 5.2: Overview of the flame spread experimental setup, after ignition. A metal mesh around the setup was used to shield the flame from random air drafts.

Temperature measurements were taken at the sample surface and at depths of 3 mm, 6 mm, and 9 mm. Thermocouples (TCs) were installed at six evenly spaced locations along the sample length, at 30 mm intervals, as shown in Figure 5.1. Each of these six measurement stations contained one surface thermocouple and three in-depth thermocouples. The thermocouple beads were aligned with the centreline of the sample.

Surface temperature measurements were obtained using 0.25 mm K-type thermocouples, fused to the sample so that the thermocouple bead was levelled with the surface. In-depth temperature measurements were made using 0.75 mm diameter

sheathed K-type thermocouples inserted from the side of the sample to reduce thermal interference from the thermocouple [Pope et al., 2022]. Placement of each in-depth thermocouple was achieved using a CNC mill which both drilled and countersunk the holes for the thermocouples to improve contact at the thermocouple tip [Morrisset et al., 2024]. The temperatures of the rear face of the sample were not measured, and were approximated to be the same as the inlet and outlet cooling water.

As shown in Figure 5.2, the experiment was also recorded using a camera. These recordings provide an alternative method for determining the ROS; however, this method is not presented here. Instead, the results are analysed and discussed solely based on thermocouple measurements. To evaluate repeatability and variability between trials, all experiments were conducted in triplicate.

Temperature reconstruction method

According to Morrisset et al. [2023], the temperature reconstruction method aims to determine the thermal gradients within the sample from the temperature measurements provided by the thermocouples. First, these measurements are used to determine the ROS between thermocouple stations by identifying the flame arrival times at each station. The arrival of the leading edge of the flame is defined as the moment when the surface thermocouple records 350 °C, as in Morrisset et al. [2024]. However, it is worth noting that lower temperatures could also be considered for defining flame arrival. Using a phosphor thermometry technique, studies by Burnford et al. [2024] have shown that surface temperatures at the flame leading edge exhibit a local maximum of 320 ± 20 °C, while temperatures in the pyrolysis region remain within the 300 °C to 350 °C range.

As the ignition process introduced transient behaviour during the initial stages of flame spread, data from the first 30 mm of spread were excluded from the analysis. Similarly, measurements from the last 30 mm were not included to avoid potential end-effects. By excluding measurements from the first and last stations, the ROS can be assumed to be in a steady state. Under this assumption, time-resolved temperature data can be converted to spatially resolved temperatures. This in turn allows the determination of temperatures at any position in front of the flame and in depth, which can be interpolated to obtain a two-dimensional temperature distribution within the sample.

Thermal gradients are determined using an overall mean ROS. For each replicate, three local ROS values are calculated during the self-sustained phase, based on measurements from the four central thermocouple stations (from 60 mm to 150 mm).

With three replicates, this results in nine local ROS values. The overall mean ROS, representing the whole experiment, is computed as the average of these nine values, with the standard deviation (σ) calculated accordingly. The uncertainty in the overall mean ROS is reported as $1.96 \cdot \sigma$, corresponding to a 95 % confidence interval. The results are compared with those reported by Morrisset et al. [2024] for the same experiment, and used as validation data for the flame spread simulations conducted with FDS.

5.2.2 Flame spread simulation

The flame spread simulation setup was designed as a simplified representation of the horizontal flame spread experiment. It builds on the simulation setups studied in previous chapters, particularly on the setup presented in Chapter 4. The same FDS version FDS6.7.9-0-gec52dee-HEAD is used, as well as the remaining simulation settings representing main phenomena like combustion, radiation, pyrolysis and heat transfer.

The parameter set currently recommended by MaCFP to model PMMA pyrolysis is used as described in the work of Fiola et al. [2021], with no modifications. The set was introduced in Chapter 4, Section 4.2.1 and provides thermophysical, optical, and kinetic properties. The default one-dimensional heat conduction model is applied, while the gas-phase settings remain unchanged and consistent with the previously studied simulation.

The boundary condition at the back face of the sample was set to a constant temperature of 15 °C using the `TMP_BACK` function in FDS. This approximation is based on the averaged temperature measurements of the cooling water, which remains relatively stable throughout the experiment. Although this is a simplification, it provides a reasonable representation of the thermal conditions at the back face of the sample.

The sample dimensions are set exactly as in the experiment, measuring 50 mm × 200 mm, with a thickness of 12 mm. The computational domain extends 300 mm × 150 mm × 100 mm in the x, y, and z directions and is divided into 36 cubic meshes, each with an edge length of 50 mm, to enable parallel computation. An overview of the domain and meshes is presented in Figure 5.3.

The ignition patch, shown as the dark grey area on the right-hand side of the sample, extends 16 mm × 50 mm in the x and y directions. This size is based on the approximate area of the sample that was near the hot wire during ignition in the

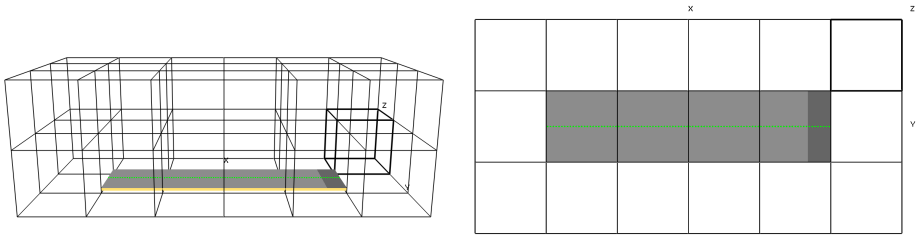

(a) (b)

Figure 5.3: Overview of the flame spread simulation, developed as a simplified representation of the horizontal flame spread experiment. (a) Perspective view and (b) top view showing domain and its subdivisions into 36 cubic meshes.

experiment. An external heat flux of 93.3 kW m^{-2} ($\approx$ 74 W) was applied to this patch for 90 s to ignite the sample, similarly to what was done in the experiment.

Four different gas-phase resolutions were tested, with cell sizes of 1.0 mm, 1.5 mm, 2.0 mm, and 2.6 mm. The cell sizes were determined by subdividing each computational mesh into 19, 25, 33, and 49 cells, respectively. The number of divisions was intentionally kept uneven to ensure that a row of gas cells always aligns with the central line of the sample. This approach allows the cell sizes to be adjusted while maintaining the dimensions of the sample, sample holder, domain, and meshes exactly as described above in all simulation cases. Moreover, it ensures that the amount of sample available for pyrolysis and combustion remains consistent in every case.

Devices were positioned along the centreline of the sample to record the HRRPUV in the row of gas-phase cells, as described in Chapter 3, Section 3.2.2.1, to determine the ROS. Temperature profiles within the solid were captured along the centreline of the sample, not only at every 30 mm from the ignition end, as in the experiment, but also at additional positions. These additional positions corresponded to the six gas cells upstream the thermocouple station at 90 mm from the ignition end. The exact positions change slightly according to the grid resolution used in each case.

The in-depth temperature profiles from the simulations are obtained using two different approaches. In the first, the temperature reconstruction method used in the experiments is applied to the simulation. That is, temperature profiles at every 30 mm are collected using devices, and the method is applied accordingly, reconstructing thermal gradients as if longitudinal conduction in the solid were accounted for in the model. In the second, the actual thermal gradients are presented, showing only the

temperature profiles normal to the sample surface. These results are analysed for all tested gas-phase resolutions, with discussions focusing on the potential implications of using the one-dimensional heat conduction model to predict flame spread in FDS.

5.3 Results and discussion

5.3.1 Experimental results

Temperature measurements from all six thermocouple stations are shown in Figure 5.4a for the first trial of the flame spread experiment (rep_01). The plot shows six sets of four time-resolved temperature profiles corresponding to the sample surface and three depth positions (3 mm, 6 mm and 9 mm). The dashed line at 350 °C indicates the defined flame arrival threshold.

It can be observed that all stations follow an apparently similar trend: a gradual increase in temperature followed by a sharp rise when the flame arrives at the respective location. The surface temperature shows the most abrupt rise, reaching the flame arrival threshold, while the depth temperatures show progressively smoother increases with depth. The repeated trend in the plot reflects the sequential heating of different stations as the flame spreads across the sample.

By skipping the first and last thermocouple stations, the data from the four central thermocouple stations are considered similar enough to assume steady state flame spread. Accordingly, the four central sets of curves shown in Figure 5.4a can be plotted on the same time scale. This is done over the three experimental replicates to obtain overall averages of surface and in-depth temperatures over the 200 s before flame arrival, as shown in Figure 5.4b. The shaded areas correspond to 1.96 times the standard deviation, taking into account the variability both within and between replicates.

Using the recorded flame arrival times at each thermocouple station, and the known spacing between stations, an overall average ROS of $3.11 \pm 0.17\,\mathrm{mm\,min^{-1}}$ was determined across all replicates. This ROS was then used to transform the time-based temperature profiles before flame arrival (Figure 5.4b) into spatial profiles ahead of the flame front. The resulting dataset, shown in Figure 5.5a, is plotted in reverse order to facilitate a more intuitive interpretation of the temperature distribution upstream from the flame.

The surface and in-depth temperature profiles shown in Figure 5.5a were then arranged into a two-dimensional array, which was subsequently colour-coded to generate the full temperature field within the solid and ahead of the flame front, as presented

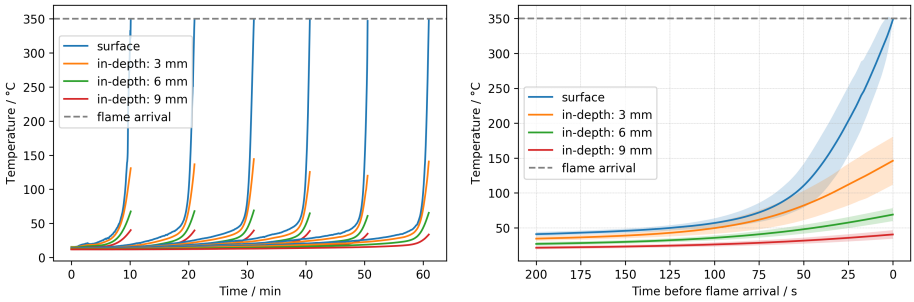

(a) (b)

Figure 5.4: Experimental temperature measurements from thermocouples up to flame arrival at 350 °C. (a) Data from all six stations over time for rep_01. (b) Averaged temperature profiles across all three replicates, excluding the first and last stations.

in Figure 5.5b. The temperature distribution provides a spatial representation of the thermal gradients within the PMMA sample, highlighting the progressive heating of the material due to solid-phase heat conduction. The vector field was obtained by computing the negative temperature gradients in both the longitudinal and normal directions of the sample.

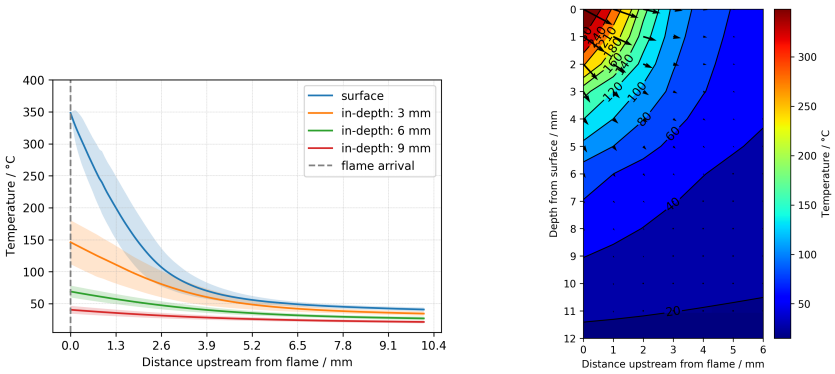

(a) (b)

Figure 5.5: Temperature profiles at the surface and within the PMMA sample. (a) Average temperatures along the distance ahead of the flame (b) Full temperature field within the solid, obtained using data from (a).

The resulting profile in Figure 5.5b closely resembles the in-depth temperature field reported by Morrisset et al. [2024] for horizontal flame spread. The overall trend remains consistent, with peak temperatures concentrated near the surface and the

flame leading edge, and gradually decreasing with depth. Compared to the lateral and downward flame spread experiments investigated in the referenced study, the horizontal case shows higher temperatures ahead of the flame front. This is due to enhanced radiative preheating, as the increased view factor between flame and sample in the horizontal configuration leads to greater radiative heat transfer Morrisset et al. [2024].

Notably, the inclination of the gradients is similar in both studies, indicating that the relative contributions of the longitudinal and normal conductive heat fluxes within the sample remain comparable. This consistency is to be expected given the identical PMMA samples and measurement techniques used in both studies. The main difference is the slightly greater thermal penetration observed here, as indicated by the isolines. This is likely due to the addition of a metal mesh to stabilise the flame – a modification to the original setup explored by Morrisset et al. [2024]. Without the mesh, the flame is more prone to flow instabilities, which can increase convective cooling and reduce thermal penetration.

However, the most significant effect of the metal mesh is seen in the uncertainties associated with the mean ROS, as shown in Table 5.1. The increased flame stability in this study improved repeatability and reduced the variability between replicates. In contrast, the absence of the mesh in Morrisset et al. [2024] resulted in a significantly larger uncertainty (19.7 %) compared to the 5.5 % reported here.

Table 5.1: Comparison between mean ROS values with uncertainties given as $1.96 \cdot \sigma$, for a 95 % confidence interval.

Reported by	Rate of spread / $\mathrm{mm\,min^{-1}}$	Relative uncertainty / %
Morrisset et al. [2024]	2.54 ± 0.50	19.7
This work	3.11 ± 0.17	5.5

For completeness of the analysis and to provide additional reference data for comparison with simulations, flame arrival times from all six stations across all replicates were used to generate the plots shown in Figure 5.6. Figure 5.6a shows the flame position as a function of time for each experimental trial. The data from all three replicates (rep_01, rep_02 and rep_03) are shown alongside the mean values, indicated by the black circular markers. The nearly linear trend suggests that the global rate of spread remains approximately constant throughout the experiment, although small variations between replicates can be observed.

Figure 5.6b provides a more detailed look at the local ROS between thermocouple stations, plotted against distance from the ignition end of the sample. The plot reveals a clear trend: the flame spread begins more slowly, accelerates progressively until approximately 135 mm, and then decelerates as it nears the far end of the sample. This acceleration phase can be attributed to the gradual growth of the pyrolysis zone below the flame. Initially, only a small portion of the material is undergoing pyrolysis, producing a relatively weak and short flame. As the pyrolysis zone extends, the flame grows in height and strength, enhancing heat feedback to the material and thereby increasing the ROS.

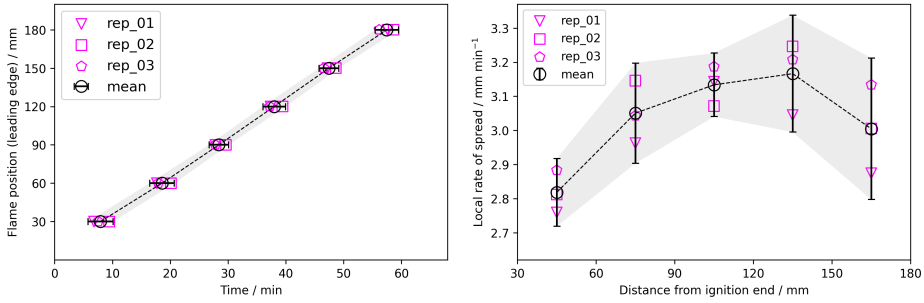

(a) (b)

Figure 5.6: Measurements from all three experimental replicates: (a) Flame position as a function of arrival time at each thermocouple station. (b) Local rates of spread between thermocouple stations along the sample.

The subsequent decrease in ROS beyond 135 mm is likely attributed to the proximity of the downstream boundary, where the sample comes into direct contact with the water-cooled sample holder. This creates a heat sink effect, limiting the thermal feedback required to sustain a high spread rate. As a result, the flame intensity is locally reduced, leading to a noticeable deceleration of the flame leading edge.

This behaviour highlights why the thermocouple readings at 30 mm and 180 mm should be excluded from the steady-state assumption: both are influenced by boundary effects that introduce additional variability, particularly in regions where the flame spread has not yet stabilised. More importantly, even if only the measurements of the thermocouple stations between 60 mm and 150 mm are considered, some variability remains as the flame still appears to be accelerating.

Recognising this variability is essential when assessing the plausibility of assuming steady-state flame spread, which is the fundamental assumption enabling the application of the temperature reconstruction method to obtain the in-depth temperature

profiles in the solid. Whether this level of variation is acceptable or not ultimately depends on the context and application. Regardless, it is necessary that such variability is accounted for in the reported uncertainties of the overall mean ROS, ensuring that differences both within and between replicates are properly reflected.

5.3.2 Validation

The simulation results for each of the four tested gas-phase cell sizes (1.0 mm, 1.5 mm, 2.0 mm, and 2.6 mm) are compared against the experimental data presented in the previous section. The focus of the discussion is on the ROS predicted by the simulations and the temperature profiles within the solid.

Predicted rates of spread

Figure 5.7 is essentially a recreation of Figure 5.6, but now including the data obtained from the post-processed simulation results. Figure 5.7a shows the tracking of the flame leading edge throughout the simulation, which was used to calculate the ROS values shown in Figure 5.7b.

At least three important observations can be made from Figure 5.7a:

(i) All simulation cases exhibit a linear flame advance during the self-sustained phase, which is consistent with the overall linear trend observed in the experimental data, as well as in similar plots presented in Chapters 3 and 4.

(ii) Among the simulation cases, the one using 2.0 mm cells produced results that most closely align with the experimental data, as also observed in Figure 5.7b.

(iii) The ROS increases with mesh refinement, i.e., as smaller gas-phase cell sizes are used. Although the results have not converged, the differences between the flame position curves become progressively smaller with increasing resolution. The simulation using the coarsest grid (2.6 mm cells) stands out as significantly detached from the others.

Regarding observation (iii), the difficulty in achieving grid convergence in FDS is a known issue, as also discussed in Chapter 3. This limitation has been associated with the approach FDS uses to compute the convective heat transfer coefficient, which includes an explicit dependence on the gas-phase cell size, establishing an inverse relation. This inverse relation is established due to the small cell sizes employed. This makes $2L/\delta n$ the maximum value in Equation 2.14, leading to $h = 2k/\delta n$, the

DNS limit in FDS. The convective heat flux is then obtained from the gas temperature gradient at the wall surface, which requires the gradient to be sufficiently well resolved. This creates a resolution sensitivity that is not purely numerical but instead embedded in the model formulation itself, and remains a recognised limitation of FDS that has only recently been addressed [McGrattan and Floyd, 2021; Dehghani et al., 2025].

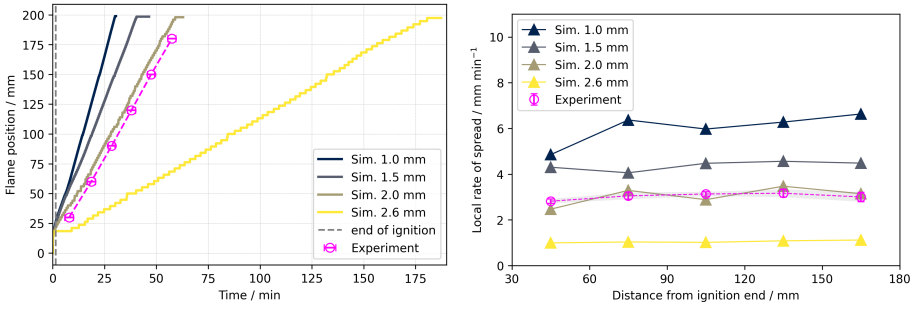

(a) (b)

Figure 5.7: Simulation results using different gas-phase cell sizes showing (a) flame position over time and (b) local rates of spread along the sample. Experimental averages from Figure 5.6 are included for comparison.

The local ROS values presented in Figure 5.7b for each simulation case were determined as the slope of the linear fits applied over every 30 mm segment along the sample, as indicated on the x-axis. The aim of this plot is to illustrate that the ROS predictions also exhibit some variability depending on which sections of the flame position curves are used in the calculation. These variabilities stem from small oscillations in the flame position curves, visible in Figure 5.7a, which are associated with numerical artefacts affecting the heat transfer to the solid and, consequently, the spread behaviour.

Furthermore, Figure 5.7b shows that these local ROS fluctuations do not follow the clear acceleration–deceleration trend observed in the experimental data (see Figure 5.6b). In particular, the final deceleration in the flame front near 165 mm, attributed to the cooled end of the sample, is not captured by the simulation model. This limitation arises from the one-dimensional heat conduction model used in the simulations, which only accounts for heat conduction normal to the surface and neglects conduction in the longitudinal and lateral directions.

As in the experimental analysis, the calculation of an overall mean ROS for each simulation case neglects the local ROS values at 45 mm and 165 mm, shown in Figure 5.7b, such that any influences of end effects are not included. Only those ROS

values in the central section of the sample, from 60 mm to 150 mm, are taken into account in the calculation. The associated variability is quantified using $1.96 \cdot \sigma$, based on the three ROS values from this central range. The resulting ROS values are listed in Table 5.2 and also shown graphically in Figure 5.8, alongside the experimental data. The experimental results refer to the ROS values previously presented in Table 5.1, both from this work and from the study by Morrisset et al. [2024]. These are shown as shaded bands, representing the range between the lower and upper uncertainty bounds.

Table 5.2: Predicted ROS averages and their associated variabilities obtained from each simulation case.

Gas-phase cell size / mm	Predicted rate of spread / mm min^{-1}
1.0	6.21 ± 0.33
1.5	4.37 ± 0.43
2.0	3.22 ± 0.48
2.6	1.05 ± 0.06

The plot in Figure 5.8 reveals a clear trend between the predicted ROS and the employed gas-phase cell sizes: as the cell size increases, the predicted ROS decreases in an approximately linear fashion. The cause of this inverse quasi-linear relationship is currently unclear and further investigation is required to better understand this relationship.

In addition, this trend may also be influenced by the way convective heat transfer is modelled in FDS, where an explicit dependence on cell size exists. As previously discussed, finer gas-phase grid resolutions can enhance the heat fluxes from the gas phase to the solid, thereby increasing the predicted ROS. However, the opposite effect has also been pointed out in previous chapters, where it was observed that above a certain gas-phase cell size, the simulation model fails to sustain the spread after the ignition phase. This threshold cell size appears, however, to be dependent on the parameter set used to model PMMA pyrolysis.

That is, in Chapter 3, where PMMA properties were described using the parameter set developed by Hehnen and Arnold [2023], flame spread was sustained at a gas phase resolution of 5 mm. On the other hand, in Chapter 4 and in the present chapter, where the parameter set recommended by the MaCFP Working Group was used, self-sustained flame spread was not achieved for cell sizes larger than about 2.5 mm. This suggests that the observed resolution sensitivity may also be related to

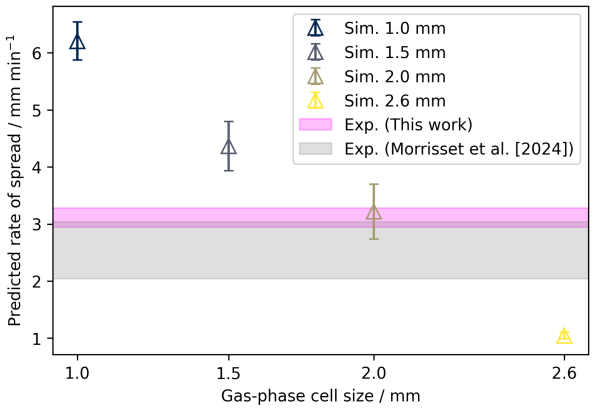

Figure 5.8: Predicted ROS averages and associated variabilities plotted against the gas-phase cell sizes used for each simulation case, compared with experimental results.

the pyrolysis parameters and their interaction with the heat transfer mechanisms of the model.

Predicted surface and in-depth temperature profiles

The temperature profiles from the simulation case using 2 mm cells are shown in Figure 5.9, as it produced ROS values closest to the experimental measurements. The plots look very similar to the experimental results in Figure 5.4, as the same temperature reconstruction method was applied to the simulation data. Figure 5.9a presents the time series of surface and in-depth temperatures calculated at 30 mm, 60 mm, 90 mm, 120 mm, 150 mm, and 180 mm positions along the sample. The averaged profiles in Figure 5.9b were computed in the same way as for the experiments, considering only the four central locations and excluding the first and last, which are nearest to the ignition and extinction ends of the sample.

Figure 5.9a shows that the overall temperature evolution as the flame approaches each location is generally similar to the experimental trend. In both cases, a gradual temperature rise is followed by a sharper increase at the surface once the flame arrives at each respective location. However, the simulated temperatures just before these sharp rises are noticeably higher than those observed in the experiments, indicating that surface temperatures were already significantly higher before the flame arrival.

This effect is more clearly illustrated in Figure 5.9b, which shows the averaged temperature profiles over the 195 s prior to flame arrival. Under the steady-state flame

spread assumption, the time-resolved data can be converted to spatially-resolved profiles by multiplying the time axis by the predicted ROS of 3.22 mm min^{-1}. The resulting upstream temperature distributions relative to the flame front are shown in Figure 5.10a. Figure 5.10b presents the same experimental measurements shown earlier in Figure 5.5a, repeated here to facilitate comparison.

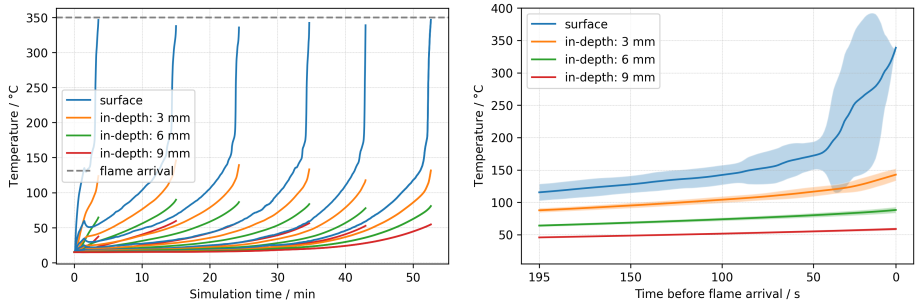

(a) (b)

Figure 5.9: Predicted surface and in-depth temperature profiles up to flame arrival at every 30 mm along the sample. (a) Over simulation time and (b) Averaged profiles excluding profiles nearest to the ignition and extinction ends of the sample.

As shown in Figure 5.10a, the simulation predicts substantially higher temperatures ahead of the flame front, both at the surface and in-depth, compared to the experimental results presented in Figure 5.10b. These elevated temperature profiles suggest that the preheating of the sample ahead of the flame is much greater in the simulation. In contrast, the experimental profiles show a more localised heating region, with temperatures only increasing significantly closer to the flame. For example, at a distance of about 10.4 mm from the flame front, the simulated surface temperature reaches about 120 °C, whereas in the experiments both the surface and depth temperatures remain below 50 °C.

Despite the discrepancies observed upstream from the flame, the simulated in-depth temperature profiles in the near field (within approximately 0 mm to 1.3 mm) show better agreement with the experimental data. Notably, the predicted temperatures at a depth of 3 mm exhibit very good agreement with the measured values, around 140 °C. Although the simulation still overpredicts the temperatures at depths of 6 mm and 9 mm closest to the flame, this discrepancy is considerably less pronounced than that seen in the temperatures farther from the flame.

Using the actual temperatures calculated at each corresponding node in the 1D discretisation, the complete in-depth temperature field ahead of the flame was deter-

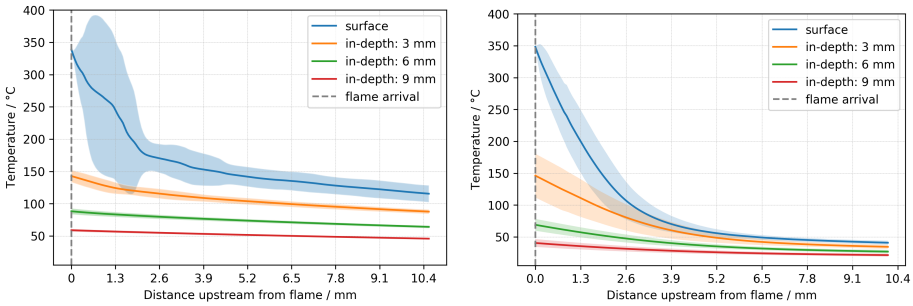

Figure 5.10: Comparison between the temperature profiles at the surface and within the solid ahead of the flame front. (a) Simulation results from the simulation case using 2 mm cells. (b) Experimental measurements (same as in Figure 5.5a).

mined. This calculation was performed not only for the 2.0 mm cell case but also for the other simulation cases employing different levels of refinement for the gas-phase grid. The resulting temperature fields are presented in Figure 5.11. It is worth noting that the distances upstream from the flame indicated on the x-axis vary slightly between plots.

The colour maps, all displayed on the same temperature scale, clearly illustrate an overall trend across the different grid resolutions: coarser grids lead to a greater overprediction of temperatures, both in-depth and at the surface. For instance, the coarsest cases with cell sizes of 2.0 mm and 2.6 mm predicted temperatures of approximately 60 °C and 90 °C respectively at a depth of 9 mm below the surface. In contrast, the experimental measurements, as presented in Figure 5.5b, indicated a temperature of 40 °C at this location. Clearly, the temperature predictions at this depth (9 mm) in the simulations employing the finest grid resolutions (particularly the 1.5 mm case) show the closest agreement with the experimental measurements.

This trend of temperature overprediction with coarser grids is particularly evident, and more pronounced, near the surface. For the finest grid resolution of 1.0 mm (Figure 5.11a), the surface temperature at the furthest upstream point shown (approximately 6.1 mm) is predicted to be around 80 °C. As the resolution becomes coarser, the predicted surface temperature at a comparable upstream distance increases steadily, rising to about 100 °C for the 1.5 mm case (Figure 5.11b), 130 °C for the 2.0 mm case (Figure 5.11c), and exceeding 140 °C in the coarsest grid of 2.6 mm (Figure 5.11d). This progression highlights that coarser simulations not only predict

higher temperatures deeper within the material, but also a more extensive preheating zone at the surface, extending further ahead of the flame front.

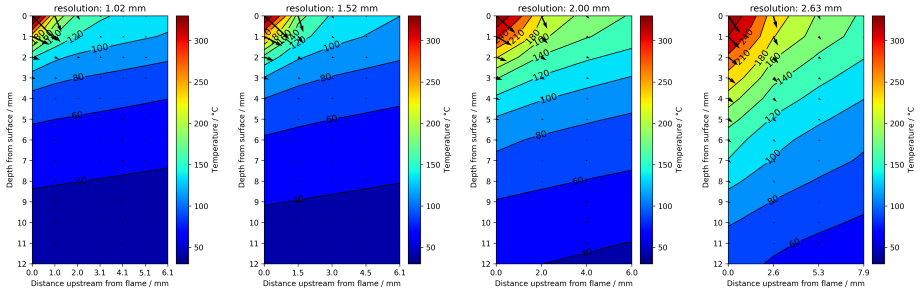

(a) (b) (c) (d)

Figure 5.11: Temperature distributions within the solid calculated for different gas-phase resolutions: (a) 1.0 mm (b) 1.5 mm (c) 2.0 mm (d) 2.6 mm. The longitudinal conductive transport does not actually exist in the model.

It is important to note that even though the isolines and thermal gradient arrows shown in Figure 5.11 assist with visualising the temperature distribution, they can be misleading from a physical viewpoint. This is because the gradient vectors were computed along both x and y directions, in the same way as for the experimental data analysis. However, the underlying heat conduction model used in the simulations assumes one-dimensional heat transfer, normal to the surface only, i.e., along y. There is no physical heat conduction along the sample in the x-direction. As a result, the computed vectors may give the false impression of multidimensional heat transport, which is not present in the actual model formulation.

To provide a more accurate graphical representation of the temperature distributions consistent with the limitations of the one-dimensional conduction model, the plots in Figure 5.11 were recalculated by considering only the temperature gradients in the direction normal to the surface. The resulting temperature fields are presented in Figure 5.12 for all simulation cases. In these plots, the one-dimensional spatial discretisation of the solid is visualised through the vertical 'columns' highlighted in the colour maps. These columns correspond to rows of nodes within the solid that are aligned with the gas-phase cells located immediately above the surface.

In addition, finer gas-phase cells tend to produce stronger surface heat fluxes, particularly near the flame front, as presented in Figure 5.13.

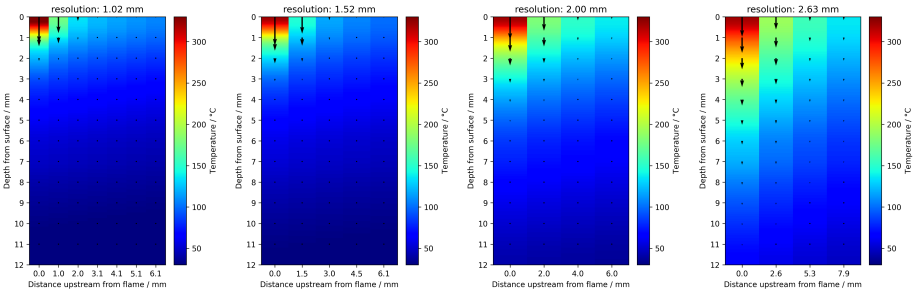

(a) (b) (c) (d)

Figure 5.12: Temperature distributions within the solid calculated for different gas-phase resolutions: (a) 1.0 mm (b) 1.5 mm (c) 2.0 mm (d) 2.6 mm.

Incoming heat fluxes

Figures 5.13a and 5.13b show respectively the radiative and convective heat fluxes incident on the solid surface ahead of the flame front, for all gas-phase resolutions. The heat fluxes correspond to the values at the solid surface, on the cells located adjacent to the columns shown in Figure 5.12. They are effectively incoming heat fluxes driving the heating within each row of nodes across the thickness of the sample. The markers along each curve reflect the spatial resolution used in each case, illustrating how the heat flux profiles are discretised according to the size of the gas-phase cells.

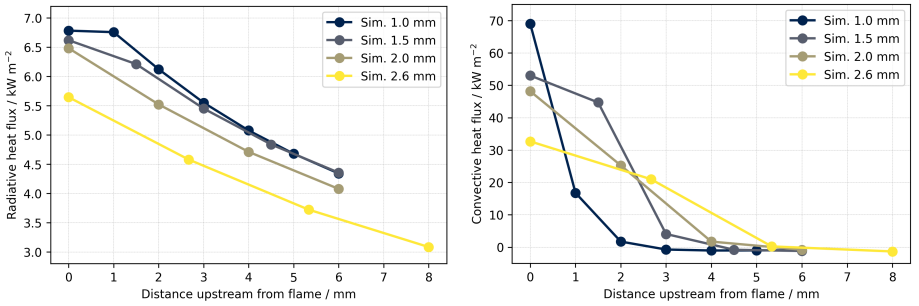

(a) (b)

Figure 5.13: Heat fluxes at the sample surface ahead of flame front, aligned with the rows of nodes in the solid shown in Figure 5.12, for different gas-phase resolutions. (a) Radiative heat flux. (b) Convective heat flux.

As can be seen from the plots in Figure 5.13, the heat fluxes at the surface, particularly the convective heat fluxes, increase significantly near the flame front as

the grid is refined. This behaviour is attributed to finer grids better resolving the temperature gradients near the flame leading edge. Figure 5.13b shows that the steep non-linear trend is best obtained when 1 mm cells are used. This observation results from the approach used to compute the convective heat flux, that includes an explicit dependence on the temperature gradients at the wall surface and on the cell sizes, as previously discussed.

It is also important to highlight the notably different contributions of the radiative and convective components to the total heat flux impinging on the sample surface near the flame. Note that the y axes in Figures 5.13a and 5.13b are scaled differently. While the peak radiative heat fluxes near the flame are in the range of $5.5\,\mathrm{kW\,m^{-2}}$ to $7.0\,\mathrm{kW\,m^{-2}}$, the convective fluxes reach considerably higher values, between $30\,\mathrm{kW\,m^{-2}}$ to $70\,\mathrm{kW\,m^{-2}}$. Furthermore, although both heat flux components increase with grid refinement, the rise in convective fluxes is significantly more pronounced. This indicates that it is primarily the convective heating that influences the energy input into the solid phase in the simulations and consequently dominates the pyrolysis rates and ROS predictions.

To determine which resolution yields the most accurate heat flux predictions, additional measurements capable of separating the radiative and convective fluxes of the total heat flux are needed. However, such measurements are challenging to perform experimentally and are typically subject to a high degree of uncertainty [Hodges et al., 2025]. Nonetheless, in flames of this scale, the primary heat transfer mechanism driving spread from the leading edge of the flame to the solid is generally attributed to gas-phase conduction, with radiation playing a secondary, though still relevant, role, particularly in preheating the material in horizontal configurations [Morrisset et al., 2024]. In the simulation model, gas-phase conduction is effectively represented as convective heat transfer. In this context, the smaller contribution of radiation and the dominant role of convection observed in the simulations are consistent with the expected hierarchy of heat transfer mechanisms in the actual flame.

This observation highlights the importance of addressing in future work the limitations related to the calculation of the convective heat transfer coefficient in FDS (Equation 2.14). As it stands, these limitations not only hinder proper grid convergence but also likely contribute to the overprediction of convective heat fluxes, as it was demonstrated that the most refined cases (1.5 mm and 1.0 mm) overpredicted the ROS values by 40 % to 100 %, respectively. Furthermore, since all heating within the solid originates from the gas-phase heat fluxes applied at the surface boundary, it is difficult to assess the plausibility of using the one-dimensional conduction model

to predict temperatures profiles within the solid without evaluating the heat fluxes reaching the material surface.

For this reason, the radiative and convective heat fluxes at the sample surface are shown in Figure 5.14 for all simulation cases. In this figure, the sub-figures on the left display radiative heat fluxes, while those on the right show the convective component. These images were obtained using the post-processing Python library `fdsreader` [Vogelsang and Arnold, 2023], and correspond to the moment when the flame front along the centreline reaches approximately 90 mm from the ignition edge. The flame is spreading from left to right. The purpose of showing these figures is to demonstrate how the shape of the flame front, reflected in the distribution of incoming heat fluxes, varies significantly with grid resolution.

In finer resolution cases, a concave flame front develops, with the leading edge curving inwards as a result of the faster flame spread along the edges of the sample than along its centreline. This behaviour contrasts with the convex shape observed in the experiments, where the leading edge curves outwards and the spread is faster along the centreline. This experimentally observed shape arises due to the water-cooled side boundaries, which locally remove heat via lateral conduction. A concave front could, in principle, appear in a real experiment if the sample edges were insulated, preventing lateral heat loss and favouring flame spread along the sides. In the simulations, however, this effect is most likely a combined effect between the one-dimensional heat conduction model and the increased convective heat fluxes. Since the conduction model neglects any lateral or longitudinal heat transfer, it is unable to redistribute the higher convective fluxes reaching the surface, which possibly leads to the observed distortion in the flame front.

5.4 Conclusions

The validation exercise presented in this chapter has revealed several important observations regarding the relationship between simulation predictions and experimental observations. In terms of ROS and in-depth temperature profiles, some predictions aligned well with the experimental data, while others showed clear deviations. The main remarks are outlined below:

Agreement in ROS does not guarantee accurate temperature predictions within the solid

Although the simulation using a 2.0 mm grid produced a ROS close to the experimental mean, the corresponding in-depth temperature profiles deviated significantly

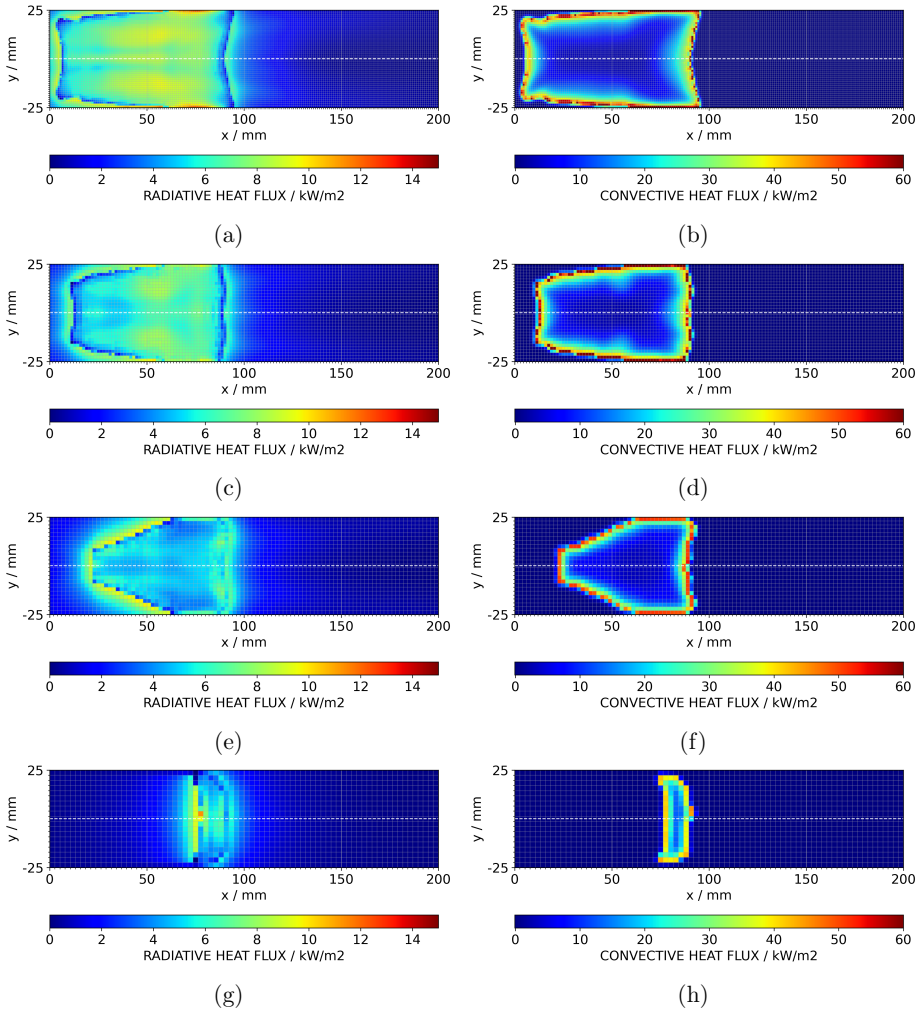

Figure 5.14: Heat flux intensities at the sample surface in the simulations using grid resolutions of: (a, b) 1.0 mm (c, d) 1.5 mm (e, f) 2.0 mm (g, h) 2.5 mm. Spread occurs from left to right.

from the measured data. Specifically, temperature predictions within the solid for the coarsest grid sizes of 2.0 mm and 2.6 mm were considerably higher than the experimental values, both near and ahead of the flame front.

On the other hand, simulations with finer grid resolutions (1.0 mm and 1.5 mm) produced temperature gradients in the near-flame region that more closely matched experimental observations. However, this improved agreement in the temperature

fields near the flame was accompanied by considerable overpredictions in the ROS, ranging from 40 % to 100 %.

Possible causes of discrepancies

The observed issues are likely due to a combined effect of two factors: the high sensitivity of convective heat flux calculations to the gas-phase grid resolution, and the limitations of the 1D heat conduction model. As the cell size decreases, convective fluxes increase substantially. However, the 1D conduction model is unable to dissipate these high incoming fluxes, which induce large temperature gradients in-depth over smaller discrete control volumes (nodes). This leads to enhanced pyrolysis and a higher ROS. Additionally, this effect may contribute to the formation of a concave flame front, where the flame spreads faster along the edges than at the centreline, unlike experimental observations.

The simulation cases represent only a simplified version of the flame spread experiments. A number of other modelling aspects, not explicitly addressed in this study, may still exert a non-negligible influence on both the predicted ROS and the temperature profiles. For instance, more consistent models should account for a more realistic representation of the experimental setup, such as incorporating the bench on which the sample holder rested, and capturing the actual flow conditions around the sample. However, the most critical sources of uncertainty are likely related to the parameter set used to describe PMMA pyrolysis, as well as assumptions and default settings that influence the calculation of radiative and convective heat fluxes.

The parameter set used in this work, developed by Fiola et al. [2021] and investigated in the previous chapter, was originally built for black cast PMMA. In contrast, the experiments discussed here were conducted using transparent cast PMMA samples. Prior studies by De Lannoye et al. [2023] have indicated that PMMA colour can influence measured HRRs, raising concerns about the suitability of this parameter set in representing the actual material behaviour. Moreover, the previous analysis in Chapter 4 highlighted that even small features in the mass loss rate curve can significantly affect flame spread predictions when using FDS with the MaCFP parameter set [Quaresma et al., 2025], which is the modelling approach adopted in this study. Therefore, future work should focus on investigating the effects of material properties that define the solid, as the properties of the PMMA used here may not reflect those of the actual sample tested.

Chapter 6

Closing Remarks

6.1 General conclusions

In this chapter, the most important conclusions drawn from the investigations conducted in the scope of this thesis are summarised and highlighted.

Parameter transferability

In Chapter 3, the sensitivity analysis results showed that the model representing the bench-scale experiment used in inverse modelling may not be sufficiently sensitive to all the parameters that are important to the flame spread simulation. Moreover, the sensitivities of the optimised model to the input parameters of interest were found to vary over the course of the simulation. An effective parameter estimation strategy should therefore include cost functions designed to capture distinct phases of the experimental response, ensuring that important parameters with time-varying sensitivities are not overlooked.

Despite these improvements, several parameters relevant to the flame spread simulation may still remain practically uninfluential to the optimised model based on standard bench scale experiments. This limitation suggests that more representative experimental setups, such as bench-scale flame spread experiments, could be used for parameter estimation, where the spread rates becomes a direct optimisation target.

Required fit accuracy

The study presented in Chapter 4 demonstrated that accounting for a small MLR peak in the scheme of pyrolysis reactions can significantly impact simulation predictions. The small MLR peaks are commonly observed in TGA data and are often neglected when modelling reaction rates. Sensitivity analyses showed that small peaks

occurring at lower temperatures within the pyrolysis range of the material can increase ROS predictions, in some cases by more than ten percent, depending on the associated mass loss.

The acceptability of such variations depends on the specific modelling objectives and the level of uncertainty considered tolerable, which should ideally be evaluated against experimental flame spread data. These findings highlight the importance of accurately characterising small features in TGA data and suggest that even minor peaks may play a non-negligible role in simulation predictions of interest, such as spread rates.

In a more general perspective, this initial step toward understanding the role of small MLR peaks contributes to ongoing discussions on experimental variability in TGA measurements. If small variations do influence ROS predictions, then a systematic quantification of their impact could help define the level of accuracy and precision required in TGA data for reliable use in fire modelling.

Validation

Chapter 5 showed that accurate ROS prediction does not necessarily imply accurate simulation of in-depth temperature profiles. Although one of the coarsest tested grid resolutions reproduced the ROS reasonably well, it significantly overestimated temperatures within the solid. In contrast, finer grids led to better agreement with measured temperatures near the flame front but substantially overpredicted the ROS. These discrepancies are likely due to the strong sensitivity of convective heat flux to gas-phase grid resolution, combined with limitations of the 1D heat conduction model.

Several other factors might also contribute to the discrepancies between simulation and experiment. However, the most critical sources of uncertainty are likely related to the utilised set of material parameters, which was originally derived for black PMMA, whereas the experiments were conducted with transparent samples. Additional uncertainties arise from underlying assumptions and simulation settings affecting both the radiative and convective heat flux calculations.

6.2 Outlook

The sensitivity analysis results presented throughout this work help clarify the overall behaviour of the simulation models, capturing the interactions among the various submodels within FDS. Both the models and the material parameter sets investigated

reflect current state-of-the-art practices in the fire research community for predicting flame spread based on material pyrolysis. To derive more general conclusions, future work should aim to extend the analyses presented here, particularly along the following lines:

- Extend the sensitivity analysis on the simplified cone calorimeter simulation to additional heat fluxes and materials, to assess whether the time-dependent sensitivities to input parameters observed here are consistent across these different configurations.
- Validate the flame spread simulations, whose sensitivities were compared against those of the cone calorimeter, using flame spread experiments conducted with the same material as that used to derive the investigated parameter set, ensuring full consistency in the evaluation of parameter performance across setups.
- Build a complete material property set for the transparent PMMA samples used in the validation experiments, or at least recalibrate the applied pyrolysis scheme based on TGA data. Given the demonstrated influence of small MLR peaks on ROS predictions, this step is essential to reduce uncertainty and improve simulation fidelity.
- Consider integrating the beta 3D heat conduction model available in FDS, along with fixed convective heat transfer coefficients and adjustments to gas-phase model settings, to address limitations of the 1D conduction approach and explore impacts on the accuracy of simulation predictions, such as spread rates and temperature profiles within the solid.
- Investigate the potential of using small-scale flame spread experiments, such as the one conducted in this work, and the corresponding simulation models, as a basis for material property estimation. These setups may capture flame spread behaviour more realistically than some of the standard bench-scale experiments, which typically do not involve actual spread, like the cone calorimeter.

Appendix A

Simplified cone calorimeter simulation

A.1 Input parameters not included in the sensitivity analysis

Table A.1: Reference temperature (T_p), pyrolysis range (ΔT) and heat of reaction (ΔH_R) defining eight overlapping peaks in the DTG data of PMMA for a heating rate of $60\,\mathrm{K\,min^{-1}}$. The kinetic parameters are calculated by FDS from T_p, ΔT and the heating rate [Hehnen and Arnold, 2023].

Reaction label	T_p / °C	ΔT / °C	ΔH_R / $\mathrm{kJ\,kg^{-1}}$	A / $\mathrm{s^{-1}}$	E / $\mathrm{J\,mol^{-1}}$
PMMA1	381.3	120.7	10.4	2.08E+11	1.59E+05
PMMA2	408.4	86.	10.1	2.12E+17	2.42E+05
PMMA3	428.3	90.4	1838.5	8.14E+16	2.44E+05
PMMA4	310.7	180.	1619.7	1.52E+06	8.47E+04
PMMA5	300.8	75.9	1739.1	3.32E+16	1.94E+05
PMMA6	216.2	70.4	1254.	1.38E+15	1.52E+05
PMMA7	187.3	73.3	1157.4	3.51E+13	1.29E+05
PMMA8	196.9	250.	758.2	5.33E+02	3.95E+04

A.2 Material definition in the FDS input file

```
&MATL ID                     = 'PMMA1'
      EMISSIVITY             = 0.9405141386485816
      ABSORPTION_COEFFICIENT = 7978.755855654813,
      REFRACTIVE_INDEX       = 2.8539019657069407,
      SPECIFIC_HEAT_RAMP     = 'PMMA_spec_heat_ramp'
      CONDUCTIVITY_RAMP      = 'PMMA_conductivity_ramp'
```

```
      DENSITY                = 1201.722222222222
      N_REACTIONS            = 1
      REFERENCE_TEMPERATURE  = 381.3443746649532
      PYROLYSIS_RANGE        = 120.7440564865074
      HEATING_RATE           = 60
      SPEC_ID                = 'FuelMixture'
      NU_SPEC                = 0.9899044759798044
      MATL_ID                = 'PMMA Aalto Residue'
      NU_MATL                = 0.010095524020195633
      HEAT_OF_REACTION       = 10.385814949691056 /

&MATL ID                     = 'PMMA2'
      EMISSIVITY             = 0.9405141386485816
      ABSORPTION_COEFFICIENT = 7978.755855654813,
      REFRACTIVE_INDEX       = 2.8539019657069407,
      SPECIFIC_HEAT_RAMP     = 'PMMA_spec_heat_ramp'
      CONDUCTIVITY_RAMP      = 'PMMA_conductivity_ramp'
      DENSITY                = 1201.722222222222
      N_REACTIONS            = 1
      REFERENCE_TEMPERATURE  = 408.3883709946584
      PYROLYSIS_RANGE        = 85.96187121041275
      HEATING_RATE           = 60
      SPEC_ID                = 'FuelMixture'
      NU_SPEC                = 0.9899044759798044
      MATL_ID                = 'PMMA Aalto Residue'
      NU_MATL                = 0.010095524020195633
      HEAT_OF_REACTION       = 10.128169644595395 /

&MATL ID                     = 'PMMA3'
      EMISSIVITY             = 0.9405141386485816
      ABSORPTION_COEFFICIENT = 7978.755855654813,
      REFRACTIVE_INDEX       = 2.8539019657069407,
      SPECIFIC_HEAT_RAMP     = 'PMMA_spec_heat_ramp'
      CONDUCTIVITY_RAMP      = 'PMMA_conductivity_ramp'
      DENSITY                = 1201.722222222222
      N_REACTIONS            = 1
      REFERENCE_TEMPERATURE  = 428.2540035507077
      PYROLYSIS_RANGE        = 90.39252489068386
      HEATING_RATE           = 60
      SPEC_ID                = 'FuelMixture'
      NU_SPEC                = 0.9899044759798044
      MATL_ID                = 'PMMA Aalto Residue'
      NU_MATL                = 0.010095524020195633
      HEAT_OF_REACTION       = 1838.460303474519 /

&MATL ID                     = 'PMMA4'
      EMISSIVITY             = 0.9405141386485816
      ABSORPTION_COEFFICIENT = 7978.755855654813,
      REFRACTIVE_INDEX       = 2.8539019657069407,
      SPECIFIC_HEAT_RAMP     = 'PMMA_spec_heat_ramp'
      CONDUCTIVITY_RAMP      = 'PMMA_conductivity_ramp'
      DENSITY                = 1201.722222222222
      N_REACTIONS            = 1
      REFERENCE_TEMPERATURE  = 310.72655174589727
      PYROLYSIS_RANGE        = 179.99298498463392
      HEATING_RATE           = 80
      SPEC_ID                = 'FuelMixture'
      NU_SPEC                = 0.9899044759798044
      MATL_ID                = 'PMMA Aalto Residue'
```

```
      NU_MATL                = 0.010095524020195633
      HEAT_OF_REACTION       = 1619.717271736553 /

&MATL ID                     = 'PMMA5'
      EMISSIVITY             = 0.9405141386485816
      ABSORPTION_COEFFICIENT = 7978.755855654813,
      REFRACTIVE_INDEX       = 2.8539019657069407,
      SPECIFIC_HEAT_RAMP     = 'PMMA_spec_heat_ramp'
      CONDUCTIVITY_RAMP      = 'PMMA_conductivity_ramp'
      DENSITY                = 1201.722222222222
      N_REACTIONS            = 1
      REFERENCE_TEMPERATURE  = 300.77205541725533
      PYROLYSIS_RANGE        = 75.91045441968164
      HEATING_RATE           = 60
      SPEC_ID                = 'FuelMixture'
      NU_SPEC                = 0.9899044759798044
      MATL_ID                = 'PMMA Aalto Residue'
      NU_MATL                = 0.010095524020195633
      HEAT_OF_REACTION       = 1739.082687477869 /

&MATL ID                     = 'PMMA6'
      EMISSIVITY             = 0.9405141386485816
      ABSORPTION_COEFFICIENT = 7978.755855654813,
      REFRACTIVE_INDEX       = 2.8539019657069407,
      SPECIFIC_HEAT_RAMP     = 'PMMA_spec_heat_ramp'
      CONDUCTIVITY_RAMP      = 'PMMA_conductivity_ramp'
      DENSITY                = 1201.722222222222
      N_REACTIONS            = 1
      REFERENCE_TEMPERATURE  = 216.2488285365476
      PYROLYSIS_RANGE        = 70.36922700264373
      HEATING_RATE           = 60
      SPEC_ID                = 'FuelMixture'
      NU_SPEC                = 0.9899044759798044
      MATL_ID                = 'PMMA Aalto Residue'
      NU_MATL                = 0.010095524020195633
      HEAT_OF_REACTION       = 1253.973471989791 /

&MATL ID                     = 'PMMA7'
      EMISSIVITY             = 0.9405141386485816
      ABSORPTION_COEFFICIENT = 7978.755855654813,
      REFRACTIVE_INDEX       = 2.8539019657069407,
      SPECIFIC_HEAT_RAMP     = 'PMMA_spec_heat_ramp'
      CONDUCTIVITY_RAMP      = 'PMMA_conductivity_ramp'
      DENSITY                = 1201.722222222222
      N_REACTIONS            = 1
      REFERENCE_TEMPERATURE  = 187.2523577480169
      PYROLYSIS_RANGE        = 73.30255706364409
      HEATING_RATE           = 60
      SPEC_ID                = 'FuelMixture'
      NU_SPEC                = 0.9899044759798044
      MATL_ID                = 'PMMA Aalto Residue'
      NU_MATL                = 0.010095524020195633
      HEAT_OF_REACTION       = 1157.3723612048998 /

&MATL ID                     = 'PMMA8'
      EMISSIVITY             = 0.9405141386485816
      ABSORPTION_COEFFICIENT = 7978.755855654813,
      REFRACTIVE_INDEX       = 2.8539019657069407,
      SPECIFIC_HEAT_RAMP     = 'PMMA_spec_heat_ramp'
```

```
      CONDUCTIVITY_RAMP      = 'PMMA_conductivity_ramp'
      DENSITY                = 1201.722222222222
      N_REACTIONS            = 1
      REFERENCE_TEMPERATURE  = 196.85774116536888
      PYROLYSIS_RANGE        = 249.99573096502849
      HEATING_RATE           = 60
      SPEC_ID                = 'FuelMixture'
      NU_SPEC                = 0.9899044759798044
      MATL_ID                = 'PMMA Aalto Residue'
      NU_MATL                = 0.010095524020195633
      HEAT_OF_REACTION       = 758.2134448829147 /

&MATL ID             = 'PMMA Aalto Residue'
      EMISSIVITY     =  0.5520057564788229,
      DENSITY        =  2500.0,
      CONDUCTIVITY   =  4.50919688424257,
      SPECIFIC_HEAT  =  5.892803062316541/

&RAMP ID='PMMA_spec_heat_ramp',
      T=150., F=0.7741648038839803 /
&RAMP ID='PMMA_spec_heat_ramp',
      T=480., F=3.808281524548285 /
&RAMP ID='PMMA_spec_heat_ramp',
      T=800., F=7.274640529337403 /

&RAMP ID='PMMA_conductivity_ramp',
      T=150., F=0.3788915344192658 /
&RAMP ID='PMMA_conductivity_ramp',
      T=480., F=0.0242847106346628 /
&RAMP ID='PMMA_conductivity_ramp',
      T=800., F=4.337110594860761 /

&MATL ID             = 'Backing'
      EMISSIVITY     =  0.4406532690587335,
      DENSITY        =  65.0,
      CONDUCTIVITY   =  2.407783433840767,
      SPECIFIC_HEAT  =  4.066725085995637/
```

A.3 Sensitivities across different gas-phase grid resolutions

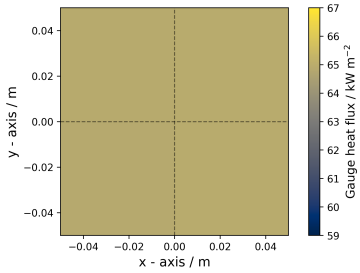

(a) C2

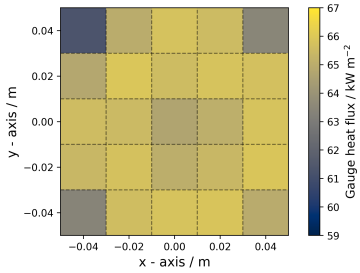

(b) C5

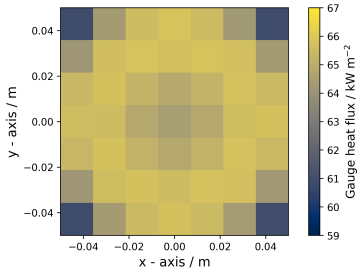

(c) C7

Figure A.1: Heat flux maps applied on the sample of the simplified cone calorimeter simulation for different gas-phase grid resolutions.

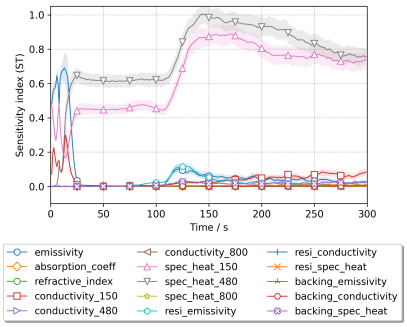

(a) C2

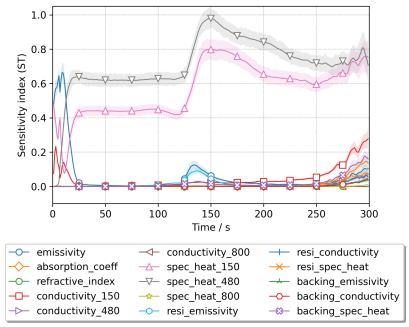

(b) C5

Figure A.2: Total-order indices (ST) calculated based on the simulated HRRs.

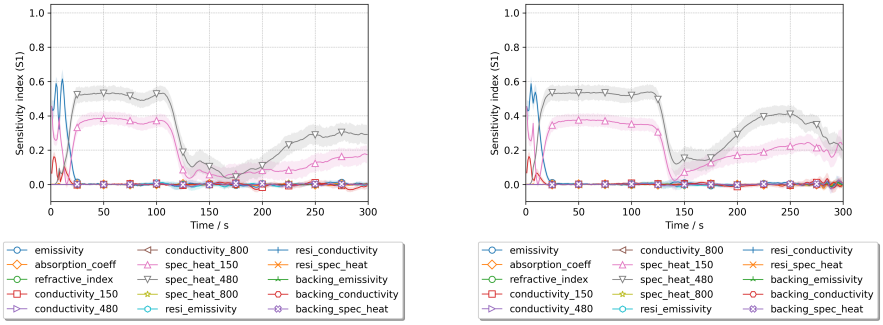

(a) C2 (b) C5

Figure A.3: First-order indices (S1) calculated based on the simulated HRRs.

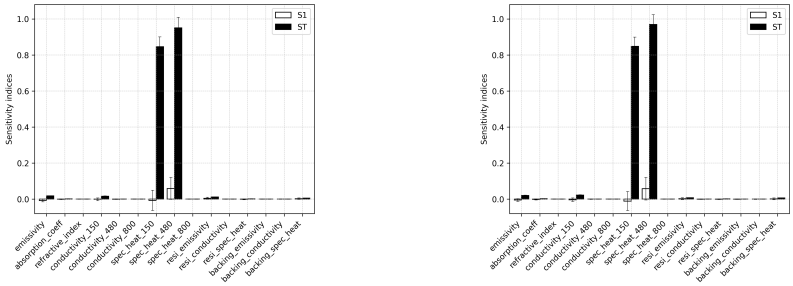

(a) C2 (b) C5

Figure A.4: Sensitivity indices (ST and S1) expressing the effects of input parameters on the global RMSE, calculated between the simulated HRRs and the target experimental data.

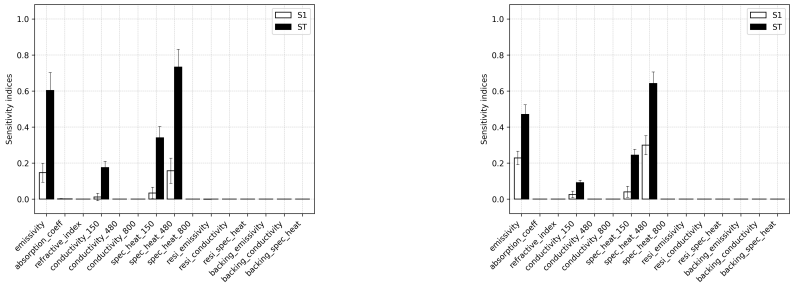

(a) C2 (b) C5

Figure A.5: Sensitivity indices expressing the effects of input parameters on the partial RMSE, calculated between the simulated HRRs and the target experimental data in the initial 20 seconds.

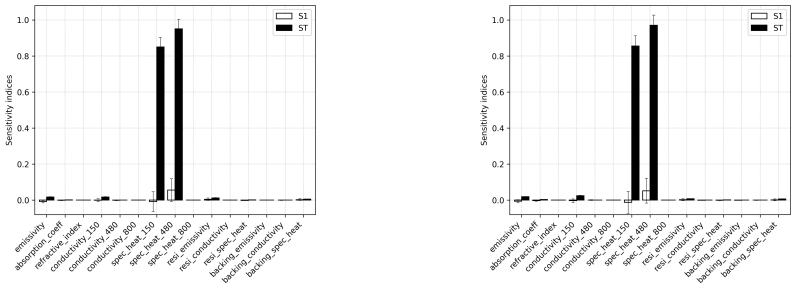

(a) C2 (b) C5

Figure A.6: Sensitivity indices expressing the effects of input parameters on the partial RMSE, calculated between the simulated HRRs and the target experimental data in the interval of 20 s to 300 s.

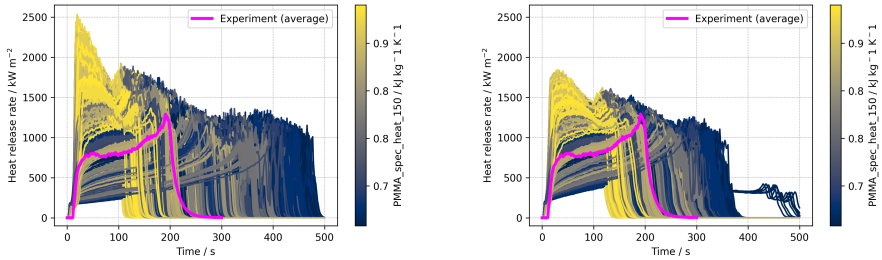

(a) C2 (b) C5

Figure A.7: Simulated HRRs coloured by the specific heat at 150 °C values used in each simulation.

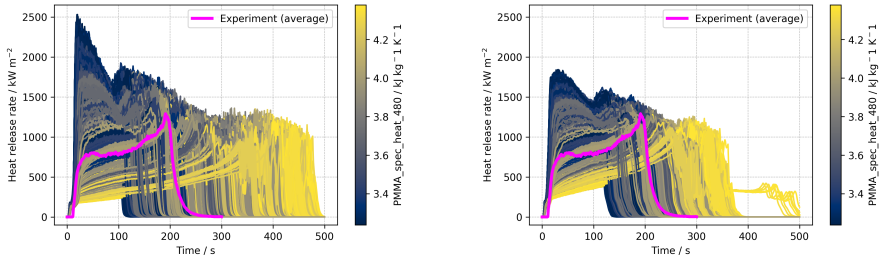

(a) C2 (b) C5

Figure A.8: Simulated HRRs coloured by the specific heat at 480 °C values used in each simulation.

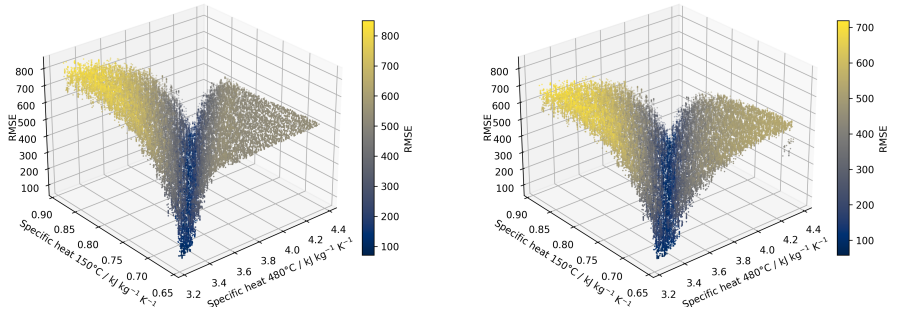

(a) C2 (b) C5

Figure A.9: Values of RMSE plotted against its two most influential parameters.

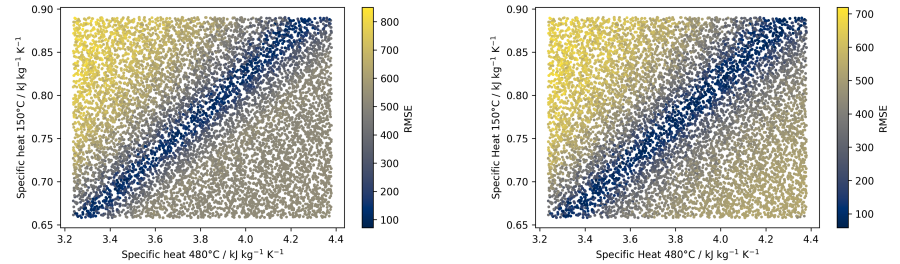

(a) C2 (b) C5

Figure A.10: Values of RMSE plotted against its two most influential parameters, 2D projection.

A.4 Effect of sample size on Sobol indices estimations

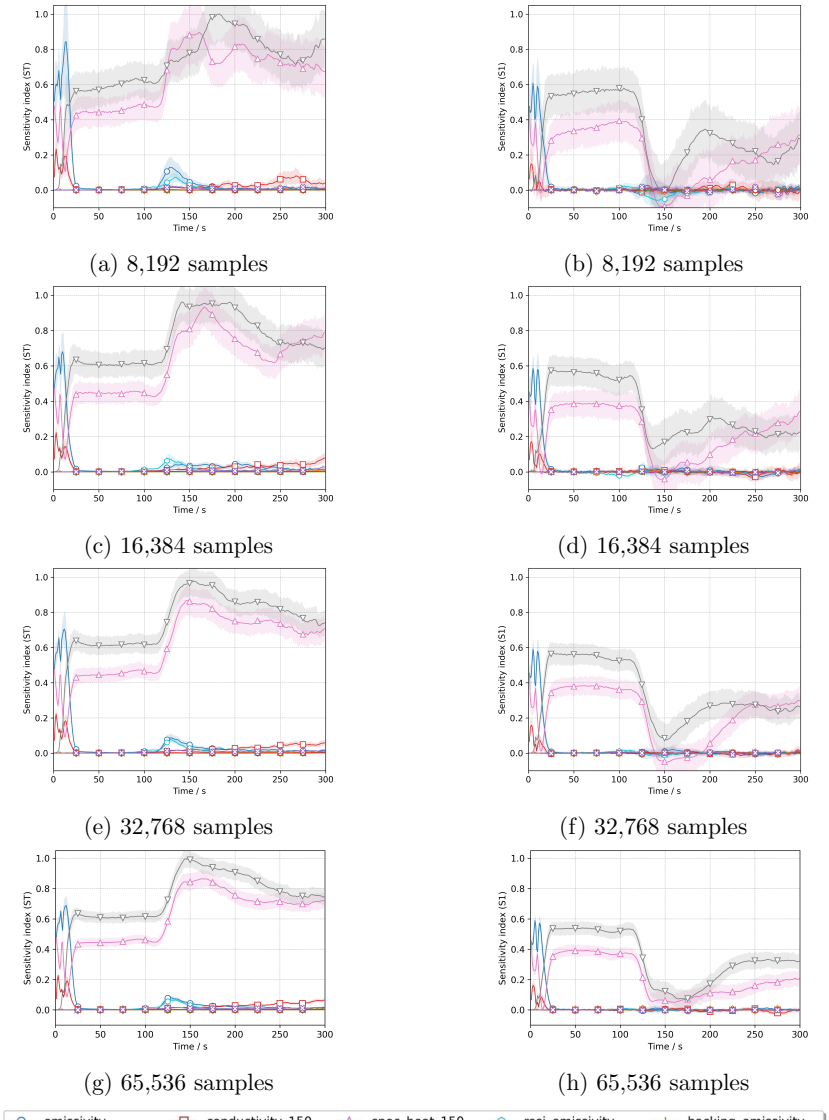

(a) 8,192 samples (b) 8,192 samples

(c) 16,384 samples (d) 16,384 samples

(e) 32,768 samples (f) 32,768 samples

(g) 65,536 samples (h) 65,536 samples

Figure A.11: Sobol indices estimated considering different sample sizes.

References

Arrhenius, S. (1889). Über die Reaktionsgeschwindigkeit bei der Inversion von Rohrzucker durch Säuren. *Zeitschrift für physikalische Chemie*, 4(1):226–248.

Arrhenius, S. (1967). On the reaction velocity of the inversion of cane sugar by acids. In *Selected readings in chemical kinetics*, pages 31–35. Elsevier.

Assael, M., Botsios, S., Gialou, K., and Metaxa, I. (2005). Thermal conductivity of polymethyl methacrylate (pmma) and borosilicate crown glass bk7. *International Journal of Thermophysics*, 26:1595–1605.

Babrauskas, V. (1982). Development of the cone calorimeter, a bench scale heat release rate apparatus based on oxygen consumption. *NASA STI/Recon Technical Report N*, 83:29673.

Babrauskas, V. (2016). *The Cone Calorimeter*, pages 952–980. Springer New York, New York, NY.

Bal, N. and Rein, G. (2011). Numerical investigation of the ignition delay time of a translucent solid at high radiant heat fluxes, `https://doi.org/10.1016/j.combustflame.2010.10.014`. *Combustion and Flame*, 158(6):1109–1116.

Bal, N. and Rein, G. (2015). On the effect of inverse modelling and compensation effects in computational pyrolysis for fire scenarios, `https://doi.org/10.1016/j.firesaf.2015.02.012`. *Fire safety journal*, 72:68–76.

Batiot, B., Rogaume, T., Collin, A., Richard, F., and Luche, J. (2016). Sensitivity and uncertainty analysis of Arrhenius parameters in order to describe the kinetic of solid thermal degradation during fire phenomena, `http://dx.doi.org/10.1016/j.firesaf.2016.03.007`. *Fire Safety Journal*, 82:76–90.

Beji, T. and Merci, B. (2019). Numerical simulations of a full-scale cable tray fire using small-scale test data, `https://doi.org/10.1002/fam.2687`. *Fire and Materials*, 43(5):486–496.

Bird, R. B. (2002). Transport phenomena. *Appl. Mech. Rev.*, 55(1):R1–R4.

Bolshova, T. A., Gerasimov, I. E., Shmakov, A. G., and Korobeinichev, O. P. (2023). Combustion of spherical PMMA samples in still air simulated using a skeletal chemical kinetic mechanism, `https://doi.org/10.1016/j.firesaf.2023.103807`. *Fire Safety Journal*, 138:103807.

Boulet, P., Gerardin, J., Acem, Z., Parent, G., Collin, A., Pizzo, Y., and Porterie, B. (2014). Optical and radiative properties of clear pmma samples exposed to a radiant heat flux. *International Journal of Thermal Sciences*, 82:1–8.

Burnford, J., Morrisset, D., Ojo, A. O., Hadden, R. M., Law, A., and Peterson, B. (2024). Assessment and application of phosphor thermometry for spatially resolved surface temperature measurements during downward flame spread, `https://doi.org/10.1016/j.fuel.2024.131201`. *Fuel*, 365:131201.

Chaos, M. (2013). Application of sensitivity analysis in condensed-phase pyrolysis modeling. *Fire Safety Journal*, 58:202–210, doi:10.1016/j.firesaf.2013.02.006.

Chaos, M., Khan, M. M., Krishnamoorthy, N., De Ris, J. L., and Dorofeev, S. B. (2011). Evaluation of optimization schemes and determination of solid fuel properties for cfd fire models using bench-scale pyrolysis tests. *Proceedings of the Combustion Institute*, 33(2):2599–2606.

Chaudhari, D. M., Fiola, G. J., and Stoliarov, S. I. (2021). Experimental analysis and modeling of Buoyancy-driven flame spread on cast poly (methyl methacrylate) in corner configuration, `https://doi.org/10.1016/j.polymdegradstab.2020.109433`. *Polymer Degradation and Stability*, 183:109433.

Chaudhari, D. M. and Stoliarov, S. I. (2022). Analysis of sensitivity of vertical corner flame spread dynamics to uncertainties in the model input. In *The 10th International Seminar on Fire and Explosion Hazards*, volume 22.

Coats, A. W. and Redfern, J. P. (1963). Thermogravimetric analysis. A review. *Analyst*, 88:906–924, doi:10.1039/AN9638800906.

De Lannoye, K., Belt, A., Reinecke, E.-A., Markert, F., and Arnold, L. (2023). Comparison of black and transparent pmma in the cone calorimeter. *Obtaining Data for Fire Growth Models*, pages 150–160.

De Lannoye, K., Trettin, C., Belt, A., Reinecke, E., Goertz, R., and Arnold, L. (2024). The influence of experimental conditions on the mass loss for TGA in fire safety science, https://doi.org/10.1016/j.firesaf.2023.104079. *Fire Safety Journal*, 144:104079.

Dehghani, P., Chaudhari, D. M., DiDomizio, M. J., and Floyd, J. E. (2025). Toward grid-independent modeling of natural convection with fire dynamics simulator. *International Journal of Heat and Mass Transfer*, 250:127190.

DiDomizio, M. and McKinnon, M. (2023). Impact of specimen preparation method on thermal analysis testing and derived parameters, https://doi.org/10.1520/STP164220210106. In *Symposium on Obtaining Data for Fire Growth Models*, pages 64–87. ASTM International.

DiDomizio, M. J., McKinnon, M. B., and Bellamy, G. (2024). Measurement of thermal conductivity of thermally reactive materials for use in pyrolysis models. *Fire and Materials*, 48(8):796–810.

Ding, Y., Leventon, I. T., and Stoliarov, S. I. (2023). An analysis of the sensitivity of the rate of buoyancy-driven flame spread on a solid material to uncertainties in the pyrolysis and combustion properties. Is accurate prediction possible?, https://doi.org/10.1016/j.polymdegradstab.2023.110405. *Polymer Degradation and Stability*, 214:110405.

Drysdale, D. (2011). *An introduction to fire dynamics*. John wiley & sons.

Feinberg, J. and Langtangen, H. P. (2015). Chaospy: An open source tool for designing methods of uncertainty quantification, http://dx.doi.org/10.1016/j.jocs.2015.08.008. *Journal of Computational Science*, 11:46–57.

Ferriol, M., Gentilhomme, A., Cochez, M., Oget, N., and Mieloszynski, J. (2003). Thermal degradation of poly (methyl methacrylate)(PMMA): modelling of DTG and TG curves, https://doi.org/10.1016/S0141-3910(02)00291-4. *Polymer degradation and stability*, 79(2):271–281.

Fiola, G. J., Chaudhari, D. M., and Stoliarov, S. I. (2021). Comparison of pyrolysis properties of extruded and cast poly (methyl methacrylate), https://doi.org/10.1016/j.firesaf.2020.103083. *Fire safety journal*, 120:103083.

Fleurotte, M., Authier, O., Bourbigot, S., Fontaine, G., Debenest, G., and Amokrane, A. (2022). Sensitivity analysis applied to the pyrolysis of charring and non-charring materials under a cone calorimeter, https://doi.org/10.1177/07349041221134486. *Journal of Fire Sciences*, 40(6):405–443.

Flynn, D. R., Zarr, R. R., Hahn, M. H., and Healy, W. M. (2002). Design concepts for a new guarded hot plate apparatus for use over an extended temperature range. *ASTM SPECIAL TECHNICAL PUBLICATION*, 1426:97–114.

for Standardization (ISO), T. I. O. (2015). Part 1: Heat release rate (cone calorimeter method) and smoke production rate (dynamic measurement). Standard, International Organization for Standardization, Geneva, CH.

Grosshandler, W. L. (1993). Radcal: A narrow band model for radiation. *Calculations in a Combustion Environment, NIST Technical Note*, 1402.

Hammerschmidt, U., Hameury, J., Strnad, R., Turzó-Andras, E., and Wu, J. (2015). Critical review of industrial techniques for thermal-conductivity measurements of thermal insulation materials. *International journal of thermophysics*, 36:1530–1544.

Hasburgh, L. E. and Boardman, C. R. (2023). *Measuring the Specific Heat Capacity of Wood during Pyrolysis*, page 88–96. ASTM International100 Barr Harbor Drive, PO Box C700, West Conshohocken, PA 19428-2959.

Hehnen, T. and Arnold, L. (2023). PMMA Pyrolysis Simulation – from Micro- to Real-Scale, https://doi.org/10.1016/j.firesaf.2023.103926. *Fire Safety Journal*, 141:103926.

Hehnen, T., Arnold, L., and La Mendola, S. (2020). Numerical Fire Spread Simulation Based on Material Pyrolysis—An Application to the CHRISTIFIRE Phase 1 Horizontal Cable Tray Tests, https://doi.org/10.3390/fire3030033. *Fire*, 3(3):33.

Hehnen, T., Arnold, L., Van Hees, P., and La Mendola, S. (2018). Simulation of fire propagation in cable tray installations for particle accelerator facility tunnels. In *Proceedings of the 8th International Symposium on Tunnel Safety and Security ISTSS*.

Herman, J. and Usher, W. (2017). SALib: An open-source Python library for Sensitivity Analysis, https://doi.org/10.21105/joss.00097. *The Journal of Open Source Software*, 2(9).

Hirata, T., Kashiwagi, T., and Brown, J. E. (1985). Thermal and oxidative degradation of poly (methyl methacrylate): weight loss https://doi.org/10.1021/ma00149a010. *Macromolecules*, 18(7):1410–1418.

Hodges, J. L., Floyd, J. E., and DiDomizio, M. J. (2025). Separation of heat transfer modes in fire: Review and analysis, https://doi.org/10.1016/j.firesaf.2025.104353. *Fire Safety Journal*, page 104353.

Holland, B. and Hay, J. (2002). The effect of polymerisation conditions on the kinetics and mechanisms of thermal degradation of PMMA, https://doi.org/10.1016/S0141-3910(02)00100-3. *Polymer degradation and stability*, 77(3):435–439.

Howell, J. R., Mengüç, M. P., Daun, K., and Siegel, R. (2020). *Thermal radiation heat transfer*. CRC press.

Hurley, M. J., Gottuk, D. T., Hall Jr, J. R., Harada, K., Kuligowski, E. D., Puchovsky, M., Watts Jr, J. M., WIECZOREK, C. J., et al. (2015). *SFPE handbook of fire protection engineering*. Springer.

Iwanaga, T., Usher, W., and Herman, J. (2022). Toward SALib 2.0: Advancing the accessibility and interpretability of global sensitivity analyses, https://sesmo.org/article/view/18155. *Socio-Environmental Systems Modelling*, 4:18155.

Jamil, H. and Brännström, F. (2024). Intrusive and non-intrusive uncertainty quantification methodologies for pyrolysis modeling, https://doi.org/10.1016/j.firesaf.2023.104060. *Fire Safety Journal*, 143:104060.

Jiang, L., Miller, C. H., Gollner, M. J., and Sun, J. (2017). Sample width and thickness effects on horizontal flame spread over a thin PMMA surface, https://doi.org/10.1016/j.proci.2016.06.157. *Proceedings of the Combustion Institute*, 36(2):2987–2994.

Kashiwagi, T., Inaba, A., Brown, J. E., Hatada, K., Kitayama, T., and Masuda, E. (1986). Effects of weak linkages on the thermal and oxidative degradation of poly (methyl methacrylates) https://doi.org/10.1021/ma00162a010. *Macromolecules*, 19(8):2160–2168.

Kim, E. and Dembsey, N. (2015). Parameter estimation for comprehensive pyrolysis modeling: guidance and critical observations, http://doi.org/10.1007/s10694-014-0399-0. *Fire Technology*, 51(2):443–477.

Korobeinichev, O., Gonchikzhapov, M., Tereshchenko, A., Gerasimov, I., Shmakov, A., Paletsky, A., and Karpov, A. (2018). An experimental study of horizontal flame spread over PMMA surface in still air, https://doi.org/10.1016/j.combustflame.2017.10.008. *Combustion and flame*, 188:388–398.

L., C., Stoliarov, S., Lord, J., and Leventon, I. (2018). A methodology for predicting and comparing the full-scale fire performance of similar materials based on small-scale testing. *Fire and Materials*, 42(7):710–724.

Laidler, K. J. (1984). The development of the Arrhenius equation. *Journal of chemical Education*, 61(6):494.

Laidler, K. J. and King, M. C. (1983). The development of transition-state theory. *J. phys. Chem*, 87(15):2657–2664.

Lauer, P., Arnold, L., and Brännström, F. (2023). Inverse modelling of pyrolization kinetics with ensemble learning methods, https://doi.org/10.1016/j.firesaf.2023.103744. *Fire Safety Journal*, 136:103744.

Lauer, P., Hehnen, T., Brännström, F., Arnold, L., Trettin, C., and Lannoye, K. D. (26 February 2021). Pyrolysis Model Data Set Contribution for the Macfp Workshop April 2021 - Dataset, https://doi.org/10.5281/zenodo.470457. *Zenodo*.

Lauer, P., Hehnen, T., Trettin, C., Brännström, F., and Arnold, L. (2020). Role of the Cost Function for Material Parameter Estimation, https://doi.org/10.5281/zenodo.4007595. In *Fire and Evacuation Modelling Technical Conference*.

Lauer, P., Trettin, C., Wittbecker, F.-W., and Arnold, L. (2016). Performance of optimization algorithms for deriving material data from bench scale tests. In *Fire and Evacuation Modelling Technical Conference*, volume 2016.

Lautenberger, C. and Fernandez-Pello, C. (2009). Generalized pyrolysis model for combustible solids. *Fire safety journal*, 44(6):819–839.

Lautenberger, C. and Fernandez-Pello, C. (2011). Optimization algorithms for material pyrolysis property estimation. *Fire Safety Science*, 10(3):459–470.

Lautenberger, C., Rein, G., and Fernandez-Pello, C. (2006). The application of a genetic algorithm to estimate material properties for fire modeling from bench-scale fire test data. *Fire safety journal*, 41(3):204–214.

Leventon, I., Batiot, B., Bruns, M., Hostikka, S., Nakamura, Y., Reszka, P., Rogaume, T., and Stoliarov, S. (2022). Measurement and Computation of Fire Phenomena (MaCFP) Condensed Phase Material Database. github.com/MaCFP/macfp-db, Commit: 7f89fd8, DOI: https://doi.org/10.18434/mds2-2586.

Leventon, I., Batiot, B., Bruns, M., Hostikka, S., Nakamura, Y., Reszka, P., Rogaume, T., and Stoliarov, S. (2023). Measurement and Computation of Fire Phenomena (MaCFP) - Condensed Phase Material Database (MATL-DB). https://github.com/MaCFP/matl-db/tree/master/PMMA/Material_Properties, Commit: 2393d51.

Leventon, I., Heck, M., McGrattan, K. B., Bundy, M., and Davis, R. D. (2024). The Impact of Material Composition on Ignitability and Fire Growth. Volume 1: Full-Scale Burning Behavior of Combustible Solids Commonly Found in Nuclear Power Plants. Technical report, National Institute of Standards and Technology.

Li, J., Gong, J., and Stoliarov, S. I. (2014). Gasification experiments for pyrolysis model parameterization and validation. *International Journal of Heat and Mass Transfer*, 77:738–744.

Li, J. and Stoliarov, S. I. (2013). Measurement of kinetics and thermodynamics of the thermal degradation for non-charring polymers, https://doi.org/10.1016/j.combustflame.2013.02.012. *Combustion and Flame*, 160(7):1287–1297.

Linteris, G., Zammarano, M., Wilthan, B., and Hanssen, L. (2012). Absorption and reflection of infrared radiation by polymers in fire-like environments, https://doi.org/10.1002/fam.1113. *Fire and Materials*, 36(7):537–553.

Manring, L. E. (1989). Thermal degradation of poly (methyl methacrylate). 2. Vinyl-terminated polymer https://doi.org/10.1021/ma00196a024. *Macromolecules*, 22(6):2673–2677.

Manring, L. E., Sogah, D. Y., and Cohen, G. M. (1989). Thermal degradation of poly (methyl methacrylate). 3. Polymer with head-to-head linkages https://doi.org/10.1021/ma00202a048. *Macromolecules*, 22(12):4652–4654.

Maragkos, G. and Beji, T. (2021). Review of convective heat transfer modelling in cfd simulations of fire-driven flows. *Applied sciences*, 11(11):5240.

Matala, A. and Hostikka, S. (2011). Probabilistic simulation of cable performance and water based protection in cable tunnel fires. *Nuclear Engineering and Design*, 241(12):5263–5274.

Matala, A. and Hostikka, S. (2013). Modelling polymeric material using Microscale combustion calorimetry and other small scale data. In *Submitted to Fire and Materials*.

Matala, A., Hostikka, S., and Johan, M. (2008). Estimation of pyrolysis model parameters for solid materials using thermogravimetric data, `https://doi.org/10.3801/IAFSS.FSS.9-1213`. In *Fire Safety Science – Proceedings of the Ninth International Symposium, pp. 1213-1224*.

McCoy, C. G., Tilles, J. L., and Stoliarov, S. I. (2019). Empirical model of flame heat feedback for simulation of cone calorimetry. *Fire Safety Journal*, 103:38–48, doi:https://doi.org/10.1016/j.firesaf.2018.11.006.

McGrattan, K. and Floyd, J. (2021). Current and future parameters used by fds. In *ASTM Symposium on Obtaining Data for Fire Growth Models*.

McGrattan, K., Hostikka, S., Floyd, J., McDermott, R., and Vanella, M. (2005). *Fire Dynamics Simulator (version FDS6.7.6-810-ge59f90f-HEAD) – User's Guide*. US Department of Commerce, Technology Administration, NIST. `http://dx.doi.org/10.6028/NIST.SP.1019`.

McGrattan, K., Hostikka, S., Floyd, J., McDermott, R., and Vanella, M. (2021). Fire dynamics simulator technical reference guide volume 3: Validation, fds 6.7.6. *NIST Special Publication 1018-3, Sixth Edition*, doi:http://dx.doi.org/10.6028/NIST.SP.1018.

McGrattan, K., Hostikka, S., McDermott, R., Floyd, J., Weinschenk, C., and Overholt, K. (2013). Fire Dynamics Dimulator Technical Reference Guide Volume 1: Mathematical Model. *NIST special publication*, 1018(1):175.

Meunders, A., Baker, G., Arnold, L., Schroeder, B., Spearpoint, M., and Pau, D. (2014). Parameter optimization and sensitivity analysis for fire spread modelling with fds. In *SFPE 10th International Conference on Performance-Based Codes and Fire Safety Design Methods, University of Queensland, Australia*.

Modest, M. F. and Mazumder, S. (2021). *Radiative heat transfer*. Academic press.

Morrisset, D., Hadden, R. M., and Law, A. (2023). Characterization of flame spread over PMMA using a temperature reconstruction method, https://doi.org/10.1080/00102202.2023.2239459. *Combustion Science and Technology*, 195(14):3557–3570.

Morrisset, D., Hadden, R. M., and Law, A. (2024). Quantifying the controlling mechanisms of opposed flow flame spread: Influence of orientation, material, and external heating, https://doi.org/10.1016/j.firesaf.2023.104048. *Fire Safety Journal*, 142:104048.

Morrisset, D., Santamaria, S., Hadden, R., and Emberley, R. (2022). Implications of data smoothing on experimental mass loss rates, https://doi.org/10.1016/j.firesaf.2022.103611. *Fire Safety Journal*, 131:103611.

NIST (2023a). FDS Validation repository, NIST NRC Parallel Panels, PMMA_60_kW_1_cm.fds; Github. https://github.com/firemodels/fds/blob/300ee407ca64757098623ccc7ede12ae548137f8/Validation/NIST_NRC_Parallel_Panels/FDS_Input_Files/PMMA_60_kW_1_cm.fds, Commit: 300ee40.

NIST (2023b). FDS Validation repository on Github. https://github.com/firemodels/fds/tree/master/Validation/NIST_NRC_Parallel_Panels, Commit: 300ee40.

Nyazika, T., Jimenez, M., Samyn, F., and Bourbigot, S. (2019). Pyrolysis modeling, sensitivity analysis, and optimization techniques for combustible materials: A review, http://doi.org/10.1177/0734904119852740. *Journal of fire sciences*, 37(4-6):377–433.

PLEIADES (2025). Scientific Computing Center PLEIADES at the University of Wuppertal. https://pleiades.uni-wuppertal.de, Accessed in 2025-04-15.

Pope, I., Hidalgo, J. P., Hadden, R. M., and Torero, J. L. (2022). A simplified correction method for thermocouple disturbance errors in solids, https://doi.org/10.1016/j.ijthermalsci.2021.107324. *International Journal of Thermal Sciences*, 172:107324.

Quaresma, T. L., Hehnen, T., and Arnold, L. (2024). Sensitivity analysis for an effective transfer of estimated material properties from cone calorimeter to horizontal flame spread simulations, https://doi.org/10.1016/j.firesaf.2024.104116. *Fire Safety Journal*, page 104116.

Quaresma, T. L., Hehnen, T., and Arnold, L. (2025). The influence of small mass loss rate peaks on the rate of spread of predictive flame spread simulations: A theoretical study, https://doi.org/10.1016/j.firesaf.2025.104344. *Fire Safety Journal*, page 104344.

Quintiere, J. (1998). *Principles of fire behaviour*. CRC Press, Boca Raton.

Ramroth, L. A., Selden, B., and Lyon, R. E. (2006). Sensitivity and uncertainty analysis of a finite element thermal model of fiber-reinforced polymer composites exposed to fire. *Journal of Fire Sciences*, 24(5):411–436, doi:10.1177/0734904106068402.

Rehm, R. G. and Baum, H. R. (1978). The equations of motion for thermally driven, buoyant flows. *Journal of research of the National Bureau of Standards*, 83(3):297.

Rein, G., Lautenberger, C., Fernandez-Pello, A. C., Torero, J. L., and Urban, D. L. (2006). Application of genetic algorithms and thermogravimetry to determine the kinetics of polyurethane foam in smoldering combustion, https://doi.org/10.1016/j.combustflame.2006.04.013. *Combustion and flame*, 146(1-2):95–108.

Rogaume, T. (2019). Thermal decomposition and pyrolysis of solid fuels: Objectives, challenges and modelling, https://doi.org/10.1016/j.firesaf.2019.04.016. *Fire Safety Journal*, 106:177–188.

Saltelli, A. (2002). Making best use of model evaluations to compute sensitivity indices, https://doi.org/10.1016/S0010-4655(02)00280-1. *Computer physics communications*, 145(2):280–297.

Saltelli, A., Aleksankina, K., Becker, W., Fennell, P., Ferretti, F., Holst, N., Li, S., and Wu, Q. (2019). Why so many published sensitivity analyses are false: A systematic review of sensitivity analysis practices, https://doi.org/10.1016/j.envsoft.2019.01.012. *Environmental modelling & software*, 114:29–39.

Saltelli, A., Ratto, M., Andres, T., Campolongo, F., Cariboni, J., Gatelli, D., Saisana, M., and Tarantola, S. (2008). *Global sensitivity analysis: the primer*. John Wiley & Sons.

Sobol, I. M. (2001). Global sensitivity indices for nonlinear mathematical models and their Monte Carlo estimates, https://doi.org/10.1016/S0378-4754(00)00270-6. *Mathematics and computers in simulation*, 55(1-3):271–280.

Spink, C. H. (2008). Differential scanning calorimetry. *Methods in Cell Biology*, 84:115–141, doi:10.1016/S0091-679X(07)84005-2. Review article.

Stoliarov, S. I. and Li, J. (2016). Parameterization and validation of pyrolysis models for polymeric materials `https://doi.org10.1007/s10694-015-0490-1`. *Fire Technology*, 52:79–91.

Sudret, B. (2008). Global sensitivity analysis using polynomial chaos expansions, `https://doi.org/10.1016/j.ress.2007.04.002`. *Reliability engineering & system safety*, 93(7):964–979.

Swann, J. D., Ding, Y., McKinnon, M. B., and Stoliarov, S. I. (2017). Controlled atmosphere pyrolysis apparatus II (CAPA II): A new tool for analysis of pyrolysis of charring and intumescent polymers, `https://doi.org/10.1016/j.firesaf.2017.03.038`. *Fire Safety Journal*, 91:130–139.

Tester, J. W. and Modell, M. (1997). Thermodynamics and its applications. *(No Title)*.

Ujjwal, K., Aryal, J., Garg, S., and Hilton, J. (2021). Global sensitivity analysis for uncertainty quantification in fire spread models, `https://doi.org/10.1016/j.envsoft.2021.105110`. *Environmental Modelling & Software*, 143:105110.

Vermesi, I., Roenner, N., Pironi, P., Hadden, R. M., and Rein, G. (2016). Pyrolysis and ignition of a polymer by transient irradiation, `https://doi.org/10.1016/j.combustflame.2015.08.006`. *Combustion and Flame*, 163:31–41.

Viitanen, A., Hostikka, S., and Vaari, J. (2022). CFD simulations of fire propagation in horizontal cable trays using a pyrolysis model with stochastically determined geometry, `https://doi.org/10.1007/s10694-022-01291-6`. *Fire Technology*, 58(5):3039–3065.

Vogelsang, J. and Arnold, L. (2023). fdsreader - Fast and easy-to-use Python reader for FDS data. `https://github.com/FireDynamics/fdsreader`.

Vyazovkin, S., Achilias, D., Fernandez-Francos, X., Galukhin, A., and Sbirrazzuoli, N. (2022). Ictac kinetics committee recommendations for analysis of thermal polymerization kinetics. *Thermochimica acta*, 714:179243.

Vyazovkin, S., Burnham, A. K., Criado, J. M., Pérez-Maqueda, L. A., Popescu, C., and Sbirrazzuoli, N. (2011). ICTAC Kinetics Committee recommendations for performing kinetic computations on thermal analysis data, https://doi.org/10.1016/j.tca.2011.03.034. *Thermochimica acta*, 520(1-2):1–19.

Wagner, P.-R., Fahrni, R., Klippel, M., Frangi, A., and Sudret, B. (2020). Bayesian calibration and sensitivity analysis of heat transfer models for fire insulation panels, https://doi.org/10.1016/j.engstruct.2019.110063. *Engineering structures*, 205:110063.

Wang, P., Fan, F., and Li, Q. (2014). Accuracy evaluation of the gray gas radiation model in cfd simulation. *Case Studies in Thermal Engineering*, 3:51–58.

Webster Jr, R. D. (2009). *Pyrolysis model parameter optimization using a customized stochastic hill-climber algorithm and bench scale fire test data*. University of Maryland, College Park.

West, P. W. (1954). Inorganic thermogravimetric analysis. *Journal of Chemical Education*, 31(6):334, doi:10.1021/ed031p334.1.

Yang, F., Rippe, C., Hodges, J., and Lattimer, B. (2019). Methodology for material property determination https://doi.org/10.1002/fam.2721. *Fire and Materials*, 43(6):694–706.

Zeng, W., Li, S., and Chow, W. K. (2002). Review on chemical reactions of burning poly (methyl methacrylate) PMMA, https://doi.org/10.1177/0734904102020005482. *Journal of Fire Sciences*, 20(5):401–433.

Zhang, S., Li, Y., and Li, L. (2022). A review of devices and methods for measuring thermal emissivity at cryogenic temperatures. In *IOP Conference Series: Materials Science and Engineering*, volume 1241, page 012050. IOP Publishing.

Schriften des Forschungszentrums Jülich
IAS Series

Schriften des Forschungszentrums Jülich
IAS Series

Band / Volume 70
Towards Improved Civil Safety: Experimental Insights into Impulse Propagation through Crowds
S. Feldmann (2025), xi, 99 pp
ISBN: 978-3-95806-828-5

Band / Volume 71
Development and Evaluation of Architecture Concepts for a System-on-Chip Based Neuromorphic Compute Node for Accelerated and Reproducible Simulations of Spiking Neural Networks in Neuroscience
G. Trensch (2025), 219, XXXV pp
ISBN: 978-3-95806-832-2

Band / Volume 72
The tube furnace as a new bench scale experiment for pyrolysis
K. De Lannoye (2025), ix, 70 pp
ISBN: 978-3-95806-839-1

Band / Volume 73
Single-file Movement: Literature Review, Empirical Analysis with Artificial Neural Networks, and Modeling
R. Subaih (2025), x, 115 pp
ISBN: 978-3-95806-843-8

Band / Volume 74
Improvement and Validation of Visibility Models in Fire Safety
K. Börger (2025), ix, 97 pp
ISBN: 978-3-95806-857-5

Band / Volume 75
Simulation of Fire Propagation, Based on Material Pyrolysis
T. Hehnen (2025), VIII, 25, xcii pp
ISBN: 978-3-95806-875-9

Band / Volume 76
Sensitivity Analysis on Flame Spread Simulation
T. Lins da Silva Quaresma (2026), xxiii, 138, clx pp
ISBN: 978-3-95806-894-0

Weitere ***Schriften des Verlags im Forschungszentrum Jülich*** unter
http://wwwzb1.fz-juelich.de/verlagextern1/index.asp

IAS Series
Band / Volume 76
ISBN 978-3-95806-894-0

Mitglied der Helmholtz-Gemeinschaft

JÜLICH
Forschungszentrum